Reconstruction of Beauty Jets in Proton-Proton Collisions at $\sqrt{s}$ = 7 TeV with ALICE

Dissertation, Linus Feldkamp 2018

WWU MÜNSTER

wissen.leben

Institut für Kernphysik
Westfälische Wilhelms-Universität
Münster

Experimentelle Physik

Reconstruction of Beauty Jets in Proton-Proton Collisions at $\sqrt{s} = 7$ TeV with ALICE

Inaugural-Dissertation
zur Erlangung des Doktorgrades
der Naturwissenschaften im Fachbereich Physik
der Mathematisch-Naturwissenschaftlichen Fakultät
der Westfälischen Wilhelms-Universität Münster

vorgelegt von
Linus Feldkamp
aus Münster

– 2018 –

Dekan: Prof. Dr. Michael Klasen
Erster Gutachter: Prof. Dr. J. P. Wessels
Zweiter Gutachter: Prof. Dr. Anton Andronic

Tag der Disputation: . . . .
Tag der Promotion: . . . .

Table of contents

Chapter 1

Introduction

With the commissioning of the Large Hadron Collider in 2008 a new era of particle physics at unprecedented collision energies began, culminating in the joint announcement of new particle compatible with the Standard Model Higgs boson by the CMS[1] and ATLAS [2] collaborations in July 2012. Beside the results of the Higgs particle research, that have been verified and improved in precision over the recent years [3][4][5][6], the study of beauty quark and hadron physics is an important cornerstone of the scientific program at the LHC as it allows to test the Standard Model predictions with unchallenged accuracy. Most notably are the results published by the LHCb collaboration on the rare $B_s^0 \rightarrow \mu^+ + \mu^-$ decay channel [7] , the production of the $\Xi_b^{'-}$ and Ξ_b^{*-} [8] as well as the measurement of a penta-quark candidate [9]. The first collisions of lead nuclei in 2010 verified the formation of a strongly interacting state of matter known as Quark-Gluon Plasma (QGP) that is the focus of scientific program the ALICE collaboration [10].

The exact properties of this exotic state of matter are governed by a mix of short-range interactions and long-range collective behaviour (see e.g. [12]). Constraining the microscopic medium parameters therefore relies on the symbiotic dialogue between theoretic model predictions and the experimental measurement of medium related observables. As one of those, the partonic energy loss can be estimated by comparing measured particle yields in nucleus-nucleus collisions and the respective appropriately scaled yields in proton-proton collision.
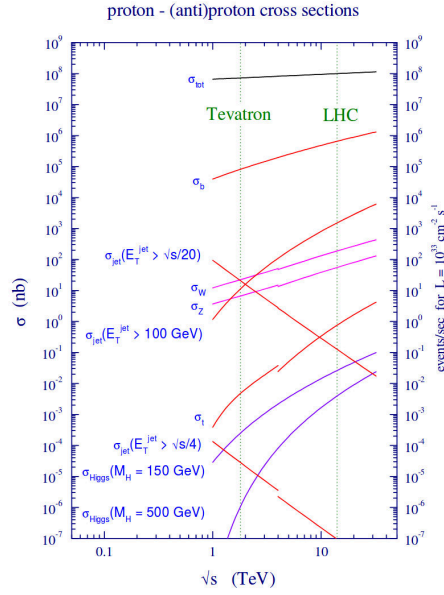
Figure 1.1: *Standard Model cross sections at different center-of-mass energies [11].*

One theoretical argument, the so-called "dead-cone" effect [13][14] predicts an ordering of the partonic energy loss depending on the quark mass with $\Delta E_b < \Delta E_c < \Delta E_s < \Delta E_d < \Delta E_u$. Also the energy loss for quarks is expected to the lower than that of gluons due to the smaller Casimir colour factor $\Delta E_q < \Delta E_g$.

The measurable effect of partonic energy loss on final state observables as momentum dependent hadronic jet cross sections is less direct, but can be expressed in terms of the nuclear modification factor R_{AA}. It is defined as

$$R_{AA} = \frac{\mathrm{d^2 N_{AA}/dy dp_T}}{\langle T_{AA}\rangle \mathrm{d}\sigma_{\mathrm{pp}}^{\mathrm{INEL}}/\mathrm{dy dp_T}}, \tag{1.1}$$

where $\mathrm{d^2 N_{AA}/dy dp_T}$ is the differential yield in nucleus-nucleus collisions, $\mathrm{d}\sigma_{\mathrm{pp}}^{\mathrm{INEL}}/\mathrm{dy dp_T}$ is the differential cross section in proton-proton collisions and $\langle T_{AA}\rangle$ is the nuclear thickness function, that can be obtained from Glauber Monte Carlo calculations. The R_{AA} is a measure of the modification of the transverse momentum spectrum due to initial- and final state medium effects in nucleus-nucleus collisions, where $R_{AA} = 1$ is equivalent to the absence of such effects.

Calculations by Huang et al. [15] show that in the case of beauty jets even any ordering in the partonic energy loss is effectively smeared out during the hadronization process and any significant differences in the beauty jet R_{AA} compared to the one of light jets is to be expected at rather low transverse jet momenta (See figure 1.2).
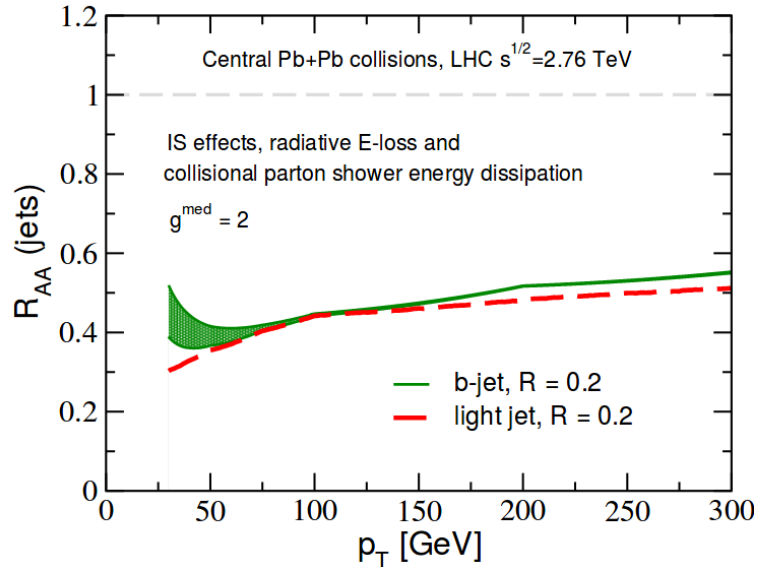
Figure 1.2: *Prediction for the p_T dependent suppression of light- and beauty-jet cross section in central $\sqrt{s_\mathrm{NN}} = 2.76$ TeV Pb$-$Pb collisions for a jet radius of $R = 0.2$ (See [15] for details).*

This thesis presents a new method for the statistical reconstruction of beauty jets using the ALICE detector. Using this technique the double-differential charged beauty jet cross section in proton-proton collisions at $\sqrt{s} = 7$ TeV down to $p_\mathrm{T}^{\mathrm{ch.b-jet}} = 5$ GeV$/c$ is reconstructed.

The presented results can be compared to Standard Model predictions as well as be used as a reference or a recipe to obtain a reference for future energy loss studies in Pb$-$Pb collisions.

Following this introduction chapters 2 and 3 introduce the reader to the theoretical foundation of beauty production in proton-proton collisions, as well as to the experimental setup of the ALICE detector. The results on neural-network-based electron-pion separation with the ALICE Transition Radiation Detector (TRD) studied by the author are briefly reported in section 2.2.4 .

Chapter 4 constitutes the central part of this thesis. Here the devised reconstruction method for charged beauty-jets is discussed and the measured double differential beauty jet cross section is presented as well as compared to theoretical predictions.

Chapter 2

Experimental setup

If science is to progress, what we need is the ability to experiment, honesty in reporting results—the results must be reported without somebody saying what they would like the results to have been—and finally—an important thing—the intelligence to interpret the results.

.

—— Richard P. Feynman

This chapter reviews the experimental setup as it was used in the 2010 proton-proton data taking period. Over the recent years many upgrades and modifications of both the accelerator configuration and configurations of the involved sub-detectors were implemented that are however not part of the following discussion.

2.1   The Large Hadron Collider

The Large Hadron Collider (LHC)[17, 18] is a 26.7 km long hadron-accelerator and collider located near Geneva at CERN.

It is housed in the tunnel of the former Large Electron Positron collider (LEP) [19] that was commissioned in 1989. The tunnel consists of eight 210 m long straight sections and eight 2.9 km long arc sections 45–170 m below the surface. The LHC uses two separate beam pipes enclosed by 1232 superconducting dipole magnets and 392 quadrupole magnets for focussing, operating at up to 8.33 T. It can accelerate protons and lead ions to a design center-of-mass energy up to $\sqrt{s} = 14$ TeV in proton-proton collisions.

There are seven experiments located at the LHC beam line, ATLAS, ALICE, CMS, LHCb, TOTEM, LHCf and MoEDAL whose physics programs include the verification
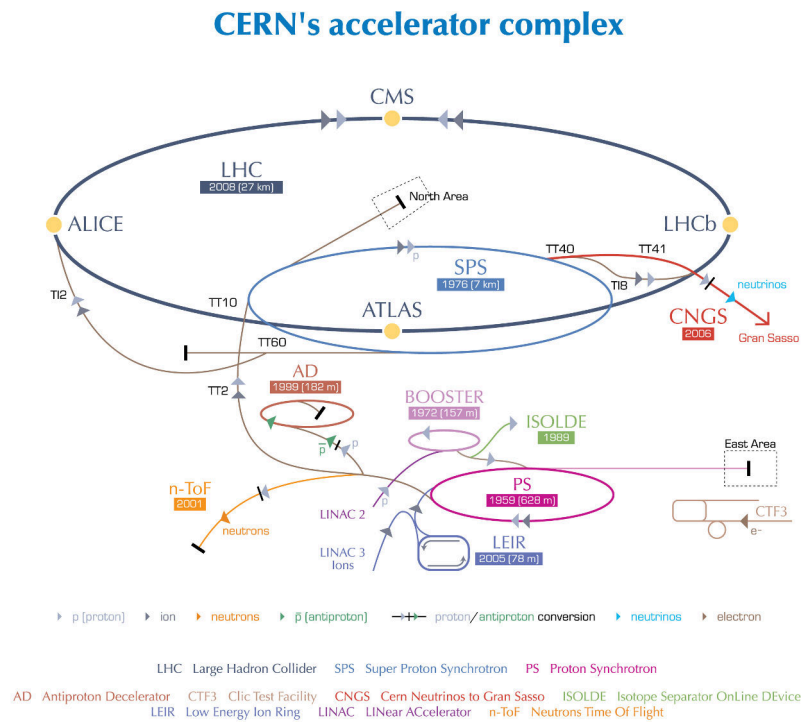
Figure 2.1: *The CERN accelerator complex [16].*

of and the search for physics beyond the Standard Model. Until today no physics beyond the Standard Model has been found, however in 2012 the long sought Higgs boson was discovered by CMS and ATLAS.
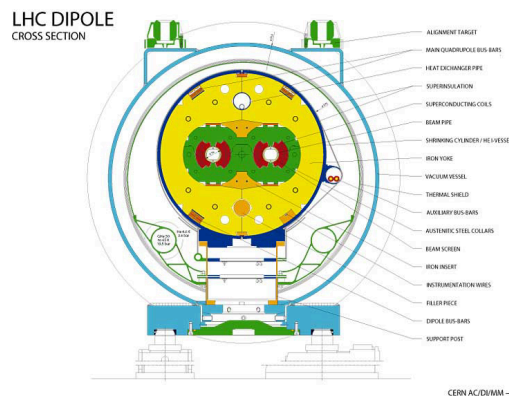
Figure 2.2: *Schematic cross section of one LHC dipole magnet [20]*

2.1.1   The LHC proton injection cycle

The protons are produced from hydrogen gas via a pulsed electrical discharge in a so called duoplasmatron proton source (see figure 2.3). The duoplasmatron consists of
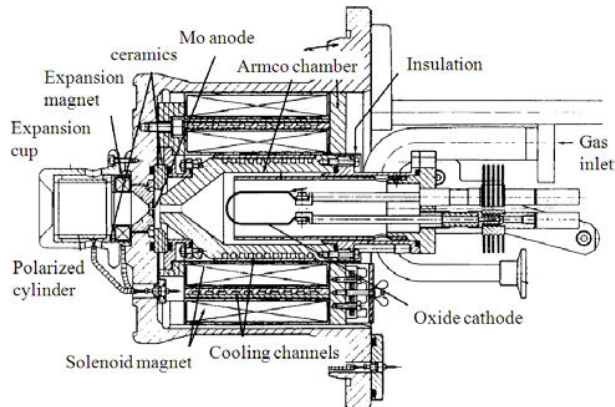
Figure 2.3: *The duoplasmatron proton source [21]*

heated (150 W, 50 A) thermionic oxide cathode made from a painted nickel mesh with a BaO to SrO ratio of 43% to 57% embedded into an external plasma chamber made from Armco steel. The anode is made from a 1 mm molybdenum insert embedded within an iron support structure. The arc voltage is in the range of 500-1000 V during ignition with about 80 V at discharge providing a pulsed $50-60$ A current for about $20-150$ μs. The pulse length is variable and modified in accordance with the final user intensity requirements. The repetition rate is 0.83 Hz, matched to the Proton Synchrotron Booster (PSB) cycle time of 1.2 s. The hydrogen gas is fed into the duoplasmatron from a standard gas bottle at a flow rate of about 4 sccm. The protons are then created via the processes $H_2 + e^- \rightarrow H_2^+ + 2e^-$, $H_2^+ + e^- \rightarrow H^+ + H + e^-$ and $H + e^- \rightarrow H^+ + 2e^-$ or equivalently $H_2 \rightarrow 2H^+ + 2e^-$. After a pressure reduction the protons are extracted and pre-accelerated up to 90 kV providing a beam current of more than 200 mA. The proton beam is then fed into a 1.75 m long radio frequency quadrupole (RFQ) operating at a frequency of 201.56 MHz [22]. The RFQ focusses the particle beam, and accelerates it up to 750 keV. Due to the internal sinusoidal pole structure, the RFQ groups the beam particles into 6 particle bunches that are then fed into the LINAC2. The 30 m long LINAC2 accelerates the protons up to 50 MeV at a current of 180 mA (see table 2.1).

Parameter	LHC Specification	Achieved	
Current during pule	180	182	mA
Pulse length	30	>100	μs
Transverse norm. rms emittance	1.2	1.2	μm
Momentum spread ($\pm 2\sigma$)	± 0.15 %	± 0.15 %	

Table 2.1: *Characteristics of the LHC proton beam from the Linac2 [23]*

The protons are then accelerated up to 1.4 GeV in the PSB. The PSB is a synchrotron with a diameter of about 50 m consisting of four stacked beam pipes with 1/4 of the Proton Synchrotron (PS) circumference each. The PS accelerates the protons up to

26 GeV and provides the LHC bunch train generation. Due to some drawbacks in the creation of bunches shorter than 5 ns the originally proposed debunching-rebunching scheme was replaced with a so called multiple-splitting scheme. In this scheme 6 bunches from the PSB are captured in the PS at 1.4 GeV and then split into three by a careful adjustment of the operational parameter of three groups of cavities operating at different harmonics. After acceleration up to 25 GeV each bunch is split twice creating a total of 72 bunches that are then shortened to ~ 4 ns at a bunch spacing of 25 ns. Table 2.2 summarizes the parameters of the PS operation.

	Multiple-splitting scheme
No. of bunches per PSB ring	1
No. of PSB cycles per PS cycle	2
No. of bunches from PSB per PS cycle	6
Harmonic no. at PS injection	7
Bunch splitting at 1.4 GeV	$1 \Rightarrow 3$
No. of bunches from 1.4GeV to 25 GeV	18
Double bunch splitting at 25 GeV	$1 \Rightarrow 4$
Harmonic no. at PS extraction	84
No. of bunches to SPS per PS cycle	72 (+12 empty buckets)
Nominal PS intensity at 1.4 GeV for 1.15×10^{11} protons	8.28×10^{12}
Nominal PSB intensity per ring	1.38×10^{12}

Table 2.2: *PS complex operation for filling the LHC (multiple-splitting scheme) [18]*

The Super Proton Synchrotron (SPS) completes the pre-acceleration by accelerating the protons from 26 GeV up to 450 GeV. The machine and beam parameters are listed in table 2.3

Proton momentum p	450	GeV/c
Machine radius R	1100	m
Min. beam pipe radius b	25	mm
Revolution time / frequency T/f_{rev}	23/43.3	μs/kHz
Betatron tunes $Q_{h,v}$	26.7	
Gamma transition γ	23.23	
Number of bunches k	243	
Protons/bunch	1.05	10^{11}
Total intensity	0.177	A
Bunch spacing s	25	ns
Bunch frequency f_b	40	MHz
Bunch length	4	ns
Transverse normalized emittance	3	μm
Average beam size σ	2.3	mm
Longitudinal emittance	0.35	eVs
		MHz

Table 2.3: *SPS beam and machine parameters [24]*

After iterative filling from the PS the SPS holds 243 bunches occupying 3/11 of the SPS ring. The SPS cavities have a filling time of 600 ns and operate at a frequency

of 200.2 Mhz [25] providing an acceleration voltage of 8 MV. After the SPS injection is completed a 8.25 s ramping cycle starts accelerating the protons to the final energy. The ramp is followed by a one second period in which the bunches are longitudinally compressed using a 400 MHz RF system and the SPS phase is adjusted with respect to the LHC for the correct injection via one of two possible extraction lines (west: TI2, east: TI8). With the injection into the LHC one so-called supercycle is completed. 24 supercycles are required for one LHC fill, that is completed after approximately 8 minutes. In the LHC the bunches are then accelerated up to their nominal beam energy. The proton bunches are there captured using a 200 MHz RF system and accelerated and refocused using a system 400 MHz[18] of eight superconducting cavities per beam, each providing $2MV$ per revolution. The performance related parameters for the 2010 period and the nominal design values are listed in table 2.4.

Parameter	2010	Design value	
Beam energy	3.5	7	TeV
β^* in IP 1 and 5 (2.0/3.5)	0.55		m
Bunch spacing	150	25	ns
Number of bunches	367	2808	
Max. protons per bunch	1.2×10^{11}	1.15×10^{11}	
Nominal emittance at start of fill	≈ 2	3.75	mm mrad
Peak luminosity	2.1×10^{32}	1×10^{34}	$cm^{-2}s^{-1}$
Max. mean number of events	4	19	
Stored beam energy	≈ 28	≈ 362	MJ

Table 2.4: *Beam performance related parameters for the 2010 proton proton run. [26]*

2.1.2 The LHC heavy ion operation

As the heavy ion operation is beyond the scope of the analysis presented in this thesis only ion-insertion is sketched in this section. The interested reader is referred to more detailed literature e.g. [18].

In heavy-ion operation mode, lead ions mostly $^{208}Pb^{27+}$ are produced from a piece of heated (to approx. 550 ° C) high-purity lead sample using electron-cyclotron resonance (ECR) [27], see figure 2.4. The beam ions are then extracted at approximately 2.5 AkeV (see table 2.5) with a repetition time of 0.2-0.4 s.

The beam of $^{208}Pb^{27+}$ ions accelerated up to 4.2 MeV per nucleon in the LINAC3 accelerator. After the accelerator the ions hit a carbon stripping foil (see STR in figure 2.5) creating a beam of $^{208}Pb^{54+}$.
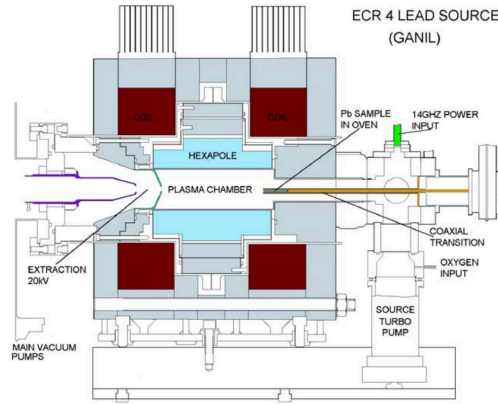
Figure 2.4: *ECR(ECR4) lead ion source source [28]*

Resonance frequency	18	GHz
Resonance field	0.65	T
Extraction energy	2.5	AkeV
Extraction voltage	20	kV
Extraction current	~ 200	μA
Typ. pulse length	200	μs
Lead ions / 200 μs pulse	9×10^9	
ϵ_{rms}^*	0.07	μm

Table 2.5: *ECR parameters for $_{208}Pb^{27+}$ [29]*
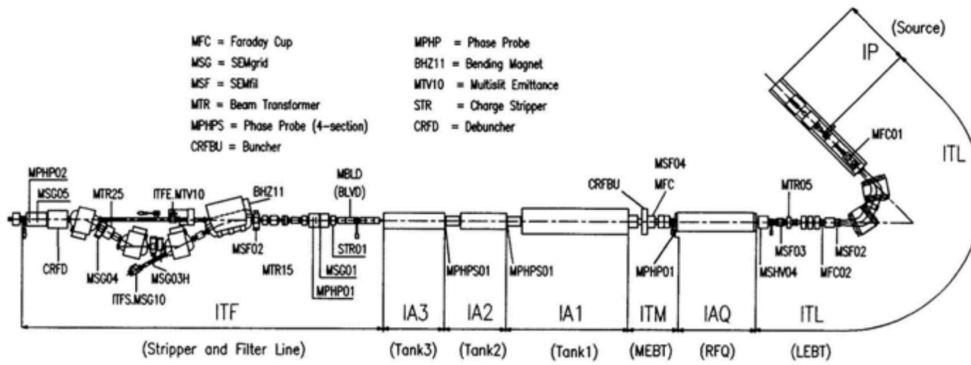
Figure 2.5: *Schematic view of the LINAC3 [28]*

The resulting wide ion bunches are compressed in the Low Energy Ion Ring (LEIR). In the LEIR[30] a series of $200\mu s$ low intensity LINAC3 pulses are transformed into 200 ns high-intensity bunches using a multi-turn injection scheme. Multiple (4 or 5) pulses are captured into two bunches and accelerated up to 72.2 MeV per nucleon.

The LEIR is followed by the PS increasing the beam energy up to 5.9 GeV. The ion beam is directed to the SPS passing a 0.8 mm aluminium stripper foil producing fully stripped $^{208}Pb^{82+}$ ions.

SPS is filled in 13 transfers up to 52 bunches and accelerated to 177 AGeV. Finally the LHC is filled via 12 injections from the SPS to a total of 592 ion bunches at a nominal bunch spacing of 100 ns that are then accelerated to the final operation energy (i.e. e.g. 1.38 ATeV for the 2010 Heavy Ion run).

2.2   A Large Ion Collider Experiment (ALICE)

ALICE is the largest general-purpose heavy-ion collider experiment in the world. From the first letter of intent [31] in 1993 to its final approval in 1997 it was specifically designed for the study of the strongly interacting sector of the Standard Modell with a focus on the investigation of the properties of the Quark-Gluon Plasma (QGP). Therefore it was build to provide excellent track reconstruction capabilities, momentum resolution and particle identification over a momentum range spanning from 100 MeV/c to above 100 GeV/c even in highest-multiplicity nucleus-nucleus collisions. The full physics program includes nucleus-nucleus, proton-nucleus as well as proton-proton collisions.

ALICE is located in a distance of about 4 km from the CERN main site in the small village of Saint Genis-Pouilly at the LHC interaction point 2 (IP2). The construction weights approximately 10000 tons with the overall dimensions of $16 \times 16 \times 26$ m^3. It is aligned with the beam-line in a depth of 44 m below the surface level and accessible via the PX24 maintenance shaft.
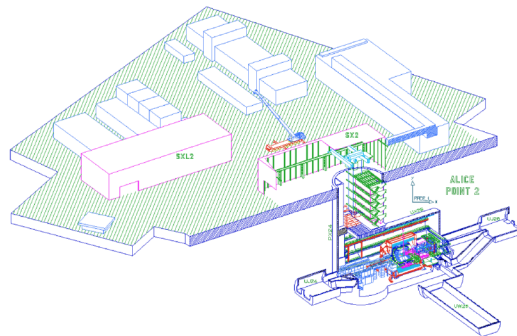

Figure 2.6: *Schematic sketch of the ALICE detector complex at Point 2 in Saint Genis-Pouilly [18]*

The detector consists of 18 sub-detectors with their individual support infrastructure,
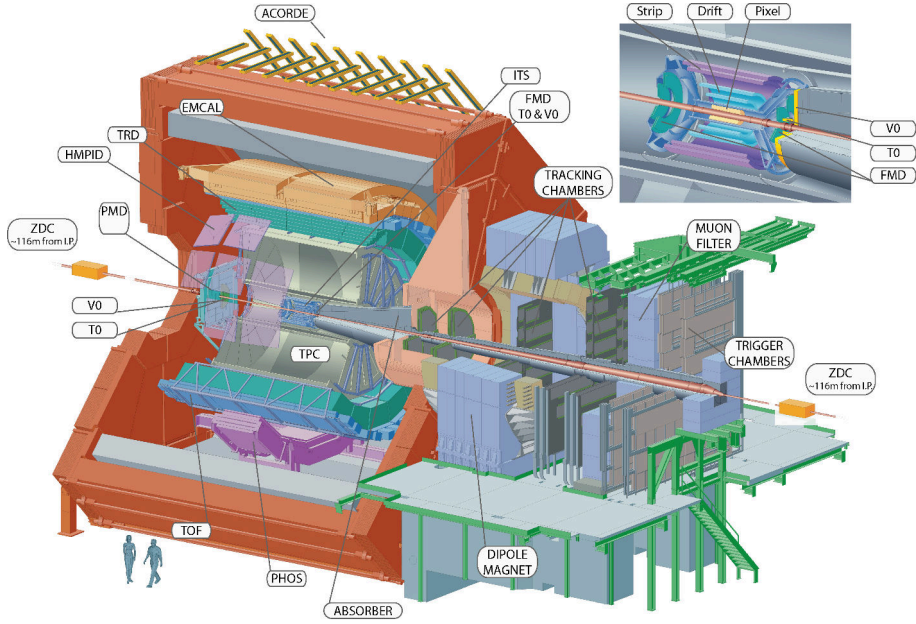

Figure 2.7: *Schematic of the ALICE detector*

the detector control systems and data acquisition hardware. The central part of the detector is enclosed by the former L3 magnet [32, 33] providing a 0.5 T magnetic field parallel to the beam direction to enable particle momentum and charge reconstruction. The lower momentum cut-off imposed by the magnetic field for particles to traverse the Time Projection Chamber (TPC) is $0.3 \cdot B(0.5T) \cdot R(2.5m) = 0.2$ GeV/c. The LHC beam line at IP2 is surrounded by a segmented beam pipe extending along ± 19m in beam direction relative to the nominal detector centre. While the outer parts are mainly constructed from stainless steel and copper, the central section consists of a 4 m long and 0.8 mm thick beryllium pipe with a diameter of about 58 mm to maximize particle transparency without disturbing the colliders running conditions. It extends from -3585 mm to 356 mm in z direction and is protected by a 80 μm thick polyimide wrapper. The Inner Tracking System (ITS) surrounds the beam pipe with a inner radius of 39 mm followed by the Time Projection Chamber, the Transition Radiation detector, the Time-Of-Flight detector(TOF), two calorimeters PHOS and EMCAL and HMPID. The central detector assembly is accompanied by the muon arm on the C side. Additional several detectors are deployed to determine relevant interaction properties needed for event selection and triggering by monitoring relevant beam properties. These detectors are the Zero-Degree calorimeters (ZDC), the T0, V0A/C and the FMD. The L3 magnet is complemented by the large dipole magnet of the muon system on the C side. Table 2.6 provides an overview of all ALICE sub-detector systems.

Detector	Acceptance		Position	Technology	Main purpose
	Polar	Azimuthal			
SPD*	$\|\eta\| < 2.0$	full	$r = 3.9$ cm	Si pixel	tracking, vertex
	$\|\eta\| < 1.4$	full	$r = 7.6$ cm	Si pixel	tracking, vertex
SDD	$\|\eta\| < 0.9$	full	$r = 15.0$ cm	Si drift	tracking, PID
	$\|\eta\| < 0.9$	full	$r = 23.9$ cm	Si drift	tracking, PID
SSD	$\|\eta\| < 1.0$	full	$r = 38$ cm	Si strip	tracking, PID
	$\|\eta\| < 1.0$	full	$r = 43$ cm	Si strip	tracking, PID
TPC	$\|\eta\| < 0.9$	full	$85 < r/\mathrm{cm} < 247$	Ne drift+MWPC	tracking, PID
TRD*	$\|\eta\| < 0.8$	full	$290 < r/\mathrm{cm} < 368$	TR+Xe drift+MWPC	tracking, $e^\pm$ id
TOF*	$\|\eta\| < 0.9$	full	$370 < r/\mathrm{cm} < 399$	MRPC	PID
PHOS*	$\|\eta\| < 0.12$	$220° < \phi < 320°$	$460 < r/\mathrm{cm} < 478$	PbWO$_4$	photons
EMCal*	$\|\eta\| < 0.7$	$80° < \phi < 187°$	$430 < r/\mathrm{cm} < 455$	Pb+scint.	photons and jets
HMPID	$\|\eta\| < 0.6$	$1° < \phi < 59°$	$r = 490$ cm	C$_6$F$_{14}$ RICH+MWPC	PID
ACORDE*	$\|\eta\| < 1.3$	$30° < \phi < 150°$	$r = 850$ cm	scint.	cosmics
PMD	$2.3 < \eta < 3.9$	full	$z = 367$ cm	Pb+PC	photons
FMD	$3.6 < \eta < 5.0$	full	$z = 320$ cm	Si strip	charged particles
	$1.7 < \eta < 3.7$	full	$z = 80$ cm	Si strip	charged particles
	$-3.4 < \eta < -1.7$	full	$z = -70$ cm	Si strip	charged particles
V0*	$2.8 < \eta < 5.1$	full	$z = 329$ cm	scint.	charged particles
	$-3.7 < \eta < -1.7$	full	$z = -88$ cm	scint.	charged particles
T0*	$4.6 < \eta < 4.9$	full	$z = 370$ cm	quartz	time, vertex
	$-3.3 < \eta < -3.0$	full	$z = -70$ cm	quartz	time, vertex
ZDC*	$\|\eta\| > 8.8$	full	$z = \pm 113$ m	W+quartz	forward neutrons
	$6.5 < \|\eta\| < 7.5$	$\|\phi\| < 10°$	$z = \pm 113$ m	brass+quartz	forward protons
	$4.8 < \eta < 5.7$	$\|2\phi\| < 32°$	$z = 7.3$ m	Pb+quartz	photons
MCH	$-4.0 < \eta < -2.5$	full	$-14.2 < z/\mathrm{m} < -5.4$	MWPC	muon tracking
MTR*	$-4.0 < \eta < -2.5$	full	$-17.1 < z/\mathrm{m} < -16.1$	RPC	muon trigger

Table 2.6: *From [34]: The ALICE detectors as listed in. The transverse (for HMPID, radial) and longitudinal coordinates r, z are measured with respect to the ALICE interaction point (IP2). The z axis points along the anticlockwise LHC beam. The detectors marked with an asterisk (*) are used for triggering. As of 2013, 13/18 of the TRD modules and 3/5 of the PHOS modules have been installed. The ZDCs were moved from $|z| \approx 114.0$ m to $|z| \approx 112.5$ m during the winter shutdown 2011/2012. The η and ϕ ranges specified for the proton ZDC are purely geometrical and do not take into account how charged particles are transported through the magnetic elements of the beam line.*

An overview over the different sub-detector systems, the ALICE coordinate system, the track and vertex reconstruction, the trigger system as well as over the implemented reconstruction and analysis software is given in the following sections.

2.2.1   The ALICE coordinate system and conventions

The ALICE coordinate system [35] originates at the nominal interaction point IP ($x = y = z = 0$). It is a right-handed orthogonal coordinate system with the x-axis perpendicular to the beam direction aligned with the local horizontal plane and pointing to the accelerator center. The y-axis is perpendicular to the x-axis and the local beam direction and thus the z-axis parallel to the beam line. The positive part of the z-axis is pointing toward RB24. The azimuthal angle is defined such that $\phi(x = 1, y = 0) = 0$ and $\phi(x = 0, y = 1) = \pi/2$ with the axis of rotation aligned with the negative z direction. The polar angle θ is the angle between the x,y-plane and the z axis and increase from 0 (aligned with the z-axis) to $\pi/2$ (x,y-plane) to π at -z;

Detector sides are labelled A at positive z-values, B around z=0 and C at negative z values. Furthermore detector parts may be labelled I ($x > 0$) , O($x < 0$), U($y > 0$) and D($y < 0$).
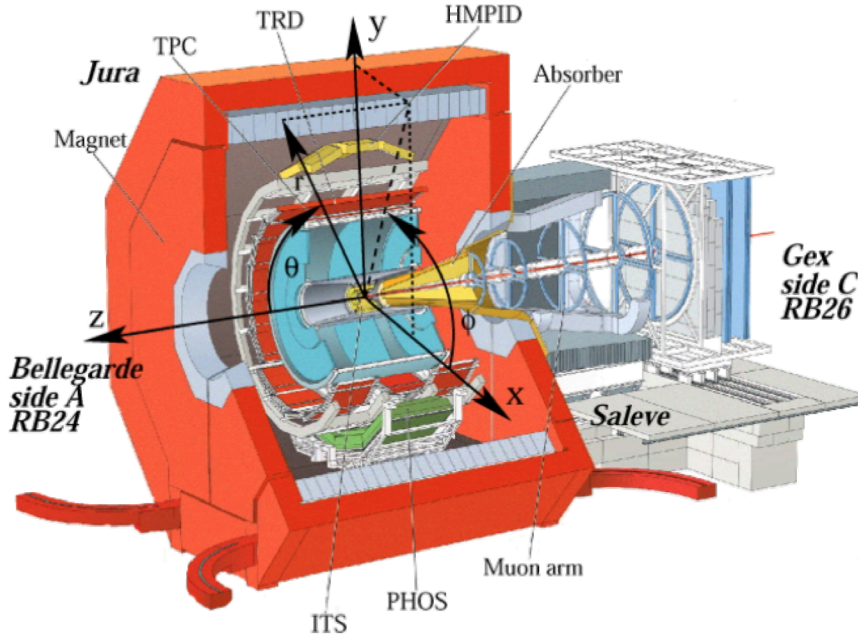

Figure 2.8: *ALICE coordinate system axis, angles and detector sides [35].*
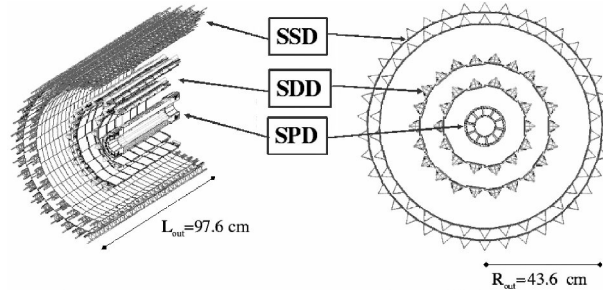
2.2.2 Inner Tracking System

Figure 2.9: *Schematic sketch of the ALICE inner tracking system [36]*
.

The Inner Tracking System [36, 18, 37] is the innermost sub-detector in ALICE. Its key tasks are the reconstruction of primary and secondary vertices and the measurement of particles with a momentum below 200 MeV/c. The ITS consists of a concentric configuration of three types of semi-conductor detectors arranged in two layers per type. Its effective acceptance covers a pseudo-rapidity region of $|\eta| < 0.9$ and the full azimuth angle to maximize the track matching with the Time Projection Chamber. The innermost layer however covers $|\eta| < 1.98$. Silicon Pixel Detectors have been selected for the first two layers (SPD) to provide a good track impact parameter resolution even at large particle multiplicities. The next two layers are made from Silicon Drift Detectors (SDD) and the two outermost layers from double-sided Silicon micro-Strip Detectors (SSD). The SDD and SSD provide a limited particle identification via dE/dx in the non-relativistic momentum region.

The SPD layers [38] consist of 80 (160) modules each build from a two-dimensional 265 x 160 cell matrix of reverse-biased silicon detector diodes connected to five readout chips at a radius of $r = 3.9(7.6)$ cm. Two modules are joined to form a 14.16 cm long half-stave that are then connected pair-wise along the z-direction to a carbon sector support structure. Every support structure holds six halve-staves arranged with a 2% sensor overlap forming a SPD sector. Ten sectors are combined as two five sector half-barrels to form the full-barrel. The SPD is cooled using C_4F_{10} via the support structure. The resulting spatial resolution for the different layers is listed in table 2.7 The Silicon Drift Detectors (SDD) [38, 39] layers are mounted at $r = 15.0(23.6)$ cm and consist of 14 (22) ladders with six (eight) modules arranged with a partial overlap of more than 580 μm to ensure full angular coverage. Each of the 260 module consists of two drift regions with a drift field of 500 V/cm and the front-end electronics and is produced from 300 μm thick NTD (neutron transmutation doped) silicon with a resistivity of 3 kΩcm The coordinate reconstruction is done using the centroid of deposited charge along the
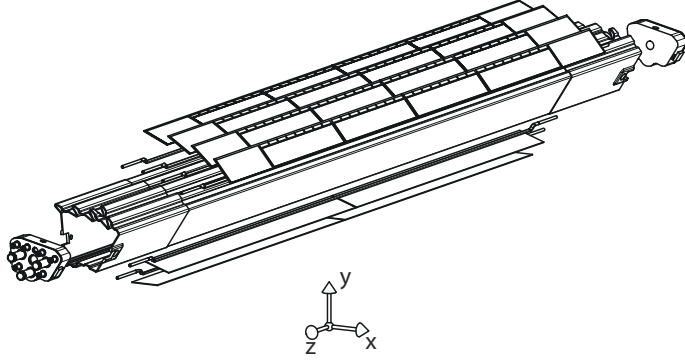
Figure 2.10: *Schematic sketch of a SPD sector [38]*

anode for the z-direction and via the drift time in $r\phi$. To ensure a good knowledge of the highly temperature-dependent drift velocity ($\propto T^{-2.4}$) 33 MOS charge injectors are incorporate into the design at well-defined distances in each of the two drift regions, The outer layers of ITS are formed by 34 (38) ladders staggered by 600 μm in radial
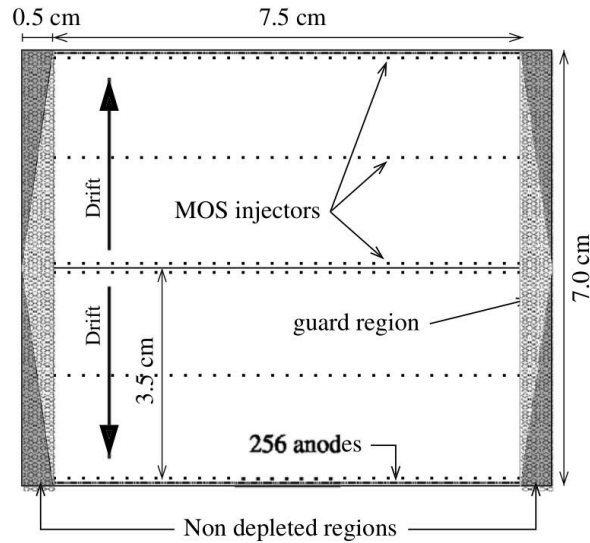
Figure 2.11: *Schematic sketch of a SDD module [38].*

direction with each consisting of 22 (25) modules along the z-direction. This is achieved by mounting adjacent modules at 6 mm separated radii. Every module is build from one sensor with 768 strips with a pitch of 95 μm on each side to form a stereo angle of 35 mrad. In total 1698 modules are attached to the support structures. The SSD layers are especially important for the ITS-TPC track matching and they provide low-momentum (< 100 MeV/c) tracking and particle identification capabilities via dE/dx measurements together with the two SDD layers. The ITS is optimized for a multiplicity of 8000 tracks per rapidity unit at mid-rapidity with the capability to reconstruct up to 15000 tracks

Layer	Type	r (cm)	$\sigma(r\varphi)$ (μm)	$\sigma(z)$ (μm)	Channels
1	SPD	3.9	12	100	3 276 800
2	SPD	7.6	12	100	6 553 600
3	SDD	15.0	35	25	43 008
4	SDD	23.9	35	25	90 112
5	SSD	38.0	20	830	1 148 928
6	SSD	43.0	20	830	1 159 200

Table 2.7: *ITS layer position and spatial resolution.*

simultaneously.

2.2.3 Time Projection Chamber
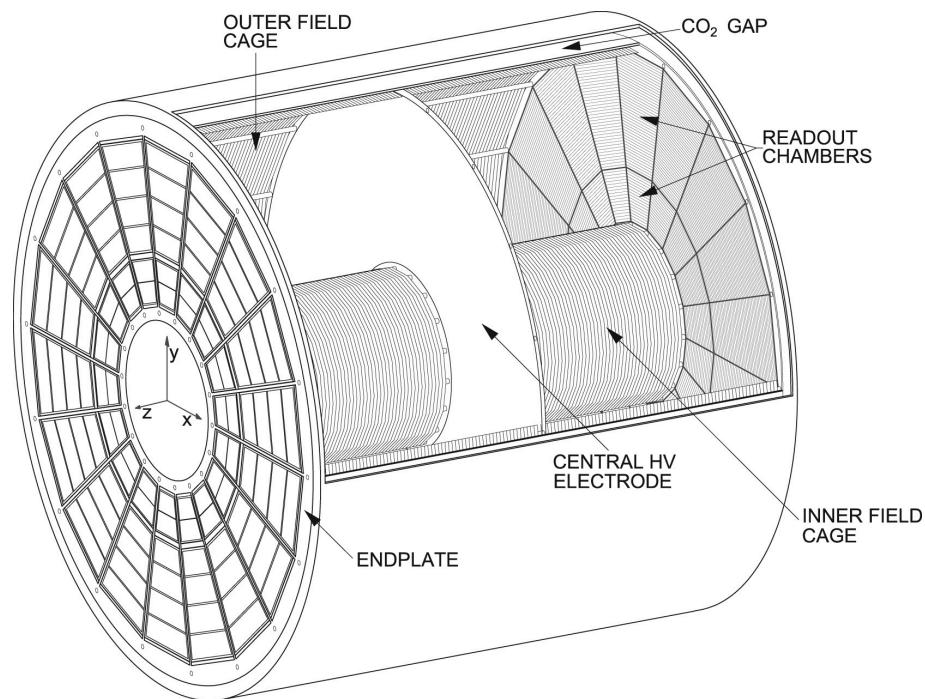
Figure 2.12: *Schematic view of the ALICE TPC .*

The time projection chamber (TPC) is by far the largest tracking detector in ALICE. It covers $-0.9 < \eta < 0.9$ in pseudo rapidity with full radial track length and matches in the three smaller tracking detectors of the inner barrel: the ITS, the Time-Of-Flight (TOF) and the Transition-Radiation-Detector (TRD). Allowing radial track lengths of 1/3 and thus a smaller momentum resolution. The pseudo-rapidity phase-space extends to $-1.5 < \eta < 1.5$. The TPC provides full coverage in the azimuthal direction and covers a transverse momentum range 0.1 GeV/c < p_T < 100 GeV/c. In radial direction it is attached to the ITS at 60.65 cm and extends up to 278.0 cm providing an active region of about 90 m^3 with a maximum traversing length of 250 cm. It consists of a cylindrical field

cage with 36 readout chambers at each of the detectors end-plates. The active volume is separated ($z = 0, \eta = 0$) by a central 22 μm aluminized Mylar electrode and filled with a 85.7/9.5/4.8 mixture of Ne/CO_2 and N_2 (90/10 Ne/CO_2 from 2011). The field cage is operated at voltage gradients of 400 V/cm with a high-voltage of 100 kV at the central electrode. Charged particles traversing the active region produce electrons and ions that are transported by field to the readout chambers. The field gradient and the maximum distance of a interacting particle to the central electrode of 250 cm result in a maximum drift time of about 92 μs for electrons. The drift time limits the maximal luminosity at which ALICE can take data in proton-proton events, less in the other collision systems. Also the significantly slower drift time of the produced ions will lead to the generation of a non-vanishing space charge distorting the reconstructed tracks. These mis-tracking is corrected and does not further limit the temporal resolution. The charge deposited in the readout planes provide 3d track reconstruction through the position of read-out electrodes and the arrival times of the electrons. The TPC is designed to reconstruct events with 8000 charged tracks per pseudo-rapidity unit thus more than 20000 charged tracks.

2.2.4   Transition Radiation detector
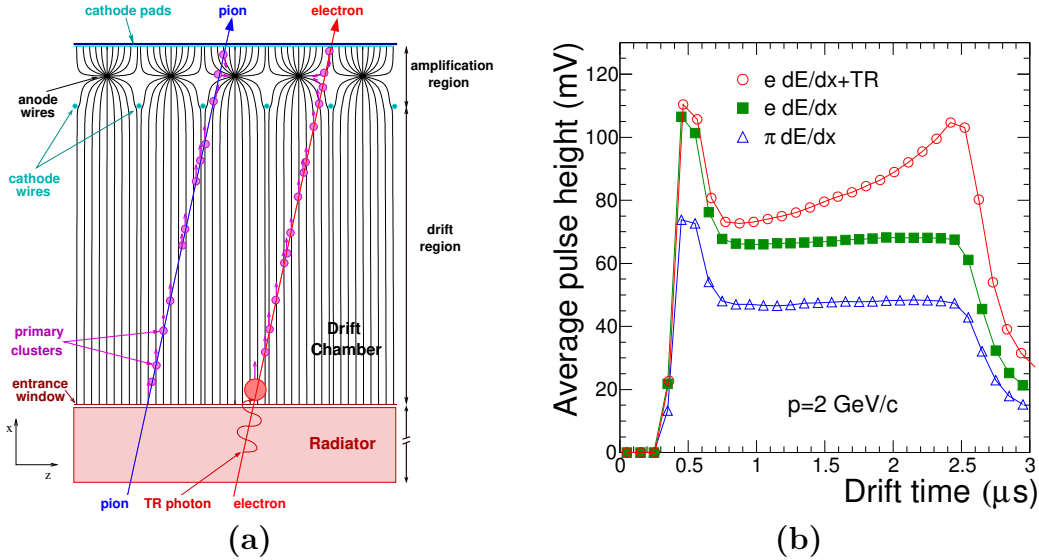
Figure 2.13: *a. Schematic cross section of a TRD chamber including radiator. b. Average pulse height as a function of drift time for pions and electrons with and without radiator [40]*

The ALICE Transition Radiation (TRD)[40] detector is follows the TPC at a radius $r = 2.9$ m to $r = 3.7$ m it covers the pseudo-rapidity region of $-0.9 \leq \eta \leq 0.9$ and the full azimuth. Initially in 2009 the TRD consisted of only seven supermodules while

three additional modules were added the 2010 winter shutdown and another three in the winter shutdown of 2011. The TRD was completed in the long shutdown 1 (LS1) in 2013/2014. In its final configuration the TRD is segmented into 18 azimuthal sectors and five longitudinal stacks consisting of six layers each. Each of the 522 layers is designed to be a independent read-out chamber with active areas of 0.90 m × 1.06 m to 1.13 m × 1.43 m and a thickness of 12 cm. Each layer is build from a 48 mm thick carbon fibre laminated Rohacell/polypropylene fibre sandwich radiator followed by a 30 mm drift region and a 7 mm multi-wire proportional chamber,that is then followed by the back-panel mounted read-out pads and electronics and it is filled with a 85% Xe 15% CO_2 gas mixture. Particles that transverse the radiator above $\gamma \simeq 1000$ (only electrons at LHC energies) will produce additional transition radiation (TR) photons with energies of $1 - 30$ keV. The TR photons are absorbed in the drift region close to the absorber leading to a characteristic peak (TR peak) at large drift times (see figure 2.13b).

2.2.4.1 Electron identification with the TRD

The TRD offers a unique and efficient way to identify electrons and separate them from other particles, dominantly pions. In the early stage of his studies the author worked on the implementation of a Neural Network (NN) based improvement to standard PID methods.

In this brief excursus the conceptual basis of the standard electron identification techniques are presented and compared to the alternative NN based particle classification.
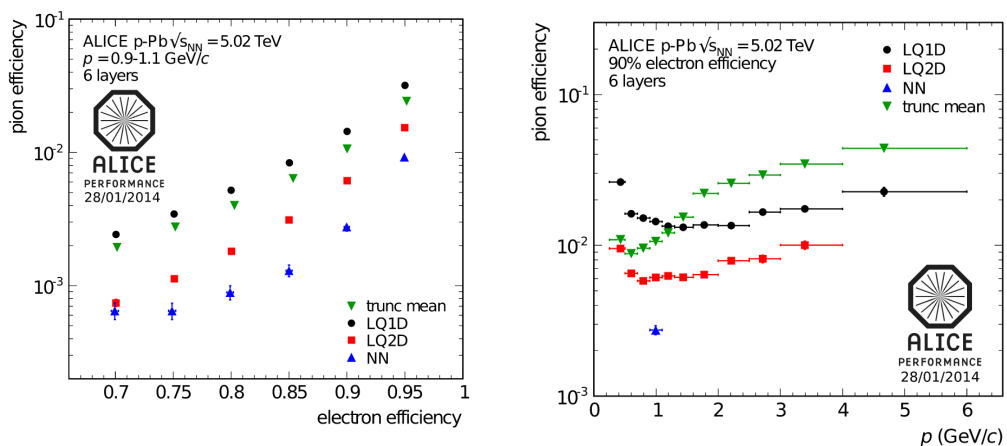

Figure 2.14: *Pion efficiency as a function of the electron efficiency for various TRD PID methods of tracks with a momentum in the range $0.9 \leq p \leq 1.1$GeV/c and signals in all 6 TRD layers (in p-Pb collisions at $\sqrt{s} = 5.02$ TeV) (left) and the pion efficiency at 90% electron efficiency as a function of the track momentum (right)*

The TRD is designed to provide electron-pion separation with a pion suppression factor of ≈ 100 for a particle momenta above 1 GeV/c. The general ansatz is to define the electron likelihood to be

$$\mathcal{L} = \frac{P_e}{P_e + P_\pi}, \tag{2.1}$$

where P_e and P_π are the respective layer-wise probabilities for a given particle with a given detector signal X_i to come from an electron or a pion.

$$P_{e/\pi} = \prod_{i=1}^{N_{\text{layers}}} P(X_i|e/\pi) \tag{2.2}$$

The detector signal in the simplest standard approach is given by the total integrated charge deposit of a particle (LQ1D). The integrated charge distributions are measured using (e.g. $K_s^0 \to \pi + \pi^-$) pions and electrons separately, normalized and interpreted as the respective probability density $P(X_i|e/\pi)$. By measuring the integrated charge for the first and the second half of the drift time separately and repeating the previous procedure the two-dimensional likelihood (LQ2D) method is defined.

The neural network approach uses the charge information of seven independent time slices. The general idea is based on previous work [41] and exploits a supervised learning approach. The interested reader may consult a introductory text book on Artificial Neural Network as e.g. [42]. Artificial Neural Networks (ANN) are one attempt to mimic the learning strategies of their biological counterparts. As neurons and synapses form the building-blocks of the hierarchical brain structure, a connected graph of artificial neurons form an ANN. The weighted edges of the graph are the equivalent of the synapses and the value of the assigned synapse weights reflect in a sense the current state of learning. The nodes of the graph are the neurons of the ANN. Each neuron is defined by a activation function and it is connected to one or several inputs via synapses. Each input is weighted by the synapse weight and presented to the activation function. The most commonly used activation functions are the Sigmoid $f(x) = (1 + \exp\{-x\})^{-1}$ and the hyperbolic tangent $f(x) = (1 - \exp\{-x\})(1 + \exp\{-x\})^{-1}$ functions, those output is calculated based on the weighted sum of all inputs.

The weights therefore can amplify or attenuate a certain input signal and define the output of the network. Neurons are arranged in a layered organization or architecture, Beside the input layer that presents each input values to all neurons in the first hidden layer an output layer presents the result of the internal computation. There may be more (Multilayer Network) than one (Monolayer Network) layers in the the hidden part of the network. Hidden refers to the circumstance that the respective layers are connected to neither the input layer nor the output layer and are thus isolated from the outside world. There are network topologies where each layer is connected only to
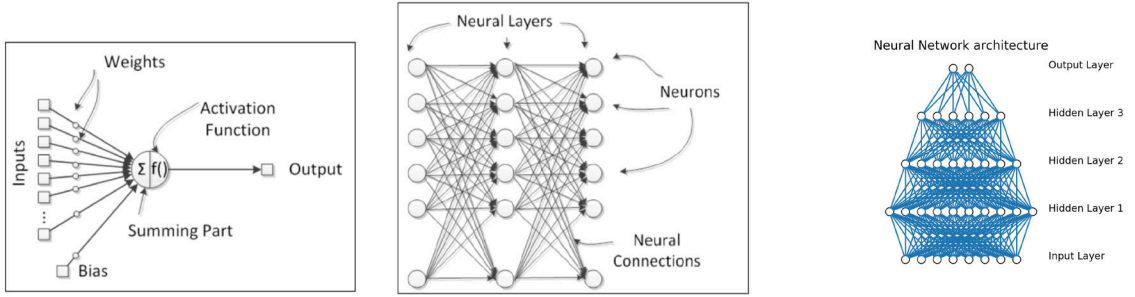
Figure 2.15: *Schematic view of an artificial neuron (left) and of the layered ANN topology(middle) [42]. Network topology (7:10:8:6:2) as implemented in this study (right).*

the following layer (Feed-Forward Networks) without connections of neurons within a layer and those that have connections to previous layers as well (Feedback Network.) In the presented study a Multilayer-Feed-Forward network is used with 7 input neurons, of those each represents integrated charge over a one (equal-time) time-slice of the TRD signal (c.f. figure 2.13). The input layer is followed by three layers of 10, 8 and 6 neurons and 2 output neurons. The two output neurons use the Soft-max function to provide a value between 0 (pions) and 1 (electrons) as a measure for the respective classification. The network is applied for each TRD layer in that a track provides a TRD signal and the resulting outputs are combined using the likelihood formula 2.2. The input dataset consists of preselected reconstructed tracks with their TRD signals obtained from pPb data set at $\sqrt{s} = 5.02$ TeV/c. The preselection is based on a cuts on the TPC number of sigma band obtained using the pion or the electron hypothesis ($-1 \leq N\sigma_{\mathrm{e}}^{\mathrm{TPC}} \leq 3$ and $-3 \leq N\sigma_{\pi}^{\mathrm{TPC}} \leq 1$) and an equivalent cut on the TOF number of sigma value ($-3 \leq N\sigma_{\mathrm{e}}^{\mathrm{TOF}} \leq 3$ and $-3 \leq N\sigma_{\pi}^{\mathrm{TOF}} \leq 3$). To train the network towards a good separation between electrons and pions it is presented with a subset of the preselected tracklets i.e. the TRD signal for one TRD layer. The output of the network is compared to the type of particle feed into the network, also encoded as 1 or 0. the deviation is propagated backwards through the structure of the ANN applying gradient-like changes to the existing synapse weights based on their impact to the final output. This procedure is therefore called back-propagation. With each training step the weights should ideally gradually assume values that minimize the deviation between the output and the presented known value. Special care has to go into the preparation of the input dataset (equal number of equivalent signal and background samples) and of the input values (e.g. normalization) to avoid biases in the trained network. Figure 2.14 shows the performance of the neural network approach in comparison with other PID methods. Often the performance is defined via the suppression of pions at an electron

efficiency $\epsilon_e = 0.9$. The efficiency is the fraction of electrons or pions of that that are presented to the PID method that are identified correctly, while the suppression is the inverse of the efficiency. The network was implemented using the Toolkit for Multivariate Data Analysis (TMVA [43]). Additionally several initial studies using deep convolutional multilayer neural networks in different topologies inspired by the "Inception-v4" network [44] were performed and implemented using the Caffee framework [45]. The resulting performance however was on par with the one obtained from the much simpler feed-forward design so the development was paused in favour of the jet analysis. While the details on deep convolutional networks (c.f. eg. [46]) would exceed the scope of this section, it can be said that they allow to automatically identify features based on the relation of different input variables. In case of an image e.g. strokes, colours or even complex entities as persons or trees. While the results of the initial studies support the previous results a deep neural network topology based on more input parameters than the seven time-slices might even surpass the current performance. Today there are several efforts within ALICE to include deep learning into many fields of the reconstruction and data analysis.
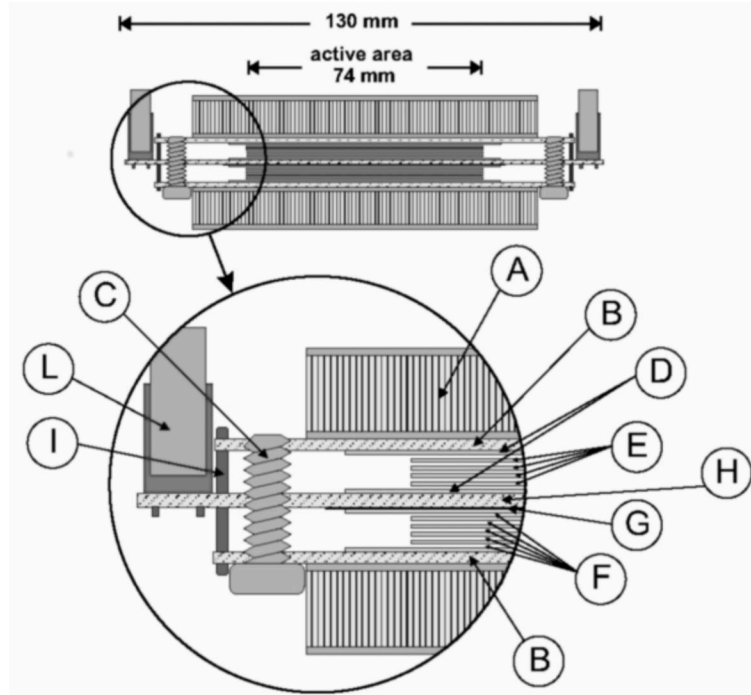
2.2.5 Time-Of-Flight Detector

Figure 2.16: *From [47]. Cross-section of the double-stack MRPC of the ALICE-TOF system. A: 10 mm thick honeycomb panel; B: PCB with cathode pick-up pads; C: M5 nylon screw to hold the fishing-line spacers; D: 550 μm thick external glass plates; E: 400 μm thick internal glass plates;F: five gas gaps of 250 μm; G: 250 μm thick Mylar film; H: central PCB with anode pick-up pads; I: pin to bring cathode signals to central read-out PCB; L: flat-cable connector (for MRPC signal transmission to the front-end electronics).*

The ALICE Time-Of-Flight detector (TOF)[48] is located at $370 \leq r \leq 399$ cm. It is segmented into 18 azimuthal SuperModules (SM) that are subdivided into five modules containing in total 1593 Multi-gap Resistive Plate Chamber (MRPC) strips. With its cylindrical surface of 141 m² it provides full azimuthal coverage in the pseudo-rapidity region of $-0.9 \leq \eta \leq 0.9$ and a intrinsic time resolution of less than 50 μs.

Each MRPC [49] is a stack of equally spaced 0.4 mm thick high-resistivity ($\approx 10^{13}\Omega$cm) soda-lime glass plates with an electric field of ≈ 100kV/cm applied to its surfaces. The gap region is 250 μm wide and filled with a mixture of 93% $C_2H_2F_4$ and 7% SF_6 forming the avalanche region while the glass plates acts as a barrier restricting the size of the avalanche even at high external field strengths. Two stacks are combined via a connecting central anode. The readout is realized via 96 2.5×3.4 cm² pads, placed on the external plates, providing 152928 channels in total. Due to its fine granularity the TOF has been used as trigger detector for cosmic events and ultra-peripheral collisions(UPC).

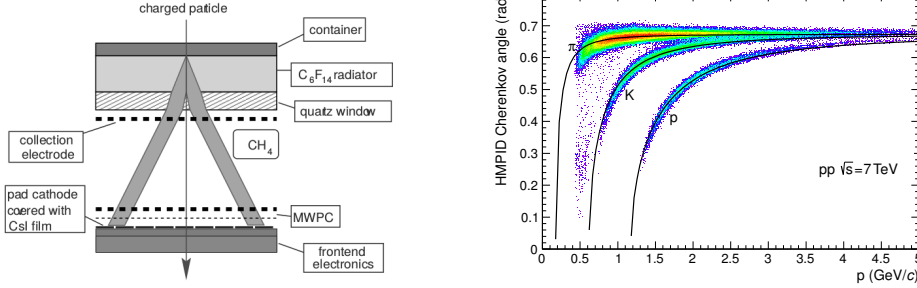### 2.2.6   High Momentum Particle Identification Detector

Figure 2.17: *Working principle of the HMPID RICH [50](left), HMPID PID performance for proton-proton collisions at $\sqrt{s} = 7\,TeV$ [34](right).*

The ALICE High Momentum Particle Identification Detector (HMPID) consists of seven proximity-focusing Ring Imaging Cherenkov (RICH) counters based on MWPC with CsI (300 nm with a quantum efficiency off 25% at 175 nm) coated readout pads. Each counter module is covered by a 15 mm radiator layer of (perfuorohexane) C_6H_{14} liquid with an index of refraction of n= 1.02989 at 175 nm that corresponds to a momentum threshold of $p^{\text{thres.}} = 1.21 \times \text{mass}(\text{GeV/c})$. The MWPC uses CH_4 at atmospheric pressure providing a gas gain of $\approx 4 \times 10^4$ Particles with velocities larger than the speed of light in the radiator will produce Cherenkov photons detected by the read out pads of the MWPC. HMPID is optimized for particle identification in the intermediate momentum range from $1 - 3$ GeV/c pions and kaons and from $1.5 - 5$ GeV/c for protons.

Year	TRD $|\eta| < 0.8$	PHOS $|\eta| < 0.12$	EMCal $|\eta| < 0.7$
2008	4	1	0
2009	7	3	2
2010	7	3	2
2011	10	3	5
2012	13	3	5
2013	13	4	5
2015ff	18	4	12

Table 2.8: *Number of sectors (20 ° in azimuth each) of the central barrel covered by TRD, PHOS, and EMCal in the first years of ALICE running.*

2.2.7   Photon spectrometer

The ALICE PHOton Spectrometer (PHOS)[51][18] is located at the bottom of the AL-ICE central barrel at a distance of 4.6 m from the nominal interaction point. It covers

the pseudo-rapidity region from $-0.12 \leq \eta < 0.12$ and the azimuthal angle from 220° to 320°. It is segmented in 5 modules of 3584 detection cells, consisting of separate $22 \times 22 \times 180$ mm^3 PbWO$_4$ crystals coupled to 5×5 mm^2 APD. Each module is equipped with a Charged-Particle Veto (CPV) detector, a MWPC with an active volume of 14 mm thickness filled with an mixture of Ar/CO$_2$ mixture that is attached at a distance of 5 mm from the PHOS module surface. PHOS main objectives, as stated in the Technical Design Report, are the study of thermal and dynamical parameters of the initial phase of the collision, in particular the initial temperature, via direct single photons and di-photons, jet quenching as a probe of de-confinement, studied via high momentum π^0 and the search for signals of chiral restoration. Since 2011 [52] PHOS contributes a high energy (90% efficiency with 36% purity at $E_{\text{thres.}=4.3}$) cluster trigger (see. section 2.2.16) to the level-0 and level-1 trigger is in development to improve the cluster energy estimation

2.2.8 Electromagnetic calorimeter

The ALICE Electromagnetic Calorimeter (EMCal) is located at a radial distance of 4.5m from the beam line in between the ALICE space-frame and the L3 magnet. In its full configuration it covers 107 degrees in azimuthal direction ($80° - 187°$) and a pseudo-rapidity region of $-0.7 \leq \eta \leq 0.7$. EMCAL is a sampling calorimeter based on the Shashlik[53] technology and consists of 12288 towers that are arranged into 2×2 tower modules made from layered Pb-scintillators [54]. Each tower consists of 77 layers of 1.44 mm Pb and 1.76 mm of scintillator with longitudinal wavelength shifting fibres constituting a radiation length of ≈ 20.1. The towers are arranged into EMCAL SuperModules 10 full size modules composed of 12×24 modules spanning 20° in azimuth and 0.7 in η and two one-third size modules composed of 4×24 modules that cover 7° in azimuth. The modules are titled to minimize the angle of incidence to 2° in η and 5° in ϕ. The tower-wise readout is realized via avalanche photodiodes coupled to charge sensitive preamplifies. During the 2010 proton-proton data taking only two super modules were installed.

2.2.9 VZERO

The ALICE VZERO system consists of two scintillator arrays arranged collinear around the beam line at varying distances, VZERO A at $z = 329$ cm opposite to the muon spectrometer and VZERO C at $z = -86$ cm — -88 cm fixed to the hadronic absorber of the muon spectrometer arm. Each array consists of four concentric rings [55]. The VZERO system [56] provides the experiment with a minimum bias trigger (MB) that, until the
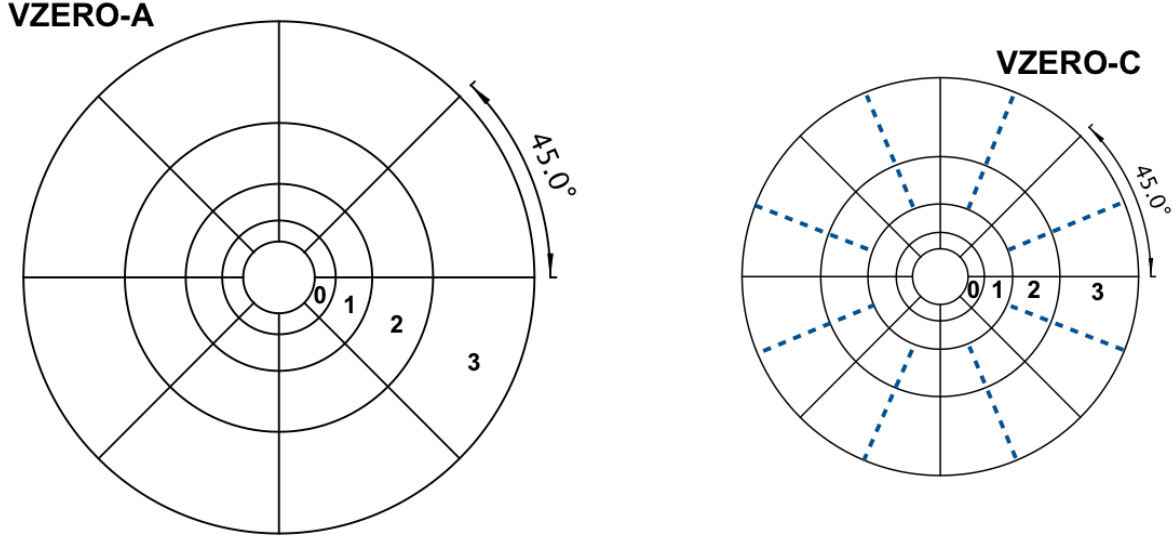
Figure 2.18: *From [50]: Sketches of VZERO-A and VZERO-C arrays showing their segmentation. Scintillator thicknesses are 2.5 and 2 cm respectively. Radii of rings are given in Tab. 2.9.*

Ring	VZERO-A				VZERO-C			
	$\eta_{\max}/\eta_{\min}$	$\theta_{\min}/\theta_{\max}$	$r_{\min}/r_{\max}$	z	$\eta_{\min}/\eta_{\max}$	$\theta_{\max}/\theta_{\min}$	$r_{\min}/r_{\max}$	z
0	5.1/4.5	0.7/1.3	4.3/7.5	329	-3.7/-3.2	177.0/175.3	4.5/7.1	-86
1	4.5/3.9	1.3/2.3	7.7/13.7	329	-3.2/-2.7	175.3/172.3	7.3/11.7	-87
2	3.9/3.4	2.3/3.8	13.9/22.6	329	-2.7/-2.2	172.3/167.6	11.9/19.3	-88
3	3.4/2.8	3.8/6.9	22.8/41.2	329	-2.2/-1.7	167.6/160.0	19.5/32.0	-88

Table 2.9: *Pseudorapidity, angular acceptance (deg.), radius (cm) and z (cm) position along the beam axis of VZERO-A and VZERO-C median plane rings, as seen from the origin of the coordinate system.*

end of the 2010 data taking period, was defined as MBOR ≡(SPD hit || VZEROA || VZEROC). Due to higher LHC luminosity and beam background the requirement was changed in the 2011 and 2012 proton-proton runs to MBOR ≡ (SPD hit || VZEROA || VZEROC) and (LHC Bunch crossing signal or from a triggering detector). In the Pb–Pb runs the following condition had to be fulfilled to generate the interaction trigger: (Two pixel hits in the outer layer of the SPD) || VZEROA || VZEROC. By the end of 2010 this again was changed again to (SPD hit || VZEROA || VZEROC). From 2011 three triggers were issued i. VZERO A || VZERO C, ii. 0-50% centrality and iii. 0-10% centrallity.

VZERO also provides the measurement of the integrated luminosity[57] for the ALICE experiment and of the invariant inelastic proton-proton cross section. Further more it can be used as a centrality indicator in heavy-ion runs.
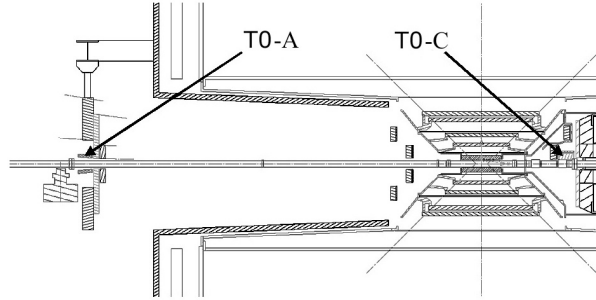
2.2.10 T0

Figure 2.19: *The layout of the T0 detector arrays inside ALICE [58].*

The T0 detector system consists of two fast Cherenkov counter arrays T0-A and T0-C located at z= 375 cm and z= −72 cm. T0-A covers the pseudo-rapidity range of $4.61 \leq \eta \leq 4.92$ and T0-C $-3.28 \leq \eta \leq -2.97$ T0 generates the T0 signal for the TOF detector with a precision of 50 ps, it measures a rough vertex estimate provides a first level trigger and helps to discriminates beam-gas interactions.

2.2.11 Photon Multiplicity Detector

The Photon Multiplicity counter (PMD) [59, 60] is a high-granularity pre-shower detector with full azimuthal coverage covering $2.3 < \eta < 3.9$ z= 361.5 cm. The PMD consists of two detector planes with a separating lead converter. The interaction point facing detector plane acts as a charged particle veto. The PMD measures the multiplicity and spatial distribution of photons and allows to estimate the event plane.

2.2.12 Forward Multiplicity Detector

The Forward Multiplicity Detector (FMD) [61, 56] consists of 51200 silicon strips arranged in 5 rings placed around the beam pipe covering $-3.4 < \eta < 5.1$ providing a high resolution charged particle multiplicity determination, measurement of the event-plane inclination and independent measurement of the elliptic flow v_2.

Ring	Azimuthal sectors	Radial strips	z [cm]	r range [cm]	η coverage
FMD1	20	512	320	$4.2 - 17.2$	$3.68 - 5.03$
FMD2i	20	512	83.4	$4.2 - 17.2$	$2.28 - 3.68$
FMD2o	40	256	75.2	$15.4 - 28.4$	$1.70 - 2.29$
FMD3i	20	512	-75.2	$4.2 - 17.2$	$-2.29 - -1.70$
FMD3o	40	256	-83.4	$15.4 - 28.4$	$-3.40 - -2.01$

Table 2.10: *Physical dimensions of Si segments and strips[61].*

2.2.13   Zero-Degree Calorimeter

The Zero-Degree Calorimeter (ZDC) is composed of two calorimeter array located at $z = \pm 115$ m. Each of ZDC arrays consists of a proton calorimeter (ZP) and a neutron calorimeter (ZN) along the beam line. The ZN's are installed at zero degree with respect to the beam axis and the ZP's externally to the outgoing beam pipes. Two electromagnetic calorimeters located at $z = 7.35$ m covering a pseudo-rapidity of $\pm 4.8 < \eta < \pm 5.7$. The ZDCs are quartz-fibre spaghetti calorimeters with optical fibres embedded in a dense absorber (Tungsten-alloy for ZN, Brass for ZP). The ZN and ZP calorimeters are mounted on a remotely controllable platform to follow the beam crossing angle.
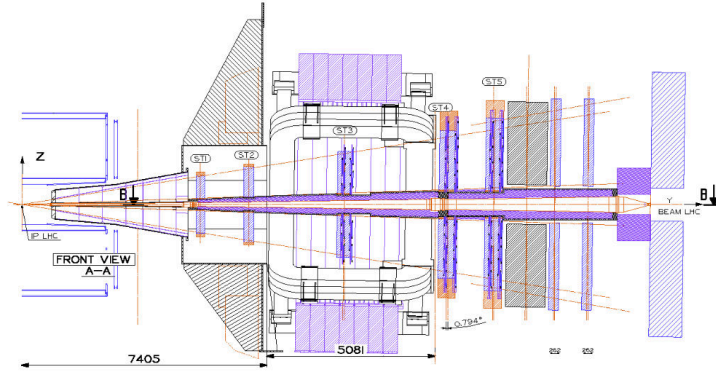
2.2.14   MUON spectrometer

Figure 2.20: *Schematic view of the ALICE muon arm [38].*

The muon spectrometer [62, 38] covers the forward pseudo-rapidity region $-4.0 \leq \eta \leq -2.5$. It consists of a 4.13 m
i.e. $z \in (-5030 \text{ mm}, -900 \text{ mm})$ passive carbon-concrete front absorber and stainless steel-tungsten-Lead beam shield surrounding the beam pipe followed by a high-granularity 10 layer tracking system. The tracking system is made of five planes of cathode pad chambers (CPC) filled with a 80%Ar-20%CO_2 mixture with a gain of $\sim 10^4$ at 1650 V and spatial resolution of ≈ 100 μm. Two stations are arranged before a large dipole magnet, one within and two after it providing 1.1 million read-out channels. The tracking system is followed by a ≈ 1.2 m thick iron-made muon filter and four layers of trigger chambers. The Trigger system is build from four planes of resistive plate chambers (RPCs) each consisting of 18 RPC modules with an individual area coverage of about 70×300 cm^2 covering ~ 140 m^2 in total and providing ~ 21000 readout channels. It provides p_T based muon selection triggers, single muons and like-/unlike-sign muon pairs.

2.2.15 A Cosmic Ray Detector (ACORDE)

The ALICE (A) Cosmic Ray Detector (ACORDE) consists of 60 plastic scintillator modules consisting of two plastic scintillator paddles with an active area of $190 \times 19.5 \text{ cm}^2$ arranged in a doublet configuration where every doublet consists of two superimposed scintillation counters and photo multipliers. A trigger signal is issued on a coincidence hit in two paddles within 40 ns providing a fast cosmic L0 trigger.

Cosmic particle triggers (see [63] for more details) are an essential ingredient for detector alignment e.g. [38].

2.2.16 The ALICE Trigger Central System

ALICE is designed and build to operate as a triggering detector. The idea of a trigger is the ability to select events with predefined technical or physics features.

The ALICE trigger system includes three hardware trigger levels L0, L1 and L2, the so-called TRD pre-trigger and the High Level Trigger (HLT). The neuralgic point of this system is the Central Trigger Processor (CTP). The CTP makes decisions based on the input of the respective triggering detectors and sends them to Local Trigger Units (LTU) of the different detectors thus providing an interface between the CTP the respective sub-detector readout.

The CTP logic is organized in clusters and 50 independently programmable trigger classes, where the latter forms the basic processing structure. A trigger class provides the basis of any trigger decision and is realized as a logical AND from all the 24 trigger inputs at each level (12 at L2)

A designated group of sub-detectors forms a cluster. A trigger class is connected to such a cluster requiring the read-out of the corresponding detectors before the class is activated. The earliest signal is the so called TRD pre-trigger that triggers the TRD electronics wake-up about 100 ns after the collision. The Pre-Trigger is composed of signals from the T0, VZERO and the TOF. The pre-trigger is followed by the L0 signal that is sent to the different detectors 1.2 μs after the collision. The quasi-constant latency and propagation time of the signal is used to calculate the interaction time. As only the fast detectors are in a ready state at the time of the L0 signal a second L1 signal with a latency of 5.5 μs is issued 5.3 μs later to collect the remaining inputs from the slower detectors and to initialize data conversion and buffering for the fast detectors. The consecutive L2 level is implemented to avoid pile-up events. Due to the 88μs TPC drift time there may be charge clusters not only from current event but also from previous or following events in the drift volume. The CTP therefore employs a past-future protection by rejecting any other events in a ± 88 μs time window around

No.	Det.	Description	Pb-Pb	pp	No.	Det.	Description	Pb-Pb	pp
1	MTR	DM like high p_T	*	*	21	TOF	High Multiplicity		*
2		DM unlike high p_T	*	*	22	V0	VO1		*
3		DM like low p_T	*	*	23		VO2	*	*
4		DM unlike low p_T	*	*	24		VO3	*	*
5	DM single	*	*		25		VO4	*	*
6	T0	T0 vertex	*	*	26		VO5		
7		T0C		*	27	TRD	Pretrigger		
8		T0A		*	28		TRD2		
9		T0 sc	*		29		TRD3		
10		T0 ce	*		30		TRD4		
11	PHO	PHOS signal	*	*	31		TRD5		
12	ZDC	ZDC diss. single arm	*		32	SPD	SPDMB		*
13	EMC	EMCAL single shower	*	*	33		SPD2		
14	ACO	ACORDE single muon	*	*	34		SPD3		
15		multi-muon	*	*	35		SPD4		
16	TOF	cosmic vert. muon	*	*	36		SPD5		
17		cosmic multi-muon	*	*	37		SPD6		
18		MB		*	38		SPD7		
19		ultraperipheral (ρ)		*	39		SPD8		
20		ultraperipheral (J/Ψ)		*	40		SPD9		
					41		SPD10		

Table 2.11: *From [18]: Available L0 trigger inputs in pp and Pb-Pb*

the current event. In Pb-Pb collisions the maximal number of events is increased to 4 for peripheral events and no additional semi central event in a 176μs window. Apart from the TPC also the other detectors are embedded into the past-future protection. In case of the of the ITS a additional $\pm 10\mu$s window is checked. If the event is past-future safe the L2 decision is send from the CTP marking the event as good for data acquisition. Detector specific trigger message are issued on levels L0 and L1.

No.	Det.	Description	Pb-Pb	pp
1	PHO	PHOS low E_T	*	*
2		PHOS med E_T	*	*
3		PHOS high E_T	*	*
4	TOF	jet trigger		*
5	TRD	TRD1	*	*
6		TRD2	*	*
7		TRD3	*	*
8		TRD4	*	*
9		TRD5	*	*
10		TRD6	*	*
11	ZDC	ZDC mb	*	*
12		ZDC sc	*	*
13		ZDC ce	*	*
14		ZDC diss.	*	
15	EMC	EMCAL single shower low	*	*
16		EMCAL single shower med	*	*
17		EMCAL single shower high	*	*
18		EMCAL jet	*	*

Table 2.12: *From [18]: List of L1 trigger inputs for Pb-Pb and pp collisions.*

Number	Description	Condition
1	MB1	V0or $\oplus$ PIXELor $\odot$ BEAMGASor
2	MB2	V0or $\odot$ PIXELor $\odot$ BEAM$\overline{G}$ASor
3	MB3	V0and $\odot$ PIXELor $\odot$ BEAM$\overline{G}$ASor
4	BG	BEAMGASor
5	BGDM	BEAMGASc
6	DMsingle	DMsingle
7	DMBeamgas	BGc $\odot$ DMsingle
8	DML	DMLikeLow
9	DMU	DMUnlikeLow
10	DMMBSingle	MB1$\oplus$ DMsingle
11	DMMBLike	MB1$\oplus$ DMLikeLow
12	DMMBUnlike	MB1$\oplus$ DMUnlikeLow
13	Photon1	MB1$\oplus$ L0PHOSMB
14	Photon2	MB1 $\oplus$ L0PHOSLE
15	Photon3	MB1 $\oplus$ L0PHOSHE
16	Photon4	MB1$\oplus$ L0PHOSIP

Table 2.13: *From [18]: List of trigger classes with trigger conditions.*

2.2.17   The High-Level Trigger

The High-Level Trigger (HLT) is a dedicated computing farm subdivided into 117 Front End Processor(FEP), 84 Compute Nodes(CN) and 4 portal machines.
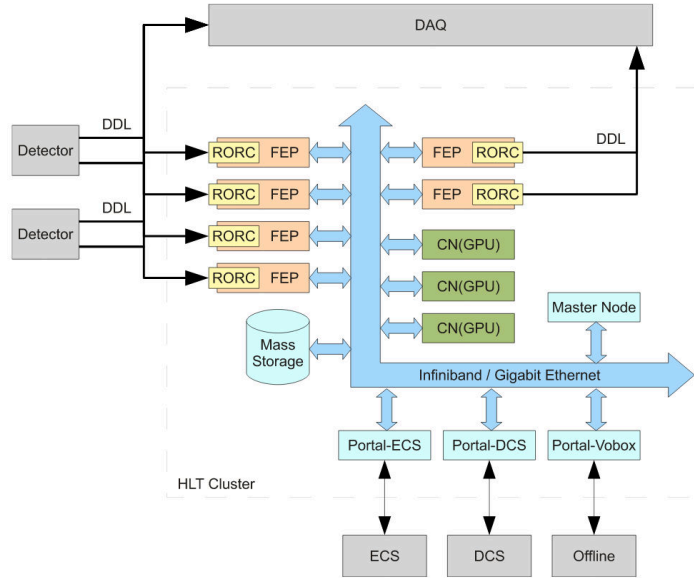

Figure 2.21:   *From [64]: Schematic diagram of the HLT's architecture indicating connections from detectors, to DAQ, other external services and internal network connections.*

During Pb-Pb operation the data rate can reach up to 25 GB/s while the data acquisition is limited to about 4GB/s bandwidth. Therefore advanced data compression algorithms are implemented in the HLT. The HLT also allows to define trigger criteria and Regions of Interest within a given event, based on the full reconstruction information.

2.2.18   ALICE data acquisition system

The ALICE Data Acquisition System (DAQ) is closely inter-weaved with the previously discussed trigger system. For every bunch crossing the CTP trigger decisions are distributed via the sub-detectors LTUs that are themselves connected to the respective Front-End Read-Out electronics (FERO) via the local Timing, Trigger and Control (TTC) system. Given a positive trigger decision i.e. L2a (L2 accept) the data from the detectors is transferred via optical Detector Data Links (DDL) to the PCI-X based DAQ Readout Receiver Cards (D-RORC) hosted in a Local Data Concentrator (LDC). With L2a the bunch crossing and the orbit number, are send as well as the trigger type , a cluster list and a list of active trigger classes to identify the respective event
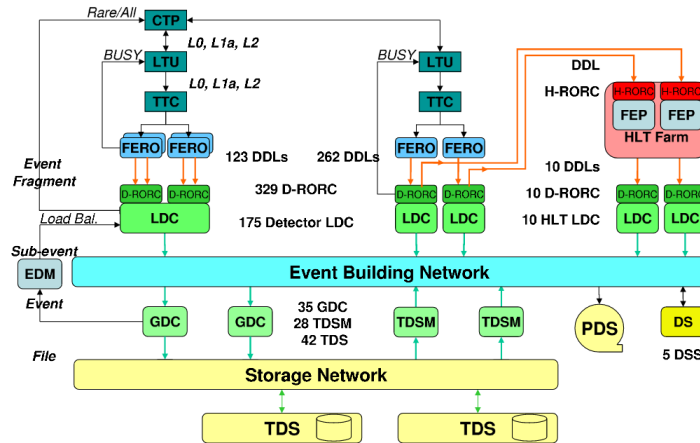
Figure 2.22: *The overall architecture of the ALICE DAQ and the interface to the HLT system[18].*

as well as to remove pile-up events and to select the detectors that are needed to be read out. The DDL a bandwidth of 200 MB/s. In the LDC different event fragments are assembled into first sub-events. These sub-events are then forwarded to a farm of Global Data Collectors (GDCs) where the different sub-events are combined into the final event. During the event building, the distribution of sub-events to different GDCs is automatically optimized by a data-driven algorithm to optimize the load on the GDC farm. The monitoring of the GDC network is done by the Event-Destination manager (EDM) while the data distribution from the LDCs to the GDCs is organized via standard TCP/IP network infrastructure the Event Building Network. The HLT receives copies of the raw data via optical DDL and the HLT Readout Receiver Cards (H-RORC) then available at the Front-End Processors (FEP).

The data at the GDCs is organized into fixed size files, registered at the ALICE Grid software and transferred via the Fibre Channel 4 gigabit/s storage network to the Transient Data Storage(TDS). The data is then exported to the computing centre by the TDS movers (TDSM) and recorded to the Permanent Data Storage (PDS).

2.2.19   The ALICE event reconstruction

For an further details on the following paragraphs see [65, 18]. After cluster finding in all of all sub-detectors namely ITS, TPC, TRD, TOF HMPID and PHOS the primary event vertex position is estimated using the clusters in the two SPD layers. Here a pair of two clusters in both layers of the SPD in the transverse plane is selected requiring a small azimuthal distance $\Delta\phi$ and used to calculate a initial estimate on the primary vertex position via linear extrapolation based on the clusters reconstructed z coordinates. The
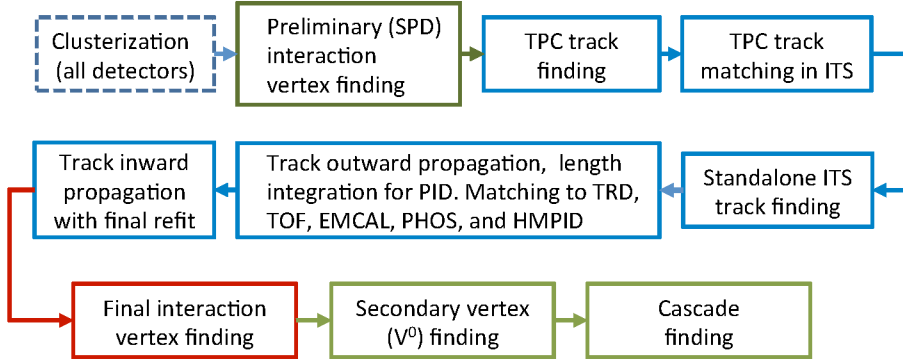
Figure 2.23: *ALICE event reconstruction flow [34]*

primary vertex resolution depends on the track multiplicity resulting in longitudinal vertex resolutions of $\sigma_z^{Pb-Pb} \approx 10$ μm and $\sigma_z^{pp} \approx 150$ μm.

Track finding starts at the outer TPC radius exploiting the low track density and the good spatial resolution of the sub-detector. The available clusters are combined into candidate tracks the so called "seeds".
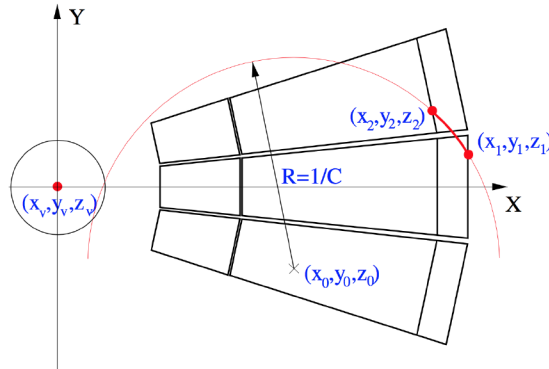

Figure 2.24: *Track-finding coordinate system, track parameters and the schematic view of the 'seeding' with the vertex constraint [65].*

Starting from the a pad row i close to the outer TPC surface and one closer to the vertex j separated by e.g. $i - j = 20$ rows. With the primary vertex constraint the possible p_T and z-direction pairs of compatible clusters are combined. For these combinations a first initial helix parametrization though the primary vertex and both cluster positions is constructed. If a additional cluster compatible with the helix approximation is found at pad row $k = j - (i - j)/2$ the helix serves the initial track parameter estimates. The covariances are constructed from cluster point uncertainties and a initially large spatial vertex uncertainty. The initial track parametrization is used as a model for the Kalman filter procedure starting from the outer pad row i to the inner pad row j. If half of possible points in the rows between i and j are successfully assigned to the track candidate

it is called a seed . The assignment decision is done based on their compatibility $\mathcal{O}(4\sigma)$ of a cluster in the next inner row defined by the local covariance matrix, modified by a noise term to account for external uncertainties, of the track candidate at this iteration step. On successful assignment the local track state vector and its covariance matrix are updated. This procedure is repeated until the inner-most layer. This procedure less desirable for any analysis looking for tracks from secondary particles as the primary vertex introduces a strong bias favouring primary tracks. Therefore a second independent pass is executed without the primary vertex constraint.

Once the candidate tracks are propagated to the inner TPC radius the tracking continues in ITS starting with the highest momentum tracks to reduce the number of ambiguously assigned ITS clusters. where the track is propagated to primary event vertex and compatible clusters are added to further constrain the track parameters. For the previously primary constraint tracks two independent propagations are done one again constrained by the primary vertex and one without the constraint. Whenever more than one compatible cluster is found all possible combination are treated as independent hypotheses. And a minimal χ^2 criterion is used to select valid candidates after full propagation. Optionally a weighted χ^2 criterion can be introduced to account for cluster sharing and missing layers. For previously secondary TPC track candidates only the unconstrained pass is executed.

In the next step the tracks are propagated outward using a reverse Kalman step to assign space points in the TRD, the TOF, the CPV (PHOS) and minimal ionizing clusters in the HMPID also removing incompatible outliers. Subsequently a additional ITS stand-alone track finding is performed on the unassigned clusters in the ITS to find tracks of particles that were not reconstructed in the TPC due to detector inefficiencies, the momentum cut-off or decay.

Lastly the tracks are propagated inwards to the primary vertex or the smallest available radius in case of secondary particles to obtain the track parameters close to the interaction point. In the next step the primary vertex position is recalculated based on the reconstructed track parameters resulting a precision of 110 μm in z-direction and 70 μm in xy for an pp event with average track multiplicity.

The primary vertex recalculation is followed by the online V^0 finding step.

Here the term V^0 is synonymous for neutral particles decaying into charged opposite-signed daughter particles and it is derived from the characteristic V-shape of the reconstructed tracks. In this step secondary decay vertices, mostly from strange particle, are reconstructed by combining opposite-signed widely-displaced tracks in a fiducial volume around the primary vertex ($\mathcal{O}$), based on their distance-of-closest approach (DCA). The
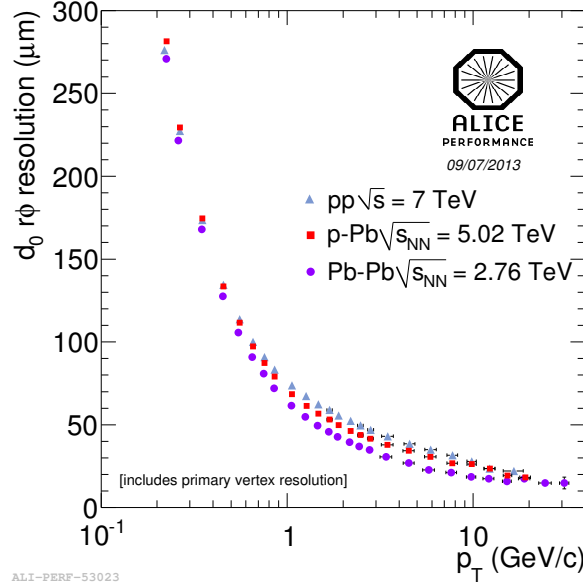
Figure 2.25: *Transverse impact parameter resolution in different collision systems.*

resulting particles momentum, calculated by the sum of both daughter momenta, has to point to the primary vertex in order for it to be accepted (cut on cosine of pointing angle).

The cascade ($\Omega^{\mp}, \Xi^{\mp}$) finding: As in the previous step all V^0 candidates are considered with a relaxed pointing angle requirement. First all V^0 with a large impact parameter are selected and all candidates within the Λ mass window are combined with all possible secondary tracks and accepted if the DCA between the secondary track interpolation and the straight line interpolation of the V^0 is small. Finally the momentum of the resulting cascade candidate has to point back to the primary vertex for the candidate to be accepted. ALICE furthermore provides the reconstruction of kinks (1-prong decays) to allow the identification of kaons in a wide momentum region.

Finally two kink reconstruction steps are performed. Kinks with a large decay angle are reconstructed by the multi-step combination of tracks that do not completely traverse the TPC. The initial decision is made by a small z-DCA and the full secondary vertex is reconstructed in the following numerical minimization passes. Only kinks within the fiducial volume defined by the track accuracy are kept and the pair of tracks is refitted to the kink vertex. In case of ambiguous track possibilities only the best defined track are selected. In the next step (small angle kink finding) tracks with less than 1.4 GeV/c belonging to any of the kick candidates or tracks that share more than half of their clusters with a track associated with a kink or have less than 80 clusters are rejected. For all remaining tracks the relative change within the last 20 pad-rows in direction is
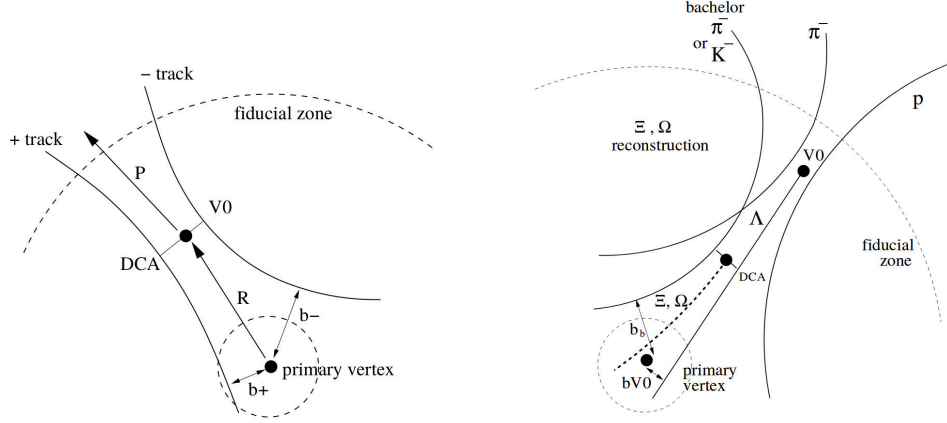
Figure 2.26: *Schematic view [65] of ALICE (left:) V0 reconstruction, (right:) cascade reconstruction*

locally estimated to estimate the position of the breaking-point i.e. the point of the maximum change in direction. A set of cuts is applied to maximize the kink quality and to suppress kinks from virtual decays.

This completes the central barrel tracking. The MUON system provides additional track reconstruction capabilities based on the input from the tracking and the trigger planes. Since the MUON arm is only relevant for special analyses it would go beyond the scope of this review. The reader may be referred especially to [65].

2.2.20   The ALICE track impact parameter definition

As being the observable of interest in the presented analysis, this section outlines the ALICE track impact parameter definition.

It is defined as the distance of closes approach (DCA) of a reconstructed track to the reconstructed primary event vertex. The transverse impact parameter is the projection of the impact parameter vector onto the xy-plane, omitting the z component. Each reconstructed track in ALICE is represented by a parametrized helix description using a set of five track parameters $\mathcal{P} = (y, z, \sin(\phi) = \frac{p_y}{p_T}), \tan(\lambda) = \frac{p_z}{p_T}), \pm \frac{1}{p_T})$. Within the ITS the local coordinate system Σ_{local} is rotated by the angle α around the z-axis in such way that both, the point of closest approach and primary vertex lie on the rotated y-axis. Technically, the y-difference of the DCA[1] and the primary vertex in Σ_{local} defines the $r\varphi$-component of the impact parameter and its sign. Expressed in the tracks local curvature radius ρ and the track position at the DCA (x_0, y_0, z_0) and the

---

[1]Synonymously used at some points in this thesis
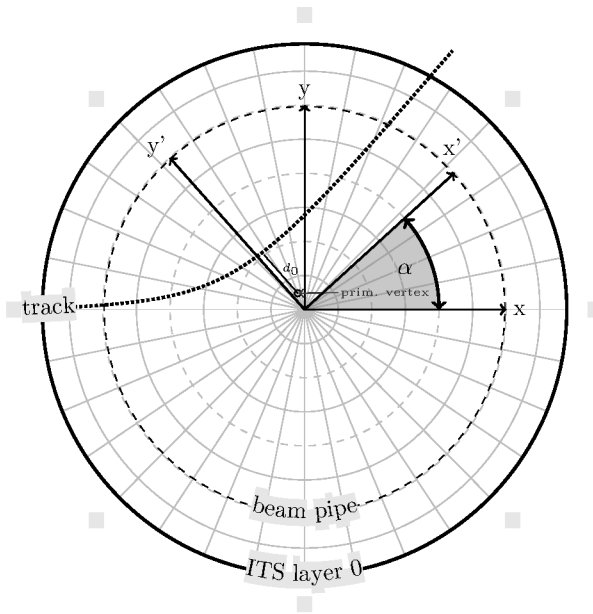
Figure 2.27: *Impact parameter definition in ALICE d_0: transverse impact parameter, α: local coordinate rotation angle*

vertex coordinate (x_V, y_V, z_V):

$$d_0 = \rho - \sqrt{((x_V - x_0)^2 + (y_V - y_0)^2)}$$
$$d_z = z_0 - z_V \tag{2.3}$$

2.2.21   The ALICE analysis software AliRoot

ALICE uses the AliRoot framework for reconstruction, simulation and analysis. AliRoot is an extension of the ROOT (version 5) data analysis framework [66] the successor of the long discontinued former (Physics Analysis WorkStation) PAW[67][68] framework. ALIROOT is a highly modular software development framework written in C++ with interfaces to other programming languages as Fortran, R or Python (PyRoot). The underlying ROOT system provides full C-macro support via the CINT C++ interpreter (replaced by clang from ROOT version 6 onwards) mainly used for interactive tasks as configuration procedures, data visualization or quality assurance. In general, each object of experimental interest e.g. a detector module or a complex physics analysis are implemented as a C++ classes inheriting from common ROOT base classes. Physics Data is stored via optimized container classes providing a hierarchical folder structure. This strongly object oriented approach combined with clear coding conventions enables efficient programming while maintaining the independence of the different sub-modules. AliROOT in combination with GEANT3 provides classes that allow to model each sub-detector of ALICE and therefore to simulate Monte Carlo events including there
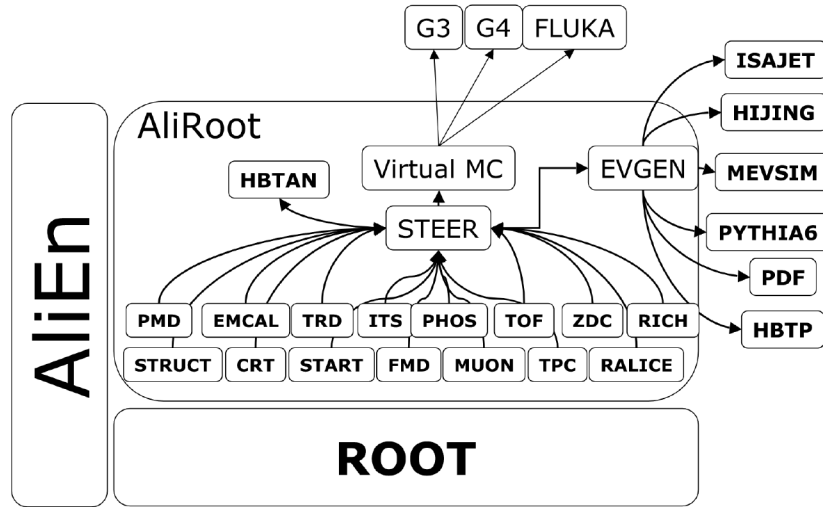
Figure 2.28: *Schematic structure of the ALICE analysis software (ALIRoot) [18].*

detector response, that can then be used as a reference for studies based on actual measurements. The input for the detector simulation can come from various event level generators as PYTHIA, HERWIG, HIJING, SHERPA or POWHEG.

ALIROOT was later split into AliRoot for all modules containing low level functionality i.e. detector specific functions for event reconstruction or functions for data handling and AliPhysics containing the user physics analyses. ALIROOT provides an interface to the AliEn[69] (ALICE Environment Grid) framework. It provides distributed processing resources used for reconstruction, simulation and data analysis. Different analysis modules can be chained in so called LEGO[70] (Lightweight Environment for Grid Operators) trains to minimize io and data preparation overhead.
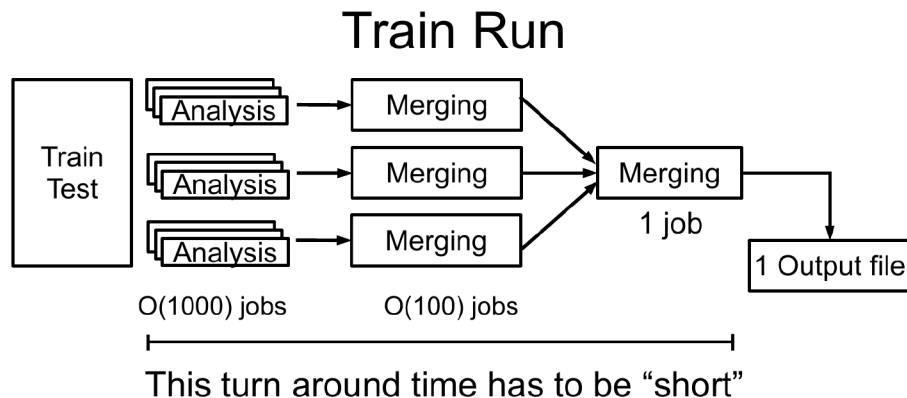
Figure 2.29: *From [70]: Procedure of a LEGO train run. After the train test the analysis jobs run. Then the results are merged into a single output file. The time to complete this procedure is called the turn around time.*

Chapter 3

Theoretical background

> *"The time has come," the walrus said, "to talk of many things: Of shoes and ships - and sealing wax - of cabbages and kings"*
>
> —— Lewis Carroll, *Through the Looking-Glass*

This chapter aims to motivate the theoretical treatment of Heavy Quark production based on the framework of Quantum Chromodynamics (QCD). For a deeper mathematical treatment of the presented topics the reader is encouraged to review indicated references in addition to a good textbook on quantum field theory e.g. [71].

3.1 Introduction: The Standard Model

The Standard Model (SM) of particle physics is the mathematical description of the the strong, the electromagnetic and the weak interaction as well as the Higgs field Yukawa-interaction. The theory includes the six fundamental spin 1/2 fermions, the quarks and leptons as well as the complex Higgs doublet $\mathcal{H}$.

Quarks come in six flavours $f_{flv} = u, d, s, c, b, t$ (up , down, strange, charm, bottom and top) and three colours $f_c = r, g, b$ (red, green, blue). Quarks and leptons can be arranged in three families or generations (see table 3.1).

Quarks Flavour	charge q	mass m	Leptons Flavour	charge q	mass m
u	+2/3 e	≈ 2.5 MeV$/c^2$	e	-1 e	0.511 keV$/c^2$
d	-1/3 e	≈ 5 MeV$/c^2$	ν_e	0 e	≤ 2 eV$/c^2$
c	+2/3 e	≈ 1.3 GeV$/c^2$	μ	-1 e	105.7 MeV$/c^2$
s	-1/3 e	≈ 100 MeV$/c^2$	ν_μ	0 e	≤ 0.19 MeV$/c^2$
t	+2/3 e	≈ 173 GeV$/c^2$	τ	0 e	1.776 GeV$/c^2$
b	-1/3 e	≈ 4.2 MeV$/c^2$	ν_τ	-1 e	≤ 18.2 MeV$/c^2$

Table 3.1: *Fundamental leptons and quarks of the Standard Model [72] .*

It is a quantum field theory based on the gauge group [71].

$$\mathbf{G} = SU(3)_{colour} \otimes SU(2)_L \otimes U(1)_Y \tag{3.1}$$

The $SU(3)_{colour}$ subgroup gives rise to eight massless bosons, the gluons, that mediate the strong interaction between quarks and anti-quarks. The subgroup $SU(2)_L \otimes U(1)_Y$ of the weak isospin and hypercharge Y describe the electro-weak interaction, that is spontaneously broken down to electromagnetic $U(1)_{em}$ symmetry by the non-vanishing vacuum expectation value of Higgs field $\langle \mathcal{H} \rangle \neq 0$ (Brout-Higgs-Englert mechanism) generating masses for the $W^{\pm}$ and Z^0 bosons while leaving the photon massless. The properties of the gauge bosons are listed in table 3.2.

Gauge boson	Interaction	charge q	mass m
g	Strong	0	0
γ	Electromagnetic	0	0
$W^{\pm}$	Weak	$\pm 1e$	80.385 ± 0.015 GeV/c^2
Z	Weak	0	91.1876 ± 0.002 GeV/c^2
H^0	Yukawa	0	125.09 ± 0.24 GeV/c^2

Table 3.2: *Properties of the Standard Model gauge bosons and the Higgs particle [72].*

3.2 Perturbative Quantum Chromodynamics

QCD, the theory of strong interaction, is a non-abelian gauge theory based on $SU(3)_{colour}$ subgroup of the Standard Model. The QCD Lagrangian $\mathcal{L}_{QCD}$ (eq. 3.9) defines the interaction of quarks, anti-quarks and of the colour-force mediating gauge bosons, the gluons. Quark fields are described by Dirac spinors $\psi_{\alpha,c,f}(x)$, $\bar{\psi}_{\alpha,c,f}(x)$ with the spinor indices α, the flavour indices $f = 1, \ldots, N_f$, and the colour indices $c = 1, \ldots, N_c$. The gluon fields emerge naturally from the requirement of invariance of the free quark Lagrangian

$$\mathcal{L} = \bar{\psi}_{\alpha,c,f}(i\slashed{\partial} - m)\psi_{\alpha,c,f} \tag{3.2}$$

under local $SU(3)_{colour}$ transformations . The spinors transform under the fundamental representation of $SU(3)$ given as

$$\psi'_{\alpha,c,f}(x) = U_{ji}(x)\psi_{\alpha,c,f}(x), \qquad \bar{\psi}'_{\alpha,c,f}(x) = \bar{\psi}_{\alpha,c,f}(x)U_{ji}^{\dagger}(x) \tag{3.3}$$

with the $SU(N)$ transformation defined as generalized rotation in colour space

$$U_{ji}(x) = \left\{ \exp\left\{ \left(i \sum_{a=1}^{N_c^2-1} \beta_a(x)t^a \right) \right\} \right\}_{ji} . \tag{3.4}$$

The $N_c^2 - 1$ ($N_c \times N_c$) matrices t^a together with the their commutator relation $[t_a, t_b] = i f_{abc}t_c$ are the generators of $su(3)$ lie algebra, where f_{abc} are the $su(3)$ structure constants.

These Generators are defined in terms of the eight Gell-Mann matrices $t_a = \lambda_a/2$. While the mass term in equation 3.2 is invariant under transformation 3.4, the derivative ∂_μ is not. To impose local gauge invariance the derivative is replaced by a covariant derivative, that compensates the symmetry breaking contribution. It is given as

$$D_{\mu,ij} \equiv \delta_{ij}\partial_\mu + ig_s \sum_{a=1}^{N_c^2-1} A_{\mu a}(x)(t_a)_{ij} = \delta_{ij}\partial_\mu + igA_\mu(x), \qquad (3.5)$$

where $A_\mu(x)$ are identified as the gluonic fields. The invariance principle fixes the field transformation behaviour to

$$A'_\mu(x) = U(x)A_\mu U^\dagger(x) + \frac{i}{g_s}\left[\partial_\mu U(x)\right]U^\dagger(x), \qquad (3.6)$$

They therefore transform under the adjoint representation of $SU(3)$. To complete the gauge-invariant QCD Lagrangian a kinematic gluon field term has to be introduced. It can be defined by the gluonic field strength tensor

$$F_{\mu\nu} = F_{\mu\nu,a}t_a \equiv \frac{i}{g_s}\left[D_\mu, D_\nu\right] = \partial_\mu A_\nu + \partial_\nu A_\mu - ig_s\left[A_\mu A_\nu\right]. \qquad (3.7)$$

Form the possible definitions of a kinetic term for the gauge fields only the trace over the product of $F_{\mu\nu}F^{\mu\nu}$ is gauge invariant. On finds

$$Tr(F_{\mu\nu}F^{\mu\nu}) = F\mu\nu, aF^{\mu\nu,b}Tr(t_a, t_b) \equiv T_R F_{\mu\nu a}F^{\mu\nu a} \qquad (3.8)$$

exploiting $Tr(t_a, t_b) = T_R\delta_{ab}$ with $T_R = 1/2$ in the fundamental representation of $SU(N)$. The QCD Lagrangian is then given as

$$
\begin{aligned}
\mathcal{L}_{QCD}^{\text{gauge-inv.}} =\quad & \sum_{f=1}^{N_f} \bar{\psi}_{\alpha,c,f}(x)(i\slashed{D}(A) - m_f)\psi_{\alpha,c,f}(x) - \tfrac{1}{4}F_{\mu\nu a}F^{\mu\nu a} \\
=\quad & -\tfrac{1}{4}(\delta_\mu A_\nu^a - \delta_\nu A_\mu^a)^2 + \sum_f \bar{\psi}_{\alpha,c,f}(x)(i\slashed{\partial}_\mu - m_f)\psi_{\alpha,c,f}(x) \\
+\quad & g_s f_{abc}(\partial_\mu A_\nu^a)A_\mu^b A_\nu^c - \tfrac{g_s^2}{4}f_{abc}f_{ade}A_\mu^b A_\nu^c A_\mu^d A_\nu^e \\
+\quad & \tfrac{ig_s}{2}A_\mu^a \sum_f \bar{\psi}_{\alpha,c,f}(x)\gamma^\mu(\lambda^a)_j^i\psi_{\alpha,c,f}(x)
\end{aligned} \qquad (3.9)
$$

The free kinematic terms for the gluons and the quark fields, the quark-gluon interaction as well as the gluon self interaction in form of the three-gluon and four gluon vertex can be read from equation 3.9. The gauge boson self-interaction is a distinctive feature of the non-abelian nature of QCD. The Feynman diagrams of the gauge-invariant QCD Lagrangian are shown in table 3.3 omitting the gluon propagator. In performing the quantization a suitable gauge-fixing has to be done to remove the impact of physically equivalent contributions. In the functional quantization approach this can be done following the method of Fadeev and Popov in [73].

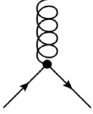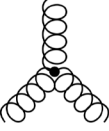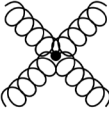$$\mathcal{L}_{QCD}^{eff} = \mathcal{L}_{QCD} + \mathcal{L}_{gauge} + \mathcal{L}_{ghost} \qquad (3.10)$$

	$$-i\frac{g_s}{2}\gamma^\mu\lambda^a_\mu$$
	$$g_s f_{abc}\Big[g_{\mu\nu}(k_1-k_2)_\lambda + g_{\nu\lambda}(k2-k_3)_\mu + g_{\lambda\mu}(k_3-k_1)_\nu\Big]$$
	$$-ig_s^2\Big[f_{abc}f_{cde}(g_{\mu\lambda}g_{\nu\rho}-g_{\mu\rho}g_{\nu\lambda})$$ $$+f_{ade}f_{bce}(g_{\mu\nu}g_{\lambda\rho}-g_{\mu\lambda}g_{\nu\rho})$$ $$+f_{ace}f_{bde}(g_{\mu\rho}g_{\nu\lambda}-g_{\mu\nu}g_{\rho\lambda})\Big]$$
	$$i\delta_{ij}\frac{\slashed{k}+m}{k^2-m^2+i\epsilon}$$

Table 3.3: *Feynman rules and contributions for the gauge-invariant QCD Lagrangian*

Typically choices for the gauge fixing term are the covariant gauge $\mathcal{L}_{gauge} = -\frac{1}{2\xi}\sum_{a=1}^{N_c^2-1}(\partial_\mu A_a^\mu)^2$ or the axial gauge $\mathcal{L}_{gauge} = -\frac{1}{2\xi}\sum_{a=1}^{N_c^2-1}(n\cdot A_a)^2$, where n is a fixed direction and the choice of n and ξ define the actual gauge. The simplest covariant gauge and often used choice is the so called Feynman-'t Hooft gauge ($\xi = 1$). In the covariant gauge $\mathcal{L}_{ghost}$ has to be added to ensure universality of the resulting S-matrix as it removes the unphysical polarization states of the gluons which would be contributing to measurable observables.

$$\mathcal{L}_{ghost} = (\partial_\mu\bar{c}_a)(\partial^\mu\delta_{ad} - gf_{abd}A_b^\mu)c_d, \tag{3.11}$$

with the scalar ghost fields $\bar{c}_a$ and c_a.

The gauge fixing allows to write down the gluon and ghost propagators and the additional ghost terms related interaction graphs in covariant gauge (Figure 3.4)
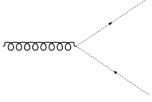
	$$\frac{i\delta_{ab}}{k^2 + i\epsilon}\left[g_{\mu\nu} - (1-\xi)\frac{k_\mu k_\nu}{k^2}\right]$$
	$$\frac{i\delta_{ab}}{k^2 + i\epsilon}$$
	$$g_s f_{abc} p_\mu$$

Table 3.4: *Feynman rules and contributions for the gauge-fixed QCD Lagrangian*

The key idea of the perturbative treatment of QCD is the expansion of a given observable f in powers of the coupling constant g_s. or more commonly in $\alpha_s = \frac{g_s}{4\pi}$

$$f = f_0 + f_1\alpha_s + f_2\alpha_s^2 + \cdots \tag{3.12}$$

under the assumption that the coupling is small. The detailed discussion of the functional quantization procedure at this point would go beyond the scope of this chapter and the interested reader is encouraged to review the topic in e.g. [71]. It shall be given that calculation of S matrix elements, that are the essential ingredients for the calculation of scattering amplitudes, is closely related to the evaluation of n-point correlation functions, the so-called Green functions. In the perturbative evaluation the problem is defined by the evaluation of a infinite sum of integrals, ordered by the power of the coupling constant, that can be diagrammatically expressed as Feynman graphs. These diagrams then have to be evaluated for each order in the coupling strength. The emergence of loop diagrams, that can be interpreted as vacuum corrections, with unbound intermediate momentum complicates the explicit calculation. These divergent contributions are called UV singularities. To evaluate these integrals are regulator has to be introduced that is then removed in a controlled way after the all integrals have been evaluated . There are different strategies of those the most commonly used method is the Dimensional Regularisation [74, 75]. In this scheme the space time dimension is chosen to be $d = 4 + 2\epsilon$ leading to constraint of the singularities in the form of $1/\epsilon^N$ with $N = 1, 2, \ldots$. The exact form of the redefinition of the dimensionality varies in the literature without impacting the results in the limit of $\epsilon \to 0$. One important idea in QFT is that the fields, masses and couplings in the theory are not observable quantities and can be redefined in such a way that the observables of the theory are finite. This procedure is called Renormalisation. A theory is called renormalisable if a finite set of

rescaling parameters exist to remove all UV singularities. Technically one introduces Renormalisation Constants Z, defined in each order of perturbation theory and counter terms to the Lagrangian to subtract the divergent contributions. There exists a certain ambiguity in definition of the singular part of the Green functions, that allow the definition of different so-called Renormalisation schemes. The Minimal Subtraction MS scheme defines the arising infinities by the $1/\epsilon$ term, while the often used $\overline{\text{MS}}$ scheme also includes the also constant contribution $\gamma_E + \ln 4\pi$.

The QCD Renormalisation constants Z_i can be written as:

$$
\begin{aligned}
\psi &= Z(\mu_R)_2^{1/2}\psi_r(\mu_R) \quad , \quad A = Z(\mu_R)_3^{1/2}A_r(\mu_R), \quad c = \tilde{Z}_3^{1/2}c_r(\mu_R)c(\mu_R), \\
m &= Z_m(\mu_R)m_r(\mu_R) \qquad\qquad\qquad \xi = \tilde{Z}(\mu_R)_3\xi_r(\mu_R) \\
g_s &= Z_g(\mu_R)g_s^r(\mu_R) \qquad\qquad\qquad\quad \Leftrightarrow \alpha_s = Z_\alpha \alpha_s^r
\end{aligned}
\tag{3.13}
$$

Z_2 , Z_3 and $\tilde{Z}_3$ are the quark, the gluon and the ghost field Renormalisation constants and Z_g and Z_m the respective constants for the coupling and the quark masses. With these definitions the QCD Lagrangian can be expressed as the sum of the previously defined (Eqn. 3.9) Lagrangian, the gauge fixing Lagrangian, the ghost Lagrangian and a new counter-terms:

$$
\begin{aligned}
\mathcal{L}_{ct} = \quad & (Z_2 - 1)\bar{\psi}_r^i i\gamma^\mu \partial_\mu \psi_r^i - (Z_2 Z_m - 1)m\bar{\psi}_r^i\psi_r^i \\
+ \quad & (Z_3 - 1)\tfrac{1}{2}A_r^{a\mu}\delta_{ab}(g_{\mu\nu}\Box - \partial_\mu\partial_\nu)A_r^{b\nu} \\
+ \quad & (\tilde{Z}_3 - 1)(\xi_r^a)^*\delta_{ab}\delta_{ab}(-\Box)\xi_r^b \\
+ \quad & (Z_g Z_2 Z_3^{\frac{1}{2}} - 1)\tfrac{g_s}{2}\bar{\psi}_r^i\lambda_{ij}^a\gamma^\mu\partial_\mu\psi^j A_{\mu r}^a \\
+ \quad & (Z_g Z_3^{\frac{3}{2}} - 1)\tfrac{g_s}{2}f_{abc}(\partial_\mu A_{\nu r}^a - \partial_\nu A_{\mu r}^a)A_r^{b\mu}A_r^{c\nu} \\
- \quad & (Z_g^2 Z_3^2 - 1)\tfrac{g_s^2}{4}f_{abc}f_{cde}A_{\mu r}^a A_{\mu r}^b A_r^{c\mu}A_r^{d\nu} \\
- \quad & (Z_g \tilde{Z}_3 Z_3^{\frac{1}{2}} - 1)g_s^r f_{abc}(\partial^\mu\xi_r^a)^*\xi_r^b A_{r\mu}^c.
\end{aligned}
\tag{3.14}
$$

The Renormalisation scale μ_R introduced in equation 3.13 is an artefact of the regularization procedure as e.g. in case of the dimensional regularization it has to be introduced to guarantee the usual mass dimensions of the matrix elements and observables. It is the momentum scale at which the UV singularities are subtracted. While the choice of μ_R is arbitrary, physical quantities as for example the elements of the S matrix should be independent of this scale. For a dimensionless observable that is probed at some given momentum scale Q^2 the requirement of the independence on the Renormalisation scale can be expressed as

$$
\mu_R^2 \frac{dR(Q^2,\mu_R^2,\alpha_s)}{d\mu_R^2} = \mu_R^2 \frac{\partial\alpha_s}{\partial\mu_R^2} + \mu_R^2\frac{\partial\alpha_s}{\mu_R^2}\frac{\partial R}{\partial\alpha_s} \overset{!}{=} 0
\tag{3.15}
$$

With $t = \ln Q^2/\mu^2$ and $\tilde{\beta}(\alpha_s) = g_s^r/4\pi\beta g_s^r = \mu_R^2 \frac{\partial\alpha_s}{\mu_R^2}$ it defines a so-called Renormalisation Group Equation (RGE).

$$-\frac{\partial R}{\partial t} + \tilde{\beta}(\alpha_s)\frac{\partial R}{\partial\alpha_s} = 0 \qquad (3.16)$$

It may be noted that the presented formula is a simplified version of the Callan-Symanzik equation, omitting the the scale dependence of the mass parameters m, deliberately chosen here to simplify the illustration. The full QCD beta function is currently known up to fourth order loop corrections [76]. Introducing the QCD scale parameter $\Lambda_{QCD} := \exp\left\{-\frac{2\pi}{(11-2/3N_f)\alpha_s\mu_R}\right\}$ one can derive the dependence of α_s on the scale Q from equation 3.16.

$$\alpha_s(Q^2) = \frac{12\pi}{(33 - 2n_f)\ln\left(Q^2/\lambda_{QCD}^2\right)} \qquad \lambda_{QCD} \qquad (3.17)$$

The scale parameter λ_{QCD}^2 is determined by experiments and cannot be derived a-priory. It defines the scale at that the perturbatively defined coupling is no longer valid and diverges. From equation 3.17 it can be seen that the coupling strength decreases with increasing momentum transfer. A simplified explanation can be given by the "Anti-screening" picture. A naked quark will create virtual quark-anti-quark pairs and gluons from the vacuum. The newly created quarks screen the original colour charge, the gluons however carrying two colour charges will not. At low momentum transfers the gluons will thus amplify the initial colour charge while at higher momentum transfers more and more of the original colour charge can be seen. The property that quarks behave as free particles in the limit of $Q^2 \to \infty$ ($\alpha_s \to 0$) is called asymptotic freedom [77, 78].

Figure 3.1 shows the scale dependence of α_s as predicted by QCD in comparison to experimental data from Deep Inelastic Scattering, electron-positron annihilation and from the the measurement of heavy quarkonia. The world average of α_s defined at the scale of the Z-boson mass M_Z was found to be $\alpha_s(M_Z^2) = 0.1184 \pm 0.0007$.

The scale parameter λ_{QCD} is found by comparison of the four-loop α_s calculation to the experimental data in the $\overline{\text{MS}}$ scheme with $n_f = 5$ to be ~ 213 MeV.

3.2.1 Factorization

The cross section of a generic $2 \to 2$ QCD process of two partons a and b within two incoming hadrons A and B into two hadrons h_c and h_d can be divided into a perturbatively calculable hard process and a non-perturbative part that includes the effects of partons within the hadron. This separation is based on the QCD factorization
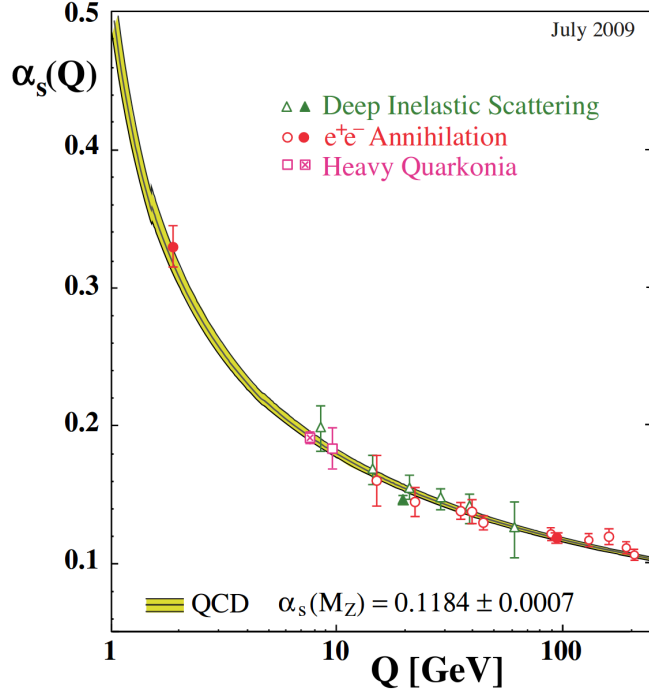
Figure 3.1: *Summary of measurements of α_s as a function of the respective energy scale Q [72].*

theorem (cf. e.g. [80]) and is leading to the following cross section definition:

$$
\begin{aligned}
\sigma(p_a, p_b, Q^2) = & \sum_{a,b} \int dx_a dx_b f_{a/A}(x_a, \mu_F^2) f_{b/B}(x_b, \mu_F^2) \\
\times & \quad \hat{\sigma}_{ab \to q\bar{q}}^H(x_a p_a, x_b p_b; \alpha_s; Q^2; \mu_F^2; \mu_R^2) \\
\times & \quad\quad D_{h_c}(z_{h_c}, Q^2) D_{h_d}(z_{h_d}, Q^2)
\end{aligned}
\tag{3.18}
$$

Where

μ_R	is the Renormalisation scale,
μ_F	is the factorization scale,
Q	is the scale of the hard scattering,
$f_{a/A, b/B}(x_{a,b}, \mu_F^2)$	is the parton distribution function defined at μ_F,
x_k	is the momentum fraction of hadron k carried
	by the parton i or j ,
$\tilde{\sigma}_{a,b}$	is the short-distance scattering cross section for
	partons i and j and
$D_h(z, Q^2)$	is the fragmentation function,

The theorem states that the hadronic cross section of a process with the hadronic final state H is given as a weighted coherent sum of single parton interactions. Where the weighting factor is given by the parton distribution functions (PDF) $f_i(x_{i/H}, \mu_F^2)$
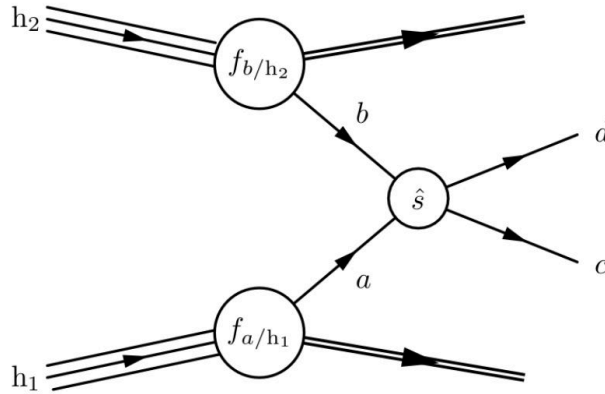
Figure 3.2: *Schematic structure of a hadron-hadron interaction [79].*

that represent the probability to find a parton i in the initial hadron H that carries the longitudinal momentum fraction x_i of the respective hadron. The factorization scale defines the energy scale that separates short-distance and long-distance physics. Partons with momenta below the factorization scale are considered part of the hadron and their description is absorbed into the PDF. The momenta p_a^μ and p_b^μ are the four momenta of the incoming partons a and b that can be related to the momenta of the incoming protons p_A and p_B by their respective momentum fractions as $p_{a(b)} = x_{a(b)}p_{A(B)}$. $\hat{\sigma}_{a,b}$ is the perturbatively calculable short-distance cross section of the interaction of the partons a and b and can be calculated up to a fixed order in α_s at the given Renormalisation scale with a standard ansatz for the $(n+k)$th approximation

$$\hat{\sigma_{a,b}} = \alpha_s^k \sum_{m=0}^{n} w^{(m)} \alpha_s^m \tag{3.19}$$

where the coefficients w are functions of the kinematic variables and the factorization scale. The accessible Bjorken-x range for the beauty quark production at the LHC can be calculated by expressing x as a function of the invariant $Q\bar{Q}$ mass ($M_b \approx 4.8$ GeV/c) of the quark pair system and the pair rapidity y.

$$x = \frac{m_{Q\bar{Q}}}{\sqrt{s}\exp(\pm y)} \tag{3.20}$$

At $\sqrt{s} = 7$ TeV it ranges from $x \approx 10^{-3}$ at $y = 0$ and $x \approx 10^{-5}$ at $y = 4$.

3.2.2 Parton distribution functions

Contrary to the naive parton model picture the proton consists not only of its three valence quarks, but due to the constant emission and absorption of gluons it is full of short lived virtual quark-antiquark pairs, the so-called sea quarks. The instantaneous

proton momentum is therefore given by the sum of all these constituents. While the the exact momentum distribution may vary, the PDF is the time-averaged probability for each of these constituents to carry the momentum fraction x of the proton. The PDF also absorbs collinear divergences caused by gluons radiated of the quarks. While there are several PDF parametrization and fitting techniques as Martin-Stirling-Thorne-Watt PDFs (MSTW) [81], the artificial neural network based NNPDF [82] and the PDF set obtained by the multi-institutional Coordinated Theoretical-Experimental Project on QCD group (CTEQ), that is mainly used in this thesis. The generic ansatz of the CTEQ version 6.6m parametrizations at the reference energy scale $Q_0 = 1.3$ GeV is given by

$$ xf(x, Q_0) = \alpha_0 x^{\alpha_1}(1-x)^{\alpha_2} e^{\alpha_3\ x}(1+e^{\alpha_4}x)^{\alpha_5} \tag{3.21} $$

with the fit parameters α.
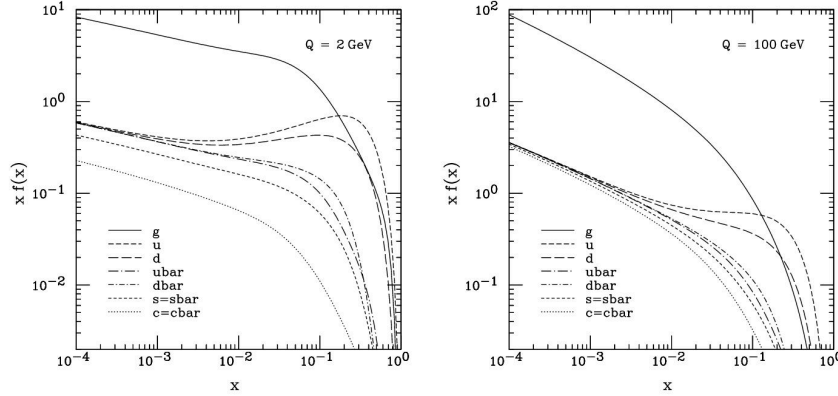
Figure 3.3: CTEQ*6.6M parton distribution functions at Q = 2 and 100 GeV [83]*

Figure 3.3 shows the respective CTEQ6.6m PDF at $Q = 2$ GeV/c and $Q = 100$ GeV/c. Figure 3.4 is an example of the momentum fraction distributions for the MSTW2008 [81] PDF at two different momentum scales. As one would expect the dominant contribution at low x is given by gluons and the valence u-quarks and it is about twice the probability of d-quarks at large x values. The x dependence has to be constrained via experimental data, while the dependence of the momentum scale Q is calculable using the Dokshitzer–Gribov–Lipatov–Altarelli–Parisi (DGLAP) [84][85] [86] equations.
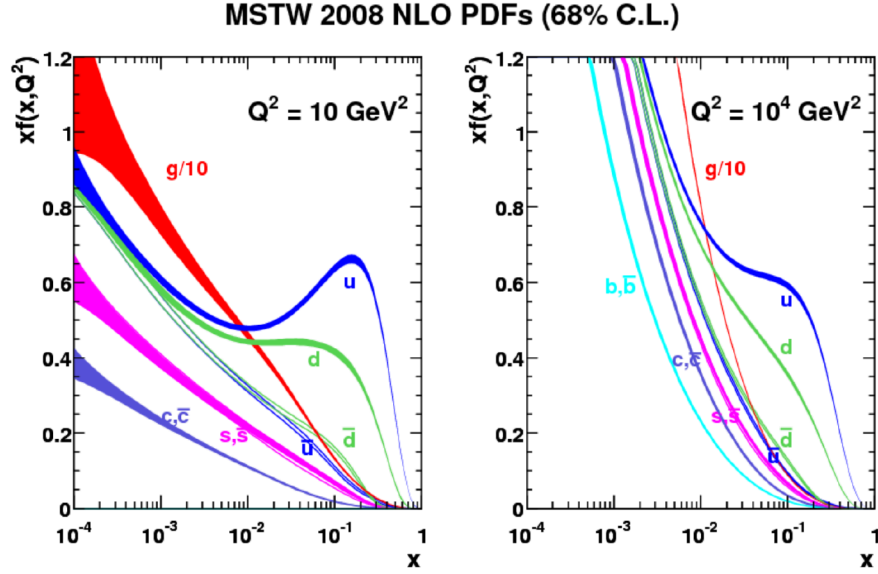
Figure 3.4: *From [81]: MSTW 2008 NLO PDFs at $Q^2 = 10$ GeV^2 and $Q^2 = 10^4$ GeV^2.*

The dependence of PDFs on the momentum scale Q is described by the DGLAP equations. It is derived from the requirement that $\sigma(p_a, p_b, Q^2)$ should be independent from the factorization scale and the fact that the parton densities are only independent from μ_F in leading-order α_s. The DGLAP equations are given by

$$\frac{df_i(x_{i/H}, Q^2)}{dlog(Q^2)} = \frac{\alpha_s}{2\pi} \int_x^1 \frac{dz}{z} (f_i(z, Q^2) P_{qq}(\frac{x}{z}) + g(z, Q^2) P_{qg}(\frac{x}{z})) \qquad (3.22)$$

$$\frac{dg(x, Q^2)}{dlog(Q^2)} = \frac{\alpha_s}{2\pi} \int_x^1 \frac{dz}{z} (\sum_i f_i(z, Q^2) P_{gq}(\frac{x}{z}) + g(z, Q^2) P_{gg}(\frac{x}{z})). \qquad (3.23)$$

Equations 3.22 and 3.23 describe the change of the quark densities as a function of Q^2 due to gluon splitting and gluon radiation and the change in the gluon density due to gluon radiation. The splitting functions P_{xy} describe the probability of gluon radiation or splitting to occur.
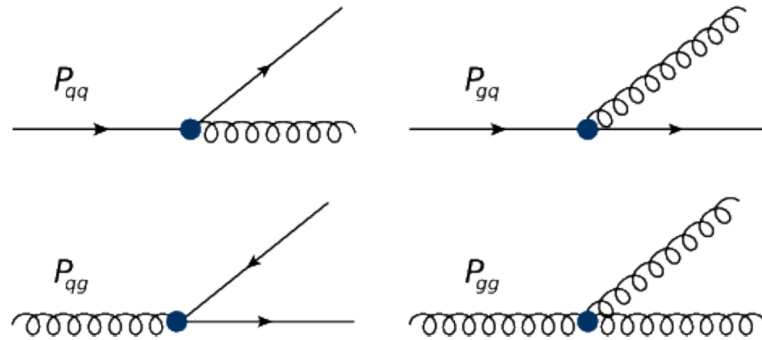
Figure 3.5: *Schematic representation of the lowest-order QCD splitting functions. [87]*

PDFs are constrained over a wide range of x and Q^2 by different suitable channels, most notably Deep Inelastic scattering (DIS), Drell-Yan(DY) and jet production. Low x DIS data from HERA [88][89] and fixed target DIS and DY data [90] for higher x values. The gluon distribution can be constrained via the jet measurements from colliders [91].

3.2.3   Fragmentation functions

A fragmentation functions (FF) describes the probability of a parton X to produce a hadron Y and the momentum fraction z at the momentum scale Q^2. Fragmentation functions are quite specific to the initial parton flavour and the final state hadron. For heavy flavour quarks the fragmentation is expected to be much harder as the heavy meson carries most of the heavy quark momentum. In this respect there are several fragmentation function candidates some of those are listed in table 3.5.

Parametrization	Function
Peterson [92]	$D_h(z) = \frac{N}{z}\left[1 - \frac{1}{z} - \frac{\epsilon}{1-z}\right]^{-2}$
Kartvelishvili [93]	$D_h(z) = N z^\alpha (1 - z)$
Lund [94]	$D_h(z) = N \frac{(1-z)^\alpha}{z} \exp\left(\frac{-b m_\perp^2}{z}\right)$

Table 3.5: *Common heavy quark fragmentation function parametrizations*

The free ϵ parameter of the Peterson FF is fitted to data obtained by the ALEPH collaboration [95]. In leading-logarithmic approximation for the perturbative part one finds [72] $\epsilon \approx 0.006$ and $\epsilon \approx 0.0033$ in a second order calculation or $\epsilon \approx 0.0023$ in a fixed order α_s^2 calculation.

3.3 Beauty production in pp collisions

3.3.1 Fixed Flavour-Number scheme

Methods for the perturbative treatment of Heavy Quark production are around since the late eighties [96, 97, 98, 99, 100, 101, 98, 102, 103, 104]. These early calculations treat heavy quarks as massive particles at all scales, while they are not treated as constituents the incoming protons. The number of active flavours in the proton PDFs are therefore fixed to $n_f = 4$ in the case of beauty quarks or $n_f = 3$ in the case of a charm quarks. Therefore the method is also named "Fixed Flavour Number Scheme" (FFNS). Within this description heavy Quarks can only be produced in the hard process .
The p_T-integrated heavy quark cross section can therefore be derived starting from the factorization theorem. Omitting the fragmentation functions D_h equation 3.18 can be re-written to

$$\sigma(S_h) = \sum_{a,b} \int dx_1 dx_2 \hat{\sigma}_{ab}(x_1 x_2 S_h, m_Q^2, \mu^2) f_{a/A}(x_1, \mu) f_{b/B}(x_2, \mu). \qquad (3.24)$$

Following the procedure as depicted in [96], the scales in eq. 3.24 have been chosen as $\mu = \mu_R = \mu_F$ and the now significant mass m_Q was introduced as parameter of the partonic short-distance scattering cross section $\hat{\sigma}_{a,b}$. S_h is the square of the hadronic center-of-mass energy while s, as used in the following, denotes the the same quantity for the partonic system. $\hat{\sigma}_{a,b}$ can be written using the ansatz given in eq. 3.25.

$$\hat{\sigma_{a,b}}(s, m_Q^2, \mu^2) = \frac{\alpha_s^2(\mu^2)}{m_Q^2} f_{a,b}\left(\frac{4m_Q}{s}; \frac{\mu^2}{m^2}\right) \qquad (3.25)$$

The calculation of the total cross section is therefore defined by problem of identifying the functions $f_{a,b}$ for the different types of annihilating partons a and b. The processes that are to be considered at leading-order are quark anti-quark annihilation $q\bar{q} \longrightarrow Q\bar{Q}$ and gluon-gluon fusion $gg \longrightarrow Q\bar{Q}$. Order α_s^3 processes with a gluon fragmenting into have contributions are comparable in magnitude to the two α_s^2 processes ,therefore the leading-order (LO) calculation needs to be extended to α_s^3. It should be noted that the resulting cross section is thus only a extended leading-order calculation. Table 3.6 summarizes the considered contributions and figures 3.6 and 3.7 show a selection of the corresponding Feynman graphs.

Process		$\mathbf{O}(\alpha_s)$
$q + \bar{q} \to$	$Q + \bar{Q}$	$\alpha_s^2(\mu^2)\ \alpha_s^3(\mu^2)$
$g + g \to$	$Q + \bar{Q}$	$\alpha_s^2(\mu^2)\ \alpha_s^3(\mu^2)$
$q + \bar{q} \to$	$Q + \bar{Q} + \text{g}$	$\alpha_s^3(\mu^2)$
$g + g \to$	$Q + \bar{Q} + \text{g}$	$\alpha_s^3(\mu^2)$
$g + q \to$	$Q + \bar{Q} + \text{g}$	$\alpha_s^3(\mu^2)$
$g + \bar{q} \to$	$Q + \bar{Q} + \text{g}$	$\alpha_s^3(\mu^2)$

Table 3.6: *Contributions to perturbative heavy quark hadro-production up to order* $\alpha_s^3(\mu^2)$ *[96]*

(a)   (b)   (c)   (d)
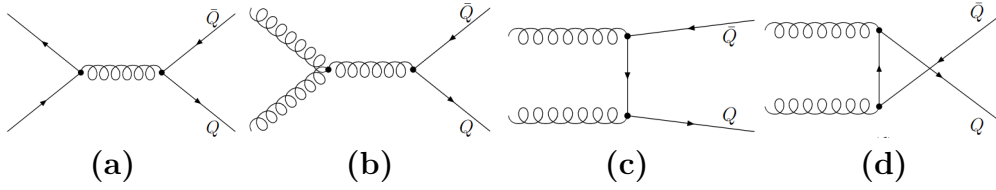
Figure 3.6: *Leading-order contributions to b-quark production []*
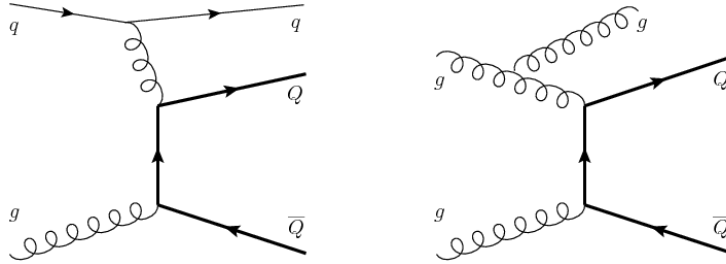
Figure 3.7: *Some exemplary Next-to-leading order contributions to the b-quark hadro-production[105].*

Expanding $f_{a,b}$ in $\alpha_s = \frac{g_s^2}{4\pi}$ yields

$$f_{a,b}(\frac{4m_Q}{s}, \frac{\mu^2}{m_Q^2}) = f_{a,b}^{(0)}(\frac{4m_Q}{s}) + g_s^2(\mu^2)\left[f^{(1)}_{ab}(\frac{4m_Q}{s}) + \bar{f}^{(1)}_{ab}(\frac{4m_Q}{s}) \ln \frac{\mu^2}{m_Q^2} \right] \quad (3.26)$$

Extending the leading order approximation for the running of α_s (see eq. 3.17) one obtains

$$\frac{d\alpha_s(\mu^2)}{d\ln \mu^2} = -\frac{33 - 2n_f}{12\pi}\alpha_s^2 - \frac{(153 - 19n_f)}{24\pi^2}\alpha_s^3 \quad (3.27)$$

The arising mass singularities are renormalized and factorized, there the Renormalisation is performed in an extension to the $\overline{\text{MS}}$-scheme. Light quark loop contributions are treated in the $\overline{\text{MS}}$ scheme. Nason et. al. [96] then introduce Renormalisation conditions for the heavy quark two-point Green function are chosen such that the heavy quark propagator has a pole at m_Q and fix the *g-q-q* vertex, to cover all graphs with a heavy quark on a external line and subtract heavy quark loops at zero momentum.

Table 3.7 gives the resulting $f^{(0)}$ contributions, where $\rho := \frac{4m_Q}{s}$ was substituted, with $\beta = \sqrt{1-\rho}$.

Process	Contribution
$q,\bar{q}$	$\frac{\pi\beta\rho}{27}\left[2+\rho\right]$
g,g	$\frac{\pi\beta\rho}{192}\left[\frac{1}{\beta}(\rho^2+16\rho+16)ln\left(\frac{1+\beta}{1-\beta}\right)-28-31\rho\right]$
$g,q/\bar{q}$	0

Table 3.7: $f_{ij}^{(0)}$ *contributions*

Renormalisation group arguments allow to express $\bar{f}^{(1)}$ as function of $f^{(0)}$ by the implicit constraints introduced via the scale dependence. Here the lowest order running α_s in conjunction with the lowest-order DGLAP equation was used under the principle that the physical result has to be independent of the choice the Renormalisation group scale. The resulting contributions are listed in table 3.8.

where the helper function

$$h_1(\beta) = \ln\left(\frac{1+\beta}{2}\right)^2 - \ln^2\left(\frac{1-\beta}{2}\right) + 2Li_2\left(\frac{1-\beta}{2}\right) \tag{3.28}$$

$$h_2(\beta) = Li_2\left(\frac{2\beta}{1+\beta}\right) - Li_2\left(\frac{-2\beta}{1-\beta}\right) \tag{3.29}$$

$$Li_2(x) = -\int_0^z \frac{dz}{z} ln(1-z) \tag{3.30}$$

were introduced.

Process	Contribution
$q,\bar{q}$	$\frac{1}{8\pi^2}\left[\frac{16\pi}{81}\rho ln\left(\left(\frac{1+\beta}{1-\beta}\right)+\frac{1}{9}f_{q\bar{q}}^{(0)}(\rho)(127-6n_{LF}+48\ln\left(\frac{\rho}{4\beta^2}\right)\right)\right]$
$g\,g$	$\frac{1}{8\pi^2}\left[\frac{\pi}{192}\left\{2\rho(59\rho^2+198\rho-288)\ln\left(\frac{1+\beta}{1-\beta}\right)+12\rho(\rho^2+16\rho+16)h_2(\beta)\right.\right.$
	$\left.\left.-6\rho(\rho^2-16\rho+32)h_1(\beta)-\frac{4}{15}\beta(7449\rho^2-3328\rho+724)\right\}+12f_{gg}^{(0)}(\rho)\ln\left(\frac{\rho}{4\beta^2}\right)\right]$
$g,q/\bar{q}$	$\frac{1}{8\pi^2}\frac{\pi}{192}\left[\frac{4}{9}\rho(14\rho^2+27\rho-136)\ln\left(\frac{1+\beta}{1-\beta}\right)\frac{32}{3}\rho(2-\rho)h_1(\beta)-\frac{8}{135}\beta(1319\rho^2-3468\rho+724)\right]$

Table 3.8: $\bar{f}_{ij}^{(1)}$ *contributions*

Lastly $f^{(1)}$ was originally obtained numerically as no true third order calculation was available and then fitted via a physics motivated model.
Radiative and virtual corrections were later included into the presented scheme [102] and also the p_T-double differential one particle cross sections were calculated.

3.3.2 ZM-VFNS, GM-VFNS and FONLL

Beside the FFNS approach there is another theoretical concepts to describe the hadronic heavy flavour final state based on the Parton Model picture. In this picture heavy quarks

are treated massless in the perturbative short-distance cross section, but rely on accurate scale-dependent fragmentation functions of quarks and gluons into the respective heavy-flavour hadron state. Due to the massless treatment of heavy quarks the method is also called Zero Mass Variable Flavour Number Scheme (ZM-VFNS) The required full mass-less calculation up to order α_s^3 is available since the eighties [106]. To obtain the required HF FF two approaches can be used. The first approach factorizes the FF into a perturbative short distance part and a non-perturbative part that expresses the hadronization of the heavy quark in a scale-independent way.

$$D_i^h(z, \mu_F) = D_i^Q(z, \mu_F) \otimes D_Q^H(z) \tag{3.31}$$

The second non-perturbative term is then fixed via $e^+ - e^-$-data, see eg. [107]. The other approach assumes non-perturbative boundary conditions and directly determines the full FF from experimental data.

Collins et. al. [108] introduced a combination of the FFNS and ZM-VFNS approach namely the General Mass Variable Flavour Number Scheme (GM-VFNS). This new approach is equivalent to ZM-VFNS in the limit of $p_T \gg m_Q$ by construction and to FFNS for $p_T = m_Q$ and provides a smooth interpolation between the low scale of the massive calculation(FFNS) and the scale of the massless calculation (ZM-VFNS). Conventional PDFs and FF are defined using the $\overline{\text{MS}}$ scheme thus different singularities arise in the massive and mass-less description, that need to be reformulated in a common scheme. The GM-VFNS therefore applies a matching scheme to interpolate between both descriptions. The difference of the massive partonic short-distance cross section in the limit of $m_Q \to 0$ and the default $\overline{\text{MS}}$ cross section is calculated and then subtracted. The resulting cross section can then be used with the default mass-less PDFs and FFs. Collinear logarithms of the form $\ln \mu^2/m_Q$ are absorbed into the PDFs and FFs and the resummed using DGLAP evolution, where μ is evolved to $\mu = p_T$ Figure 3.8 shows the predictions obtained in FFNS, ZM-VFNS and GM-VFNS calculations in comparison to CDF data.
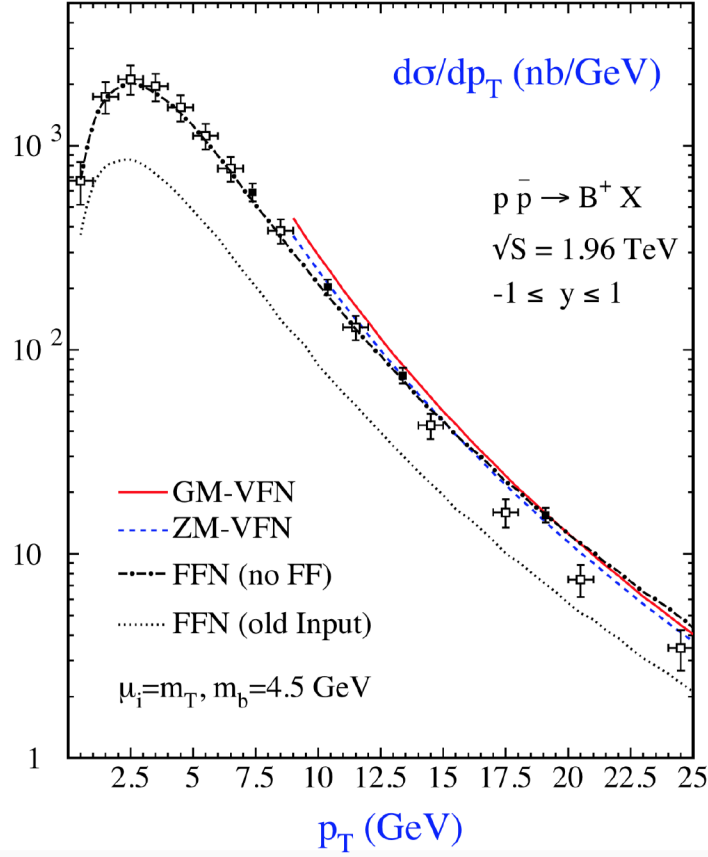
Figure 3.8: *Comparison of different model predictions for the transverse momentum distribution of $p\bar{p} \to B + X$ with CDF data points. The FFNS predictions at $n_f = 4$ are not applying any FF while older prediction uses a Peterson FF parametrisation. For more details see [105].*

For a detailed discussion of the NLO predictions see [100, 101, 98, 102, 103, 104]. The FONLL approach matches massive fixed next-to-leading order pQCD calculations (FO) with fully resummed next-to-leading logarithm corrections of the form $\alpha_s^n \log^n p_{\mathrm{T/m}}$ and $\alpha_s^n \log^{n-1} p_{\mathrm{T/m}}$ obtained from a massless calculation (RS). The FONLL key formula can be written as:

$$d\sigma_Q^{\mathrm{FONLL}} = d\sigma^{\mathrm{FO}} + (d\sigma^{\mathrm{RS}} - d\sigma^{\mathrm{F0M0}}) \times G(m, p_{\mathrm{T}}) \qquad (3.32)$$

Here FOM0 is the subtracted overlap of the FO and the RS parts in the same massless parametrization as the RS calculation. The matching function $G(m, p_{\mathrm{T}}) := p_{\mathrm{T}}^2/(p_{\mathrm{T}}^2 + \alpha^2 m^2)$ is chosen in the large transverse momentum $p_{\mathrm{T}} \gg m$ $G(m, p_{\mathrm{T}}) \to 1$. In case of heavy hadrons as D or B mesons the resulting FONLL cross section is convoluted by the respective non-perturbative fragmentation function (see section 3.2.3).

$$d\sigma_{HQ}^{\mathrm{FONLL}} = d\sigma_Q^{\mathrm{FONLL}} \otimes D_{Q \to H}^{NP} \qquad (3.33)$$

The full re-summation of the logarithmic corrections, that become significant below the HQ mass scale FONLL is expected to provide better predictions in the low momentum regime compared to GM-VFNS. Due to the nature of the calculation FONLL is limited to the description of inclusive Heavy Quark production. Figure 3.9a shows the comparison of different theoretic descriptions including FONLL and ALICE data [109] for D^+, D^0 and D^{*+} . Figure 3.9b shows the FONLL comparison of the B^+ cross section measured by ATLAS [110].
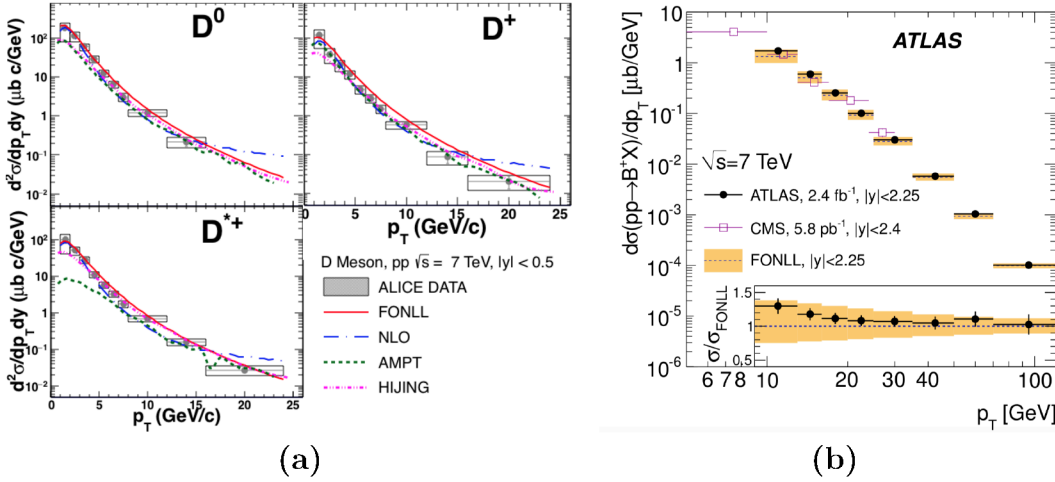
Figure 3.9: *Theory predictions and measurements of D^0, D^+, D^*+ (left) [109] and B^+ (right) [110]*

3.4   Monte Carlo event generators

Monte Carlo event generators are essential tools in High Energy Physics (HEP) for both theorist as for experimentalists and allow to make measurement predictions and to propose new observables or analysis channels that may even exceed the current definition of the Standard Model.

3.4.1   PYTHIA

PYTHIA is a widely used general purpose event generator. It is based on leading-order pQCD matrix elements convoluted with the a suitable proton PDF. In this analysis it is used with the Perugia 11 tune [111] for the underlying event generation. The event generation is combined with a parton shower leading-logarithmic QCD radiation model, a hadronization model based on the Lund string fragmentation model and a suitable multiple interaction description on. The longitudinal fragmentation is described by the

symmetric Lund fragmentation function (see 3.2.3) for light, charm and beauty quarks. The leading-order matrix elements only allow to model $2 \to 2$ processes, while $2 \to 3$ and $2 \to 4$ processes are implemented via the parton shower, that is also used for the description of the final-(FSR) and initial-state radiation(ISR). The

The PYTHIA simulation can be described in three stages:

1. process selection

2. generation of the initial state showers and beam fragments

3. generation of the final state showers, fragmentation (Lund model) and decays.
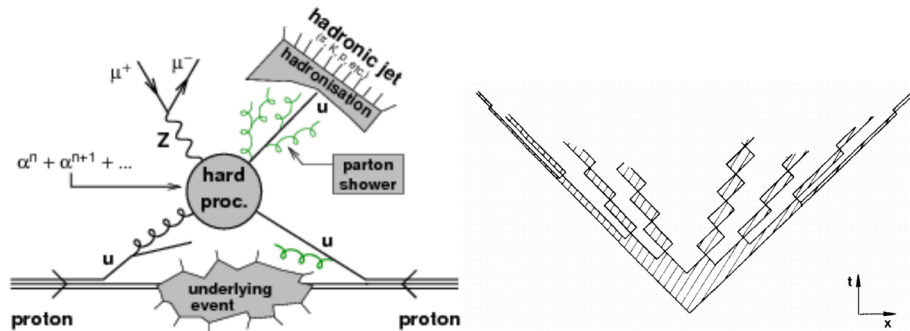
Figure 3.10: *Schematic representation of a proton-proton collision, involving a quark-gluon scattering that leads to a final state consisting of a Z-boson and a hard jet[112](left). Conceptual representation of the break-up in space–time of a Lund string into n hadrons [94] (right).*

Starting from the hard process that may also be provided by an external NLO generator initial- and final-state corrections are added via the parton shower algorithm. In PYTHIA6 (c.f. [113]) the final state showers are generated using either the virtuality- or a p_T-ordering scheme. A shower that can be interpreted as a series of $1 \to 2$ splitting processes as e.g. $q \to qg$ or $g \to gg$. In contrast to analytical calculations of the same order, that effectively implement energy- and momentum conservation as next-to-leading log corrections. The numerical implementations includes higher order-corrections indirectly via the inclusion of coherence effects, the choice of α_s and also enforces energy- and momentum-conservation on a per-splitting level. The splitting probabilities are again given by the QCD splitting functions discussed earlier completed by the non-hadronic splitting functions $P_{q \to q\gamma}$, $P_{l \to l\gamma}$. The probability of a parton A to branch into partons B and C where B carries the longitudinal momentum fraction z of A can be written as:

$$dP_a = \sum_{B,C} \frac{\alpha_{s/em}}{2\pi} P_{A \to BC}(z) dt dz \qquad (3.34)$$

where t acts as time-ordering variable for the shower evolution. The probability that a parton does not split between the ordering parameter values t_1 and t_2 is also called the Sudakov factor (SF) $S(t_1, t_2)$[114]. For a final state shower the evolution starts from a initial t_{max} that is set by the hard interaction. The parameter t can e.g. be identified with Q^2 (p_{T}) . Hence a final-state shower starts from $Q^2_{max} = Q^2_{hard}$ and the Sudakov factors $S(Q_{max}, Q_1)$for all particles are calculated and Q^2_1 is found by calculating a random number n and find the value of Q_1 where $S = n$, where Q_1 defines the mass m $(m^2 = E^2 + \mathbf{p}^2 \geq 0)$of the new particle. The corresponding z is equivalently found from the splitting functions in S. The process is repeated for each daughter until Q reaches a lower cut-off value that is of the order of 1 GeV. While PHYTIA6 originally used the virtuality ordering scheme it moved to the p_{T}-ordering scheme in the later versions due to its better compatibility with the updated multiple-interaction model. For that reason the p_{T}-ordering scheme is also the PHYTIA8 default.

The final state shower is followed by the Lund hadronization model. The string model is conceptionally based on the QCD prediction of approximate linear confinement of Quarks at large spatial distances. In a system of two a separating quark anti-quark pair a so-called colour flux tube is stretched out between both partons, where the force along the tube is assumed to be constant with a string tension of $\kappa = 1$ GeV/fm. In this picture gluons are considered as kinks in the string connecting the quark pair, carrying energy and momentum. As soft gluons and collinear gluons do not much impact the string evolution the process is by construction stable with respect to infrared safety.

A new quark-anti-quark pair is created if the energy stored in the string is larger than the required pair production energy. This happens by splitting the string into two new strings for that the fragmentation process continues. The symmetric Lund fragmentation function is constructed by a factor constituting the tunnelling probability for the quark pair out of the colour field of the string and a factor that determines the longitudinal momentum fraction of the hadron z. The tunnelling probability is given by $\frac{bm^2_{\mathrm{T}}}{z}$ where m_{T} is the transverse mass of the quark. The momentum fraction of the hadron is defined by $\frac{(1-z)^a}{z}$ where a as b are free parameters that can be tuned. The initial-state radiation is then added using a backward Sudakov factor based evolution starting at Q^2_{max} down to a lower cut-off Q^2_0 where the evolved PDF are used that contain the inclusive effects of ISR. Q^2_0 is needed to regulate soft and collinear divergences.

The exact values of e.g. α_s or the cut-off scales used in the simulation process are constrained via fits to measured data. The resulting parameter sets are standardized for comparability and called tunes. Of the many available tunes in Thesis the Perugia11 tune is in for all presented PYTHIA6 simulations, while the Monash 2013 tune [115] is used for the presented POWHEG/PYTHIA8 simulation.

3.4.2 POWHEG box

The acronym POWHEG stands for "Positive Weight Hardest Emission Generator". POWHEG (box) is a NLO Monte Carlo event generator combined with a parton shower implementation that allows to calculate infrared-safe observables with next-to leading order accuracy while collinear emissions are resummed at leading-logarithmic level. In contrast to older implementations in MC NLO that combined NLOcalculations with the HERWIG[116] parton shower, POWHEG only generates positive correction factors. POWHEG is based on a massive NLO calculation in the sense that Heavy Quarks are no active particles in the PDF they can however be created by the initial-state parton shower. The matching is performed using a five-flavour strong coupling constant and two correction factors, $-\alpha_s \frac{2T_F}{3\pi} \log \frac{\mu^2}{\mu_f^2} \sigma_{gg}^{(0)}$ and $-\alpha_s \frac{2T_F}{3\pi} \log \frac{\mu^2}{m^2} \sigma_{q\bar{q}}^{(0)}$ that are added to the gg and $q\bar{q}$ channels. In contrast to FONLL only a subset of the logarithmic corrections are resummed due to the complexity of the colour flow, leading to a leading-logarithmic light parton Sudakov factor.

This shortcoming is virtually compensated in the small transverse momentum region by NLO plus parton shower description of the exclusive final state. For the comparison of the final b-jet spectrum about 100 million POWHEG beauty events were generated for this using POWHEG box V1 and PYTHIA 8.185 [117] with five additional scale $\mu_R = \mu_F = \mu$ variations (variation factors for μ_R/μ_F: $.5/0.5, 0.5/1., 1./0.5, 2./1., 1./2.$) for the error assessment. PDF uncertainties of CTEQ6.6 provided by LHAPDF 5.9.1 [118][119] were not included in the shown prediction.

Figure 3.11 shows the comparison of the dijet production of full b-jets measured by ATLAS with MCNLO, POWHEG and PYTHIA.
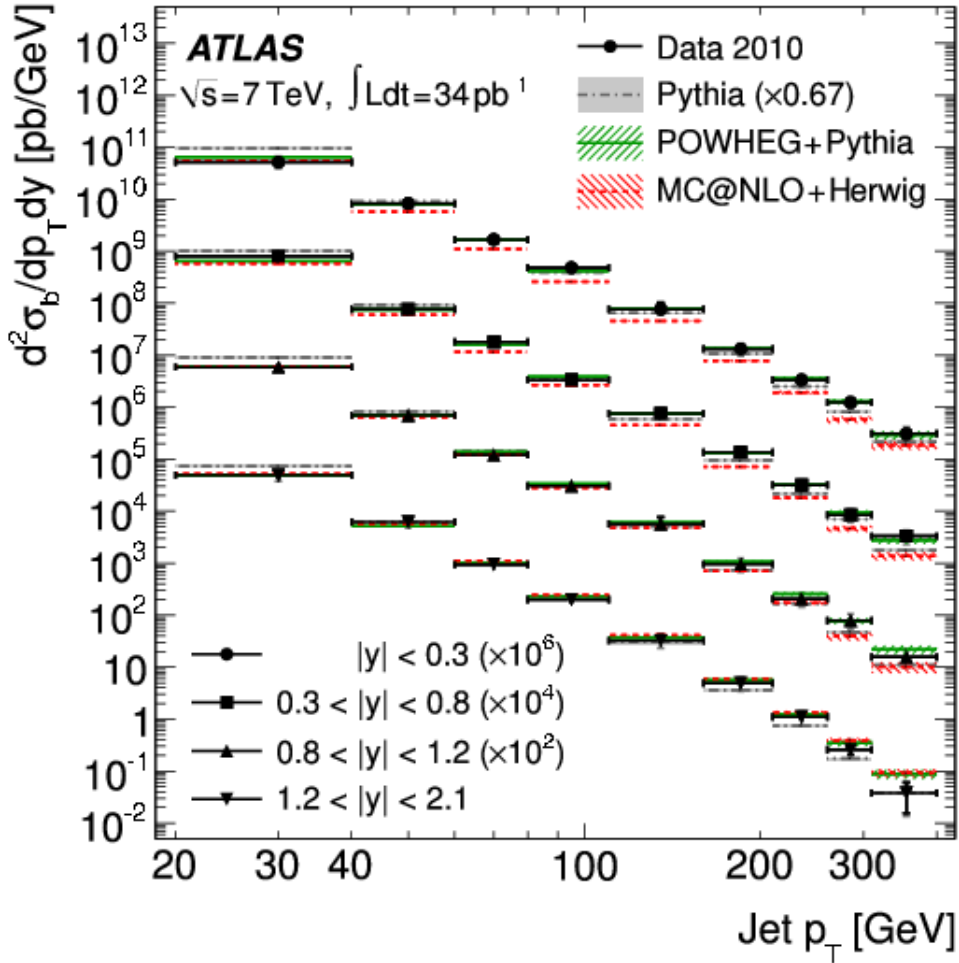
Figure 3.11: *Inclusive double-differential b-jet cross-section as a function of p_T for the different rapidity ranges. The data are compared to the predictions of* PYTHIA, POWHEG *and* MC NLO. *The leading-order prediction is scaled ($\times 0.67$) to the measured integrated cross-section* [120].

3.5 The generalized k_T-algorithm
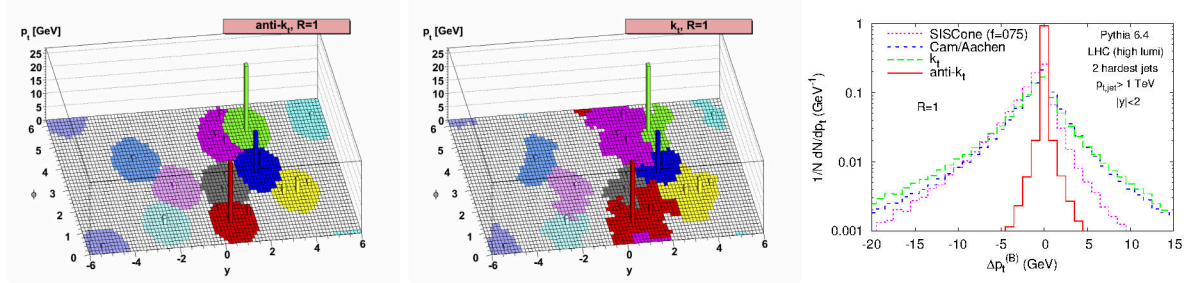
Figure 3.12: *Sample parton-level event clustered with the anti-k_T algorithm (left) and the k_T algorithm (centre) [121]. Distribution of back-reaction for the anti-k_T algorithm as compared to k_T algorithm, Cambridge/Aachen and SISCone [121] (right).*

The anti-k_T jet reconstruction algorithm [121] is a sequential object (particle, track) combination scheme based on their relative distance measure d_{ij} and their respective distances to the beam d_{iB}. The measures are defined as

$$d_{ij} = \min(p_{ti}^{2a}, p_{ti}^{2a}) \frac{\Delta_{ij}^2}{R^2} \text{ with: } \Delta_{ij} = \sqrt{(\eta_i - \eta_j)^2 + (\phi_i - \phi_j)^2} \qquad (3.35)$$

and

$$d_{iB} = p_{ti}^{2a} \qquad (3.36)$$

The parameter R is called the associated resolution parameter or radius. The parameter a effectively defines the different algorithms ($a = 1 \to k_T$ algorithm , $a = -1 \to$ anti-k_T algorithm). The actual jet reconstruction is achieved by iteratively calculating the distance measure of all available objects. For each set of distance measures the minimum of d_{ij} and d_{iB} is identified. If $d_{ij} < d_{iB}$ particles i and j are combined using a selected recombinations scheme to a new object with direction and momentum, while the original objects i and j are removed from the list of objects. If d_{iB} is the smaller quantity, object i is tagged as a jet and is removed from the list of objects. For $a = 1$ it is obvious that the effective distance for a low momentum particle is small and their initial clustering is favoured. While this description leads to irregularly shaped jet objects it provides a ideal method to sample the underlying event. For $a = -1$ the clustering starts with the leading momentum particles, suppressing the contribution from the soft-background.

The simplest recombination scheme and the one that is used within the analysis presented in this thesis is the so called E-scheme. In this scheme the components of four momenta of the two objects are added to generate the new object. It may be noted that there are several other approaches that involve a partial preprocessing step in order to make the initial momenta massless. The area of a given jet can be calculated by gen-

erating randomly distributed zero-momentum objects within full detector acceptance. These ghost particles do not impact the final jets in any way. The area can then be deduced by the number of ghost particles with a given jet while the precision is bound to the density of ghost particles and therefore only limited by the maximum computational complexity.

Chapter 4

Statistical reconstruction of charged beauty jets in proton-proton collisions at $\sqrt{s} = 7$ TeV

> *The important thing is not to stop questioning.*
> *Curiosity has its own reason for existence. One cannot*
> *help but be in awe when he contemplates the mysteries*
> *of eternity, of life, of the marvellous structure of reality.*
> *It is enough if one tries merely to comprehend a little of*
> *this mystery each day.*
>
> —— Albert Einstein

The reconstruction of jets produced in the hadronization process of heavy quarks in ultra-relativistic proton-proton collisions allows to study the quality of pQCD based predictions on heavy quark production as given by [96, 97, 99, 100, 101, 98, 102, 103, 104, 122, 123] and discussed in chapter 3, as well as to establish a baseline for Heavy-quark energy loss studies in heavy-ion collisions.

As the parton-level observables are screened from direct experimental access due to colour-confinement, applicability of local parton-hadron duality[1] (LPHD) [124, 125, 126] allows to deduce parton-level properties from the hadronization products clustered within reconstructed jets.

As beauty quarks are produced at large virtualities $Q \geq 2\,m_{\mathrm{b}}$ that translate into space-time scales of less than $\sim 1/Q = 0.1$ fm, beauty quarks in heavy-ion collisions are experience the entire medium (QGP) evolution, while preserving their flavour identity until hadronization via beauty hadrons. As outlined in e.g. [127, 13] the radiative energy loss of high energy partons interacting with the medium is expected to be larger for gluons than for quarks, and to depend on the quark mass, with beauty quarks losing less energy than charm quarks, light quarks and gluons. The nuclear modification factor of jets (R_{AA}) however is predicted [15] to be mostly sensitive at transverse jet momenta

---

[1]i.e essentially the assumption hadronization is a soft process which does not change significantly the distribution of the produced particles

below 20 GeV/c. Therefore the investigation of the low to intermediate transverse jet momentum range in proton-proton collisions, as it is accessible by ALICE provides an essential reference for any future energy loss studies.

This chapter presents the reconstruction of the charged b-jet spectrum in the momentum range of 5 GeV/c $\leq$ p$_\mathrm{t}^{\mathrm{ch.b-jet}}$ $\leq$ 100 GeV/c in proton-proton collisions at $\sqrt{s} = 7$ TeV using the ALICE detector.

4.1 Methodology
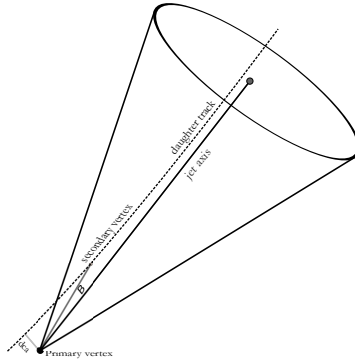
Figure 4.1: *Schematic representation of a beauty meson decay within a jet cone and of one daughter track with the corresponding track impact parameter vector to the primary vertex*

The analysis exploits the on-average larger track impact parameter (c.f. section 2.2.20) d_0 of tracks within beauty jets originating in the long lifetime $c\tau \sim 500 \ \mu$m and high decay multiplicity ($\mathcal{O}(5)$ charged particles per decay) of beauty mesons. The strategy is based on the track counting algorithm that was developed by the D0 Collaboration [128] and is also applied by ATLAS and CMS [129, 130], however with the focus on its application as a b-jet tagger.

Let $\mathcal{J}_i$ be the set of constituent tracks of a reconstructed jet J. For each $t \in \mathcal{J}_i$ the track impact parameter significance $|d_0^t|/\sigma(d_0^t)$ is calculated. If the vector $\vec{d_0}$ connecting the primary vertex and the point of closest approach on the constituent track points into the jet direction a positive sign is assigned to the respective significance if not a negative sign. The resulting quantity

$$d_0 \equiv \mathrm{sign}(\tilde{\mathrm{d}}_0 \cdot \tilde{\mathrm{e}}_{\mathrm{jet}})|\mathrm{d}_0| \tag{4.1}$$

is the signed impact parameter significance (sIP). Throughout this analysis the term impact parameter significance refers to the two-dimensional projection of the impact parameter vector onto the rφ-plane. The impact parameter vector in the sign calculation however uses the full three-dimensional information. The set of resulting impact parameters is then ordered by value starting from the largest value and the first three values are selected as independent observables and are in the following referred to as the $N = 1$, $N = 2$ and $N = 3$ discriminators. Increasing N values therefore favour particle decays with large displacement and simultaneously high decay multiplicity and suppress especially the contributions from the weak decay of strange particles. Uncorrelated background has has a high probability to be assigned a negative sign. Large impact parameters significances have a high probability to come from a B-meson decay however

particle	mass	$c\tau$
B^0	5279.58 ± 0.17 MeV	$455.4\ \mu$m
$B^\pm$	5279.25 ± 0.17 MeV	$492.0\ \mu$m
D^0	1864.83 ± 0.05 MeV	$122.9\ \mu$m
$D^\pm$	1869.58 ± 0.09 MeV	$311.8\ \mu$m
D_s^+	1968.47 ± 0.33 MeV	$149.8\ \mu$m

Table 4.1: *Properties of the dominant heavy flavour meson contributions [72]*

D-meson decays that in the case of $D^\pm$ have a larger average decay length, form the main source of background. In the tagging approach a threshold k can be assigned to the discriminator rejecting every jet with an impact parameter significance of less than k.

The presented analysis exploits the characteristic shape of the $N = 1, 2, 3$ distributions for light-, charm- and beauty-jets to extract the respective contributions using a template fit procedure. The resulting raw beauty jet spectrum is then corrected for the finite detector momentum resolution using unfolding and normalized to the corresponding trigger cross section.

4.2 Analysis structure

The analysis can be subdivided into four distinct parts **_i-iv_** handling the data preparation, measurement and different post-processing stages (See figure 4.2).

Part _i_ is the acquisition of analysis relevant data from the reconstructed proton-proton events. It consists of the event selection, the jet reconstruction, and finally the extraction of the signed impact parameter significance observables including related cut and selection efficiencies, raw-jet spectra and inter-observable correlation coefficients. It also handles the final impact parameter template extraction when presented with simulated proton-proton events.

Part _ii_ is the pre-processing of simulated proton-proton events before template creation. The used PYTHIA6/GEANT3 data sets are re-weighted to match the known measured single particle p_T-spectra and are adjusted for residual detector misalignment as well as for differences in the impact parameter resolution. The used weights are derived from a high-statistics, stand-alone PYTHIA6 simulation and 19 identified particle spectra measured by ALICE.

Part _iii_ includes the extraction of the (beauty jet)/(inclusive jet) fraction using the signed impact parameter significance distribution template fits and the combination of the resulting fractions obtained from the $N = 1$, $N = 2$ and $N = 3$ observables. Finally the result is used to obtain the detector level charged beauty jet spectrum.

Part _iv_ is the unfolding of the spectrum and the final normalization and the comparison of the final result to theory predictions.
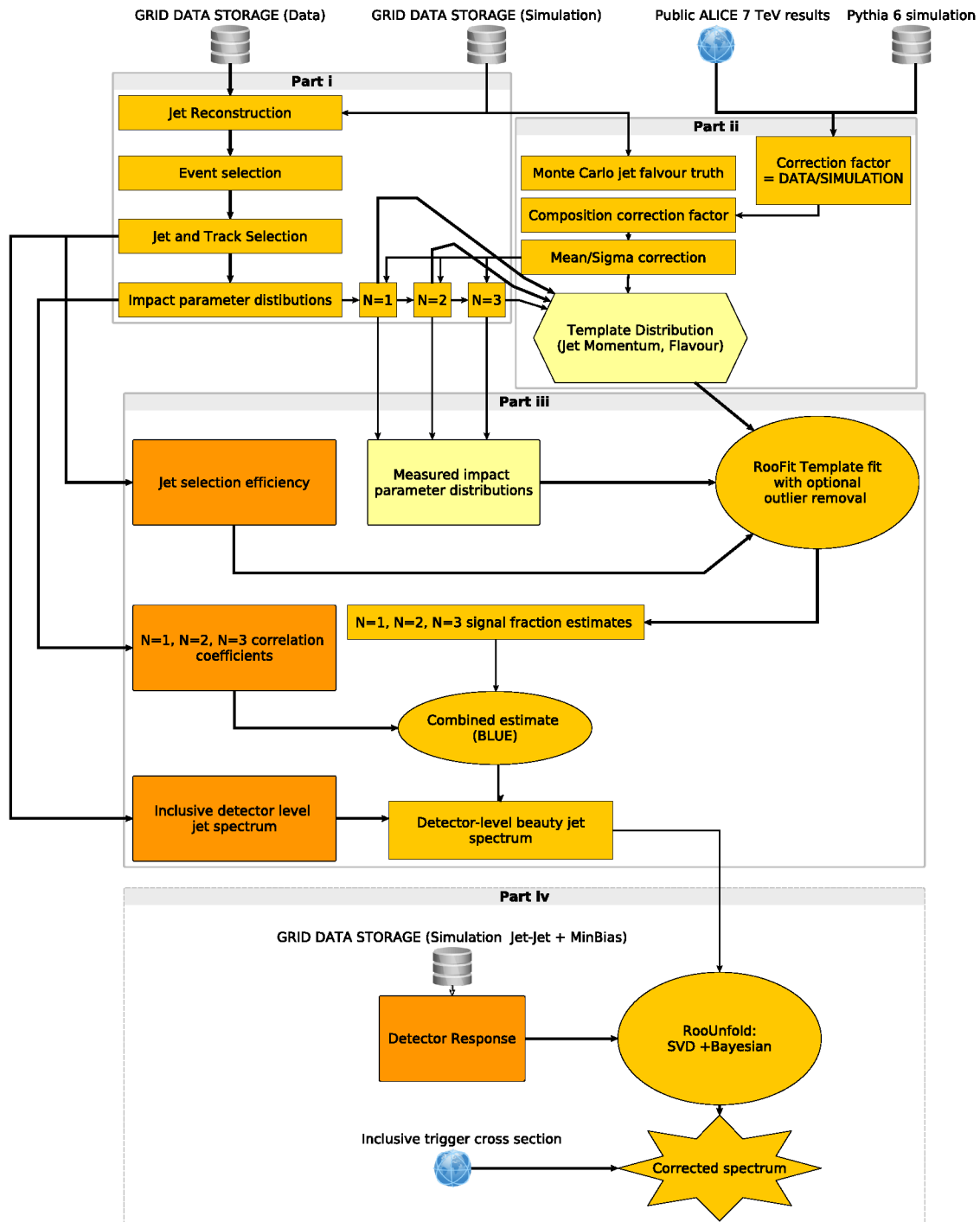
Figure 4.2: *Schematic representation of the analysis structure.*

4.3 Data sample

This analysis is based on ~ 0.42 pb^{-1} of min. bias proton-proton events from 2010 measured at an energy of $\sqrt{s} = 7$ TeV. The data was recoded during five data-taking periods with the ALICE internal designations LHC10b, LHC10c, LHC10d, LHC10e and LHC10f. The five periods consist of several data-taking runs of those 258 runs were pre-selected based on their global data quality, rejecting runs with problematic sub-detector states. Each run corresponds to one uninterrupted data recording interval.

The corresponding run numbers are:

Run numbers :114931, 115186, 115193, 115393, 115401, 116102, 116288, 116403, 116562, 116571, 116574, 116643, 116645, 117048, 117050, 117052, 117053, 117054, 117059, 117060, 117063, 117065, 117077, 117086, 117092, 117099, 117109, 117112, 117116, 117220, 117222, 119159, 119161, 119163, 119841, 119842, 119844, 119845, 119846, 119849, 119853, 119856, 119859, 119862, 120067, 120069, 120072, 120073, 120076, 120079, 120244, 120503, 120504, 120505, 120616, 120617, 120671, 120741, 120750, 120758, 120820, 120821, 120822, 120823, 120824, 120825, 120829, 122375, 124751, 125023, 125083, 125085, 125100, 125101, 125133, 125134, 125140, 125156, 125186, 125295, 125630, 125633, 125842, 125843, 125844, 125847, 125851, 125855, 126004, 126007, 126008, 126073, 126078, 126081, 126082, 126088, 126090, 126097, 126158, 126160, 126167, 126168, 126283, 126284, 126285, 126350, 126351, 126352, 126359, 126403, 126404, 126405, 126406, 126407, 126408, 126409, 126422, 126424, 126425, 126432, 128366, 128486, 128494, 128495, 128498, 128503, 128504, 128505, 128506, 128582, 128590, 128592, 128594, 128596, 128605, 128609, 128611, 128615, 128621, 128677, 128678, 128777, 128778, 128819, 128820, 128823, 128824, 128833, 128834, 128835, 128836, 128843, 128850, 128853, 128855, 128913, 129042, 129512, 129513, 129514, 129515, 129516, 129519, 129520, 129521, 129523, 129524, 129525, 129527, 129528, 129536, 129540, 129586, 129587, 129599, 129639, 129641, 129647, 129650, 129651, 129652, 129653, 129659, 129666, 129723, 129725, 129726, 129729, 129734, 129735, 129736, 129738, 129742, 129744, 129959, 129960, 129961, 129962, 129966, 129983, 130149, 130151, 130157, 130158, 130168, 130172, 130178, 130342, 130343, 130354, 130356, 130358, 130360, 130375, 130479, 130480, 130481, 130517, 130519, 130520, 130524, 130526, 130601, 130608, 130609, 130620, 130621, 130623, 130628, 130696, 130704, 130793, 130795, 130798, 130799, 130802, 130803, 130804, 130834, 130840, 130842, 130844, 130847, 130848, 130850, 133006, 133007, 133010, 133327, 133330, 133563, 133670, 133762, 133800, 133920, 133969, 133982, 134198

4.3.1 Event selection

The ALICE minimum bias trigger MBOR trigger condition is used for on-line event selection requiring at least one hit in the SPD or either of the two forward VZERO detector arrays (see 2.2.9). The trigger cross section was measured via van der Meer scans [57] to be $\sigma_{MBOR} = 62.2 \pm 2.6$ mb corresponding to $85.2^{+6.2}_{-3.0}\%$ of the total inelastic proton-proton cross section. During the data extraction a further off-line vertex selection is used (see table 4.2) to ensure a optimal impact parameter resolution. With increas-

Parameter	Condition
$Z_{\text{Vertex}}^{\text{Tracks}}$	< 10 cm
$N_{\text{constributors}}^{\text{Tracks}}$	≥ 3
$\chi_{\text{Vertex}}^{2}/\text{ndf}$	$< (3.5)^2$

Table 4.2: *Additional primary vertex requirements.*

ing interaction rate the intervals separating different collisions become shorter and the probability for recording multiple events at the same time increases. These events are called pileup-events and can be characterized by having multiple interaction vertices and a relatively small number of SPD tracklets compared to the re-constructed number of SPD clusters. These events are rejected based on the presence of multiple reconstructed vertices and rejecting those events with $N_{\text{Clusters,SPD}} > 65. + 4 \cdot N_{\text{Tracklets,SPD}}$. In the ideal pileup-free scenario a linear correlation between both observables is expected.

Figure 4.3 shows the impact of the pileup rejection and the threshold cut onto the SPD cluster vs tracklet distributions[2].
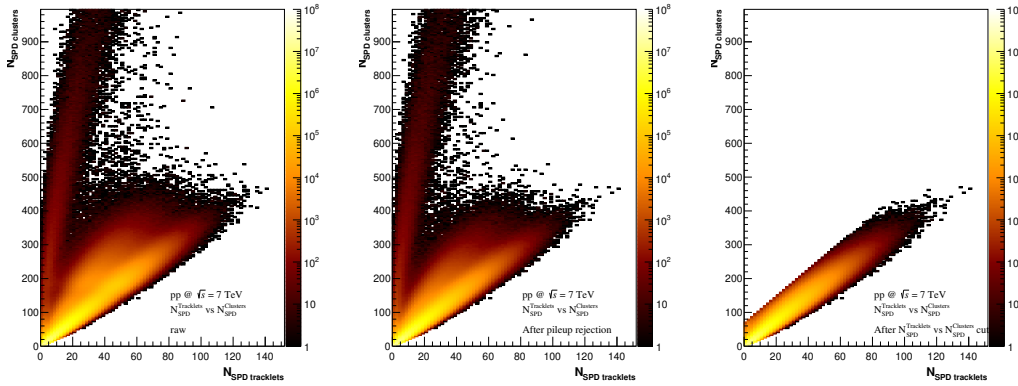
Figure 4.3: $N_{\text{Clusters,SPD}}$ *vs.* $N_{\text{Tracklets,SPD}}$ *distributions before pileup rejection (left) after multi-vertex pile-up rejection (centre) and after explicit linear cut i.e.* $N_{\text{Clusters,SPD}} > 65. + 4 \cdot N_{\text{Tracklets,SPD}}$ *(right).*

This step is important as none of the available detector simulations includes pile-up events thus the increased uncorrelated background would therefore lead to a distortion of the extracted template distributions.

The remaining pile-up is found to be negligible [34].

Table 4.3 summarizes the available MBOR statistics an the number of accepted events used in this analysis.

---

[2]Private communication with Daniel Mühlheim

Period	Number of min. bias events	Number of accepted events
LHC10b	29.511.154	18.873.998
LHC10c	80.761.387	54.046.652
LHC10d	179.249.647	105.239.720
LHC10e	175.115.966	103.950.984
LHC10f	50.603.692	31.247.708
Total	515.241.846	313.359.062

Table 4.3: *Available and accepted 2010 proton-proton events for globally good runs.*

4.4   Track selection

Several sets of track selections are used to ensure a homogeneous jet reconstruction efficiency with a good jet momentum resolution as well as a stable 2d impact parameter resolution of order of 65 μm for tracks with more than 1 GeV/c. For the jet reconstruction two sets of tracks are used. One consists of TPC stand-alone tracks used to fill the holes in the ITS acceptance and one of reconstructed tracks with both ITS and TPC points. The combination of both steps of tracks is often referred to as hybrid tracks. For the track impact parameter calculation additional cuts are applied to the ITS+TPC subset of tracks. A summary of the track selection requirements is listed in table 4.4. The decay length corresponds to the distance between the distance-of-closest approach between the jet axis and the considered track and the distance-of-closest approach of the primary vertex and the track. It is required to reject rare tracks with very large impact parameter likely to come from strange particle decays or reconstruction artefacts. The cut on the distance-of-closest approach between the jet axis and the track is also chosen to suppress the impact of strange particles. The track requirements used in the jet part of this analysis are essentially the same as the ones used in the published inclusive 7 TeV jet analysis [131] however omitting the standard primary particle selection requiring a track impact parameter of less than $0.0105 + 0.0350/p_{\mathrm{T}}^{1.1}$ cm to include tracks with non-negligible impact parameters. The geometric distribution of the both input track sets as well as for the combined hybrid tracks is shown in figure 4.4.

Track selection criterion	Global tracks	ITS tracks	sIPS analysis
	$70 + 30/20 \cdot p_T \leq 20 \text{GeV/c}$		
Min. number of clusters TPC	$70 > 20 \text{GeV/c}$	*	100
Max. χ^2/cls. TPC	4	*	*
Min. p_T	0.15 GeV/c	*	1 GeV/c
No kink/daughter	*	*	*
Shared TPC cls. fraction	0.4	*	*
Max. global χ^2	36	*	*
Preudorapidity range	(-0.9,0.9)	*	*
TPC Refit	*	*	*
ITS Refit	n/a	*	*
DCA(2d) of track to Vertex XY	n/a	< 2.4 cm	*
DCA(2d) of track to Vertex Z	n/a	< 2.4 cm	*
Max. χ^2/cls. ITS	n/a	36	*
Does not require σ to vtx	n/a	*	*
Has hits in both SPD layers	n/a	n/a	*
Max. DCA track to jet	n/a	n/a	0.07 cm
Max. linear decay length	n/a	n/a	10 cm
Has recalculated vertex	n/a	n/a	*
Hits in x ITS layers	n/a	n/a	x=6

Table 4.4: *Track selections (* indicates "true" or "same as defined in the previous column").*
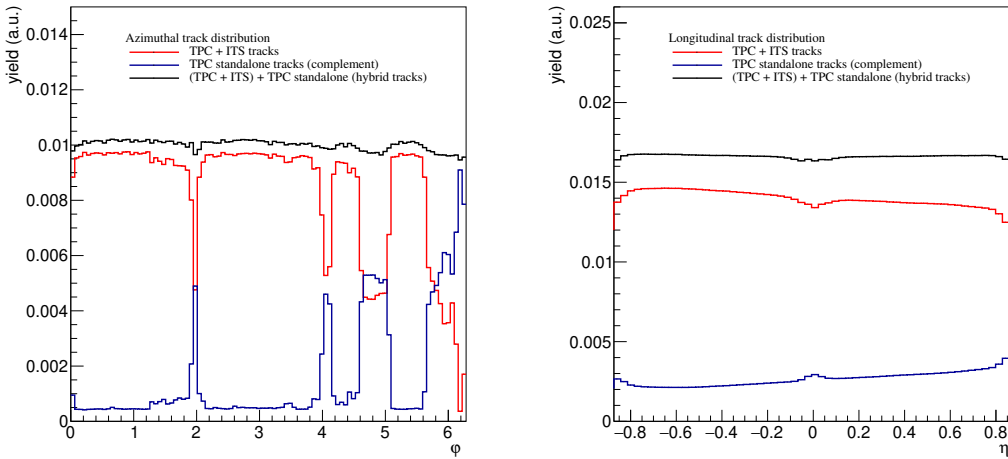
Figure 4.4: *η and φ distributions for TPC+ITS, TPC stand-alone and resulting hybrid tracks.*

The regions with reduced acceptance, visible in the ITS+TPC track geometrical distributions correspond to regions with ITS modules that were temporarily or are permanently disabled, defective have a lower track reconstruction efficiency.

To be accepted for the impact parameter calculation procedure a track has to fulfil additional criteria that were iteratively optimized to constitute a good compromise between accepted tracks and the expected impact parameter resolution. The final track cuts as used in this analysis are summarized in table 4.4. Three additional selections of track cuts with slightly modified ITS and TPC requirements have been studied. The modifications to the default cut selection are listed in table 4.5.

Selection	ITS hits	SPD hits	additional changes
default	6	2	n.a.
i.	>3	≥ 1	n.a.
ii.	>2	≥ 1	n.a.
iii.	>2	≥ 0	$N_{cls.}^{TPC} \geq 80$

Table 4.5: *Summary of modified ITS/TPC track selection cuts.*

The minimum track momentum of 1 GeV/c is selected to achieve a impact parameter resolution $< 65 \mu m$ and a homogeneous resolution for different particle species (see figure 4.5).
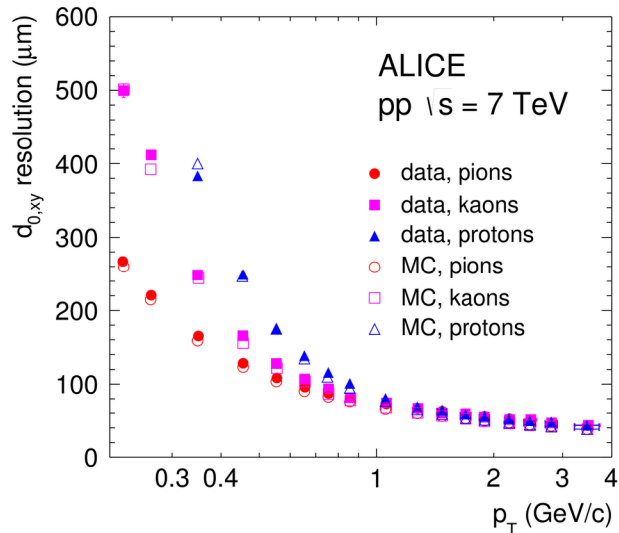
Figure 4.5: *2d-impact parameter resolution for different particle species.*

Figure 4.6 shows the effect of a loser requirement on the number of hits in different ITS layers onto the N=1, N=2, N=3 signed impact parameter distributions. Gradually reducing the required number of global ITS hits with at least one SPD hit expectedly leads to loss in resolution, decreasing from the nominal $\mathcal{O}(d_0) = 65$ μm to about $\mathcal{O}(d_0) = 78$ μm estimated by a Gaussian fit to the left, mostly detector resolution defined part

of the distributions. Removing the SPD requirement completely gives rise to a bump
structure on the flanks of the distributions originating from the photo-conversions in
the SPD layers. Here the signed impact parameter distributions are shown as they can
directly be related to the measured impact parameter resolution and show more directly
the geometric correlation between a certain input factor, as for example the effects of
photo conversions and the resulting distribution shape.
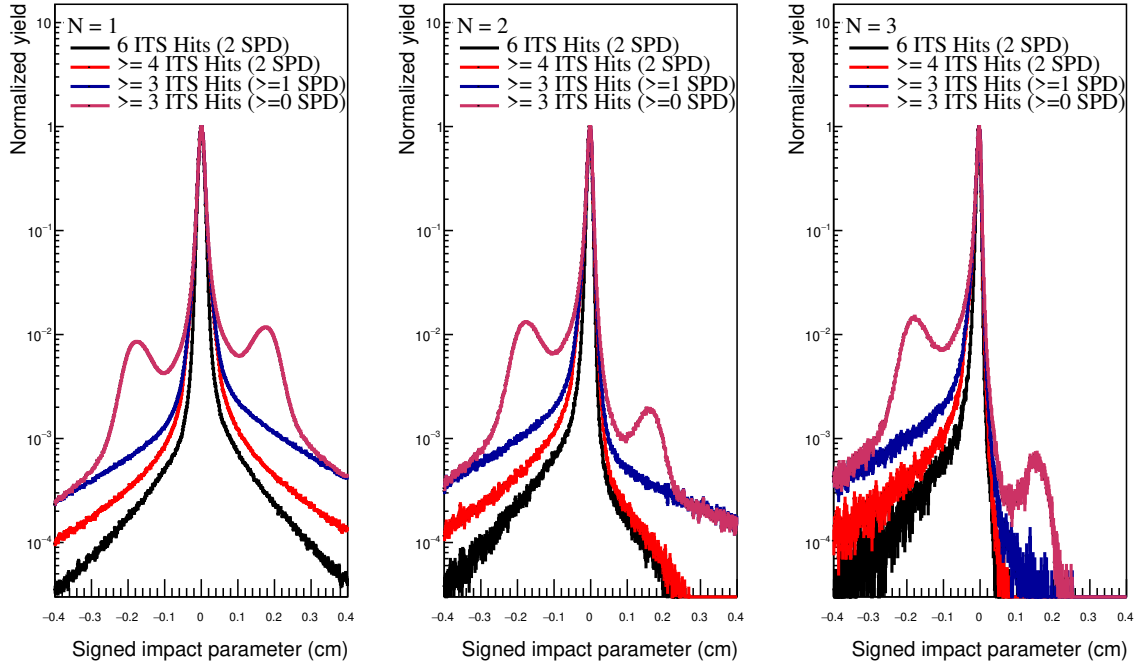
Figure 4.6: *Impact of different ITS requirements on the signed N=1, 2, 3 impact parameter distributions.*

4.5   Charged jet reconstruction

Global and TPC tracks, as defined in the previous section, are used as input for the
anti-k_{T}[121] and k_{T} jet clusterizers as implemented in FASTJET 3.0.6 [132, 133] interfaced via the ALICE jet analysis framework. A resolution parameter $R = 0.4$ are
reconstructed from reconstructed hybrid tracks with a minimum transverse momentum
of $p_{\mathrm{T}}^{\mathrm{track}} > 150$ MeV/c. Only jets within the fiducial acceptance i.e. $|\eta| < 0.5$ are
accepted.

When running on simulated data the same configuration is used on the track level. Since
MC particle level information is available a second jet finder is run using the generators
(PYTHIA) particle stack. Both jets are geometrically matched (see section 4.11.1). A

track-level MC jet is identified as a beauty-jet, if a beauty quark is found within the jet cone of the matched particle-level jet, as a charm jet if no beauty quark but a charm quark is found. In all other cases the jet is labelled as a light jet.

In the inclusive charged jet analyses the effect of the underlying event on the jet energy scale was found to be less than 2.5% (e.g. [131]) however starting at transverse jet momenta of about 20 GeV/c. Going to lower jet momenta a more significant impact is expected as the jet momentum approaches the average background momentum density that is at the order of 1 GeV/c. The analysis is performed with and without the underlying any event subtraction. The UE momentum density is estimated using a description that was developed by CMS for sparsely filled events [134]. Each jet momentum is corrected for the UE contribution by subtracting:

$$p_{jet,T}^{corr.} = p_{\text{T,jet}} - A_{jet} \cdot \rho \tag{4.2}$$

with A being the jet area and

$$\rho = \text{median} \left\{ \frac{\text{p}_\text{T}^\text{i}}{\text{A}_\text{i}} \right\} \cdot \frac{\text{Covered area}}{\text{Total area}} \tag{4.3}$$

Here the underlying event is sampled using a k_T jet finder to sample the background starting from the low momentum particles. The used jet areas A_i are estimated by introducing so-called ghosts, zero-momentum particles that basically fill the whole available acceptance without altering the reconstructed jet properties. Figure 4.7 shows the measured inclusive $d^2N/dp_T d\eta$ charged jet spectra both with and without the UE subtraction. In consistency with the published inclusive analysis the impact of the UE above a charged jet transverse momentum of 20 GeV/c is negligible. However below this threshold the difference in the spectra becomes significant. The impact of the underlying event on the final beauty-jet spectrum is also assessed in analysis.
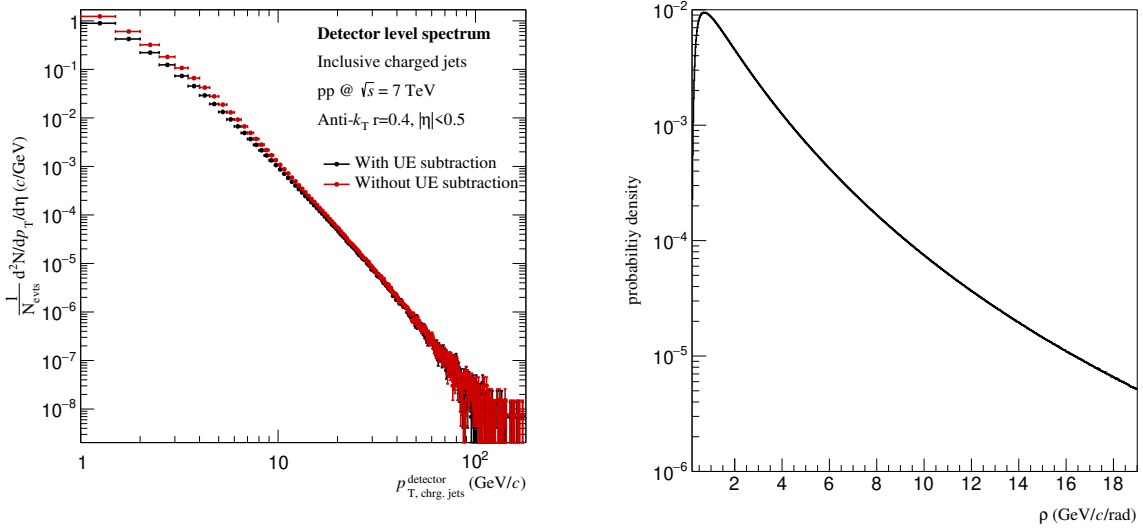
Figure 4.7: *Raw charged inclusive detector level jet with and without UE subtraction (left), Distribution of the measured underlying event momentum density (right).*

4.6   Signed impact parameter distributions

The jet correlated signed impact parameter for the selected detector level analysis p_{T}-bins are shown in figures 4.9, 4.10 and 4.11. To account for the rapidly decreasing jet yield with increasing jet momentum a non-equidistant binning is used in this analysis

$$\left(\; 4, 5, 6, 8, 10, 12, 15, 20, 25, 30, 40, 50, 70, 100 \; \right) \mathrm{GeV}/c \qquad (4.4)$$

Figure 4.8 shows a direct comparison of the $N = 1$, $N = 2$ and $N = 3$ inclusive signed impact parameter significance distributions normalized to the peak value. The distributions show a decreasing mean value with increasing N that might point to the effect of further residual strange particle background especially for $N = 1$. For $N = 2$ and $N = 3$ the resulting distributions become comparable in the negative significance range in agreement with the hypothesis that this part of the distribution is mainly defined by detector resolution effects and uncorrelated background.
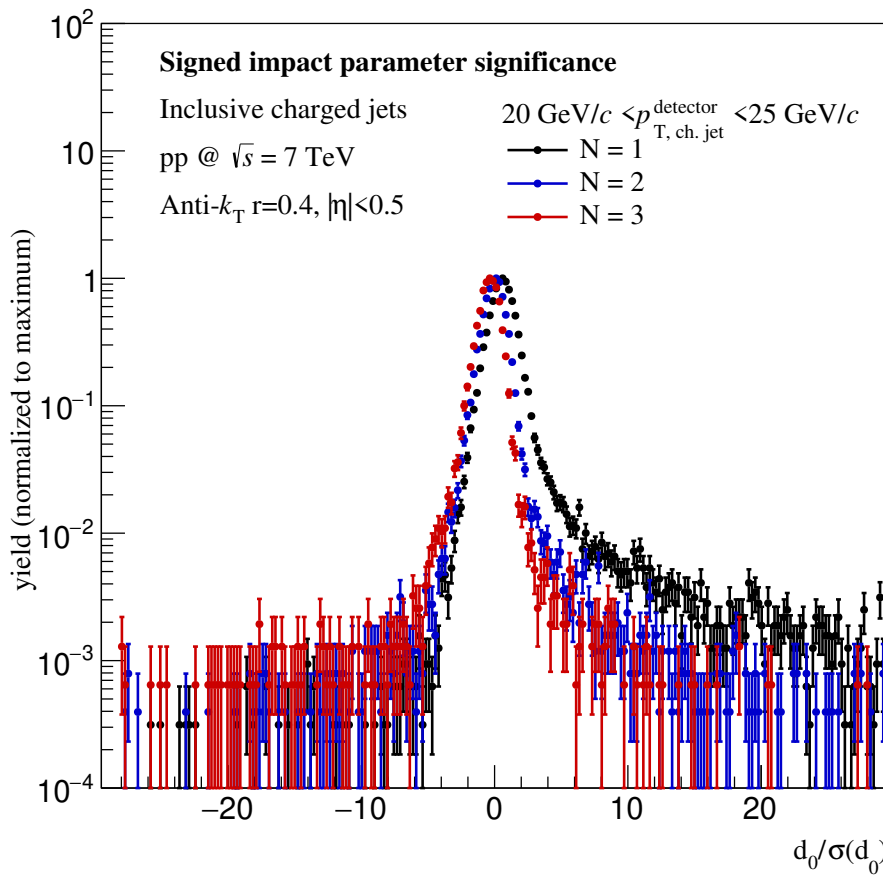
Figure 4.8: *Example comparison of $N = 1$, $N = 2$, $N = 3$ inclusive impact parameter significance distributions as intermediate transverse jet momentum.*
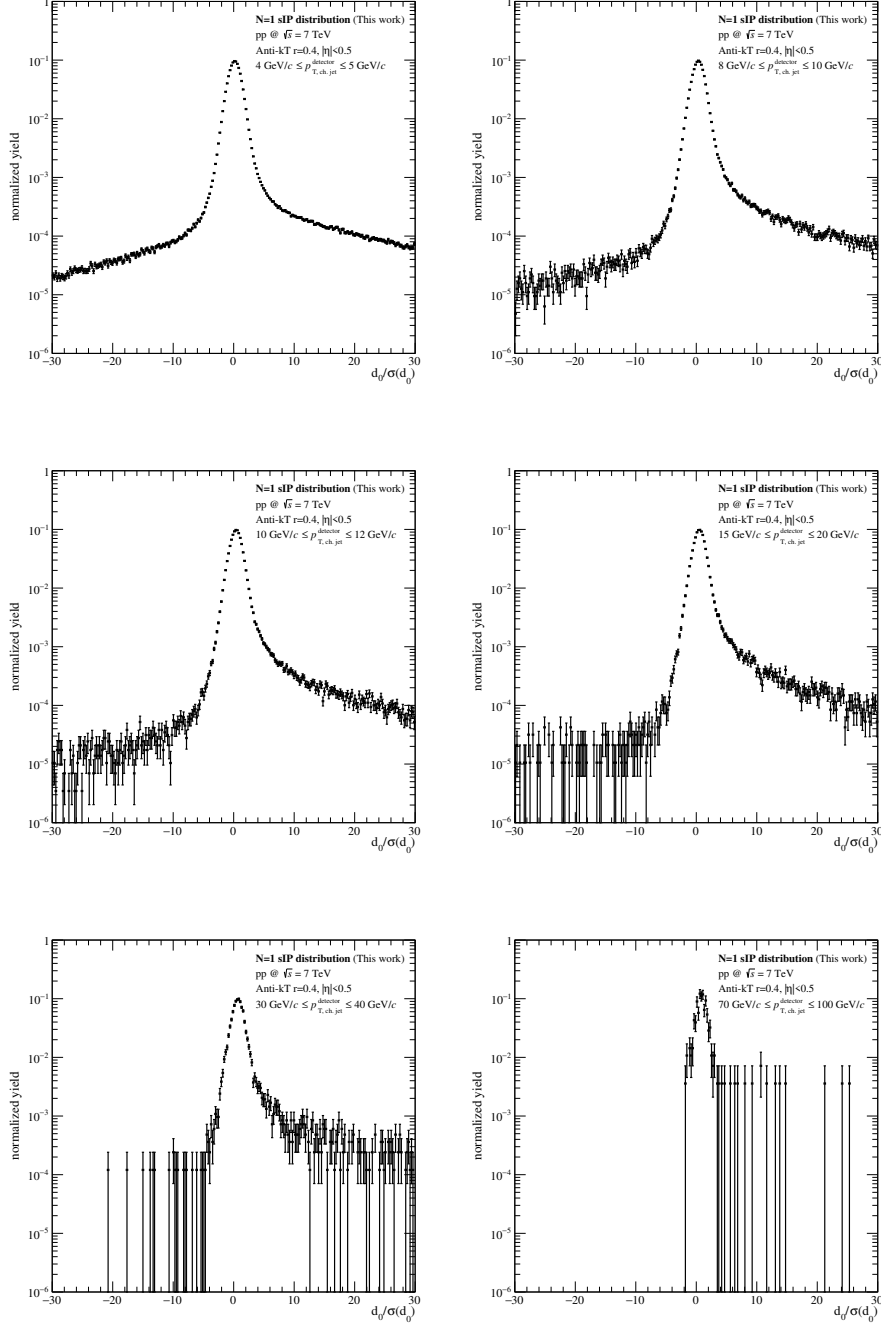
Figure 4.9: *N=1 template distributions extracted from ALICE 2010 proton-proton collisions at $\sqrt{s} = 7$ TeV. The full set of distributions for all momentum bins can be found in the appendix A.1.*
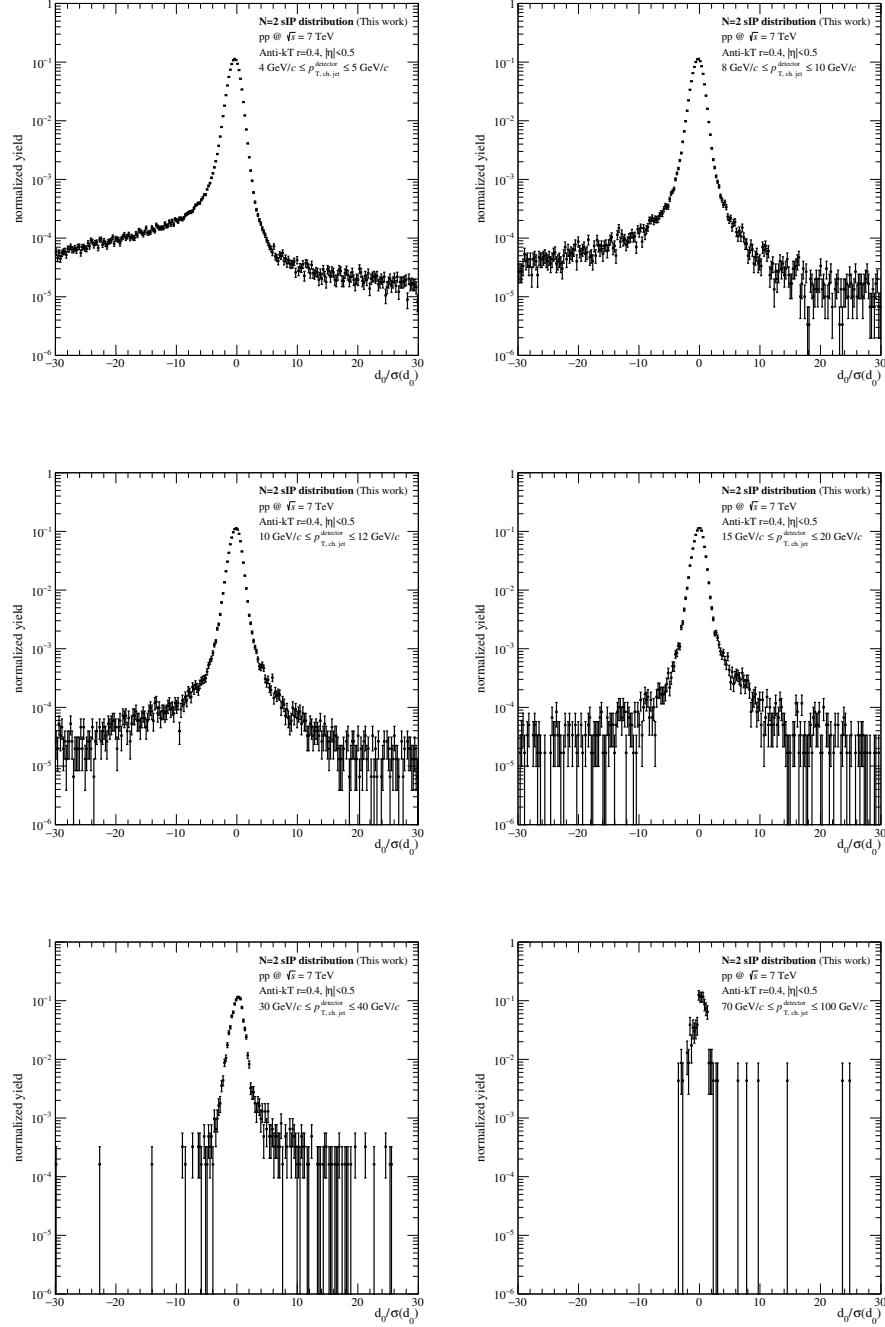
Figure 4.10: *N=2 template distributions extracted from ALICE 2010 proton-proton collisions at $\sqrt{s} = 7$ TeV. The full set of distributions for all momentum bins can be found in the appendix A.1.*
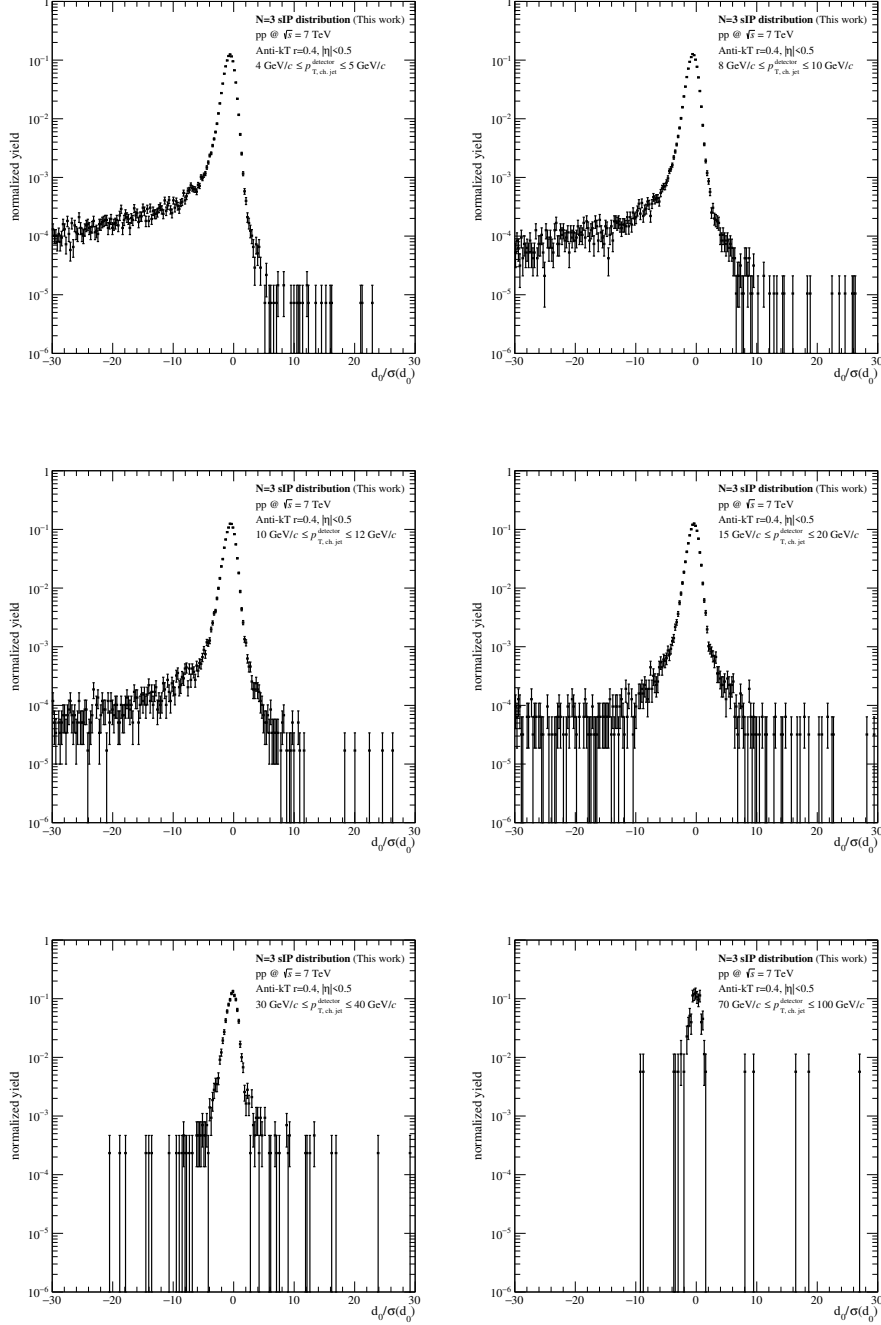
Figure 4.11: *N=3 template distributions extracted from ALICE 2010 proton-proton collisions at $\sqrt{s} = 7$ TeV. The full set of distributions for all momentum bins can be found in the appendix A.1.*

4.7 $N = 1, 2, 3$ discriminator correlations

The ordering of the impact parameter significance in the discriminator extraction introduces partial correlations that have been estimated using the Pearson coefficients extracted from two-variable same jet correlation plots. As these plots imply to have values for $N = 1$ and $N = 2$, $N = 2$ and $N = 3$ or $N = 1$ and $N = 3$ the resulting covariance will later be scaled account for the fact that not all jets have three discriminator values due to track selection cuts (See figure 4.28).

Four conservative estimates for the correlation matrices in different momentum ranges have been defined and used as input for the best linear unbiased estimate (BLUE). For each bin and each statistical variation the BLUE has been calculated. The histogram based Pearson coefficient extraction was also compared to a tree container based correlation estimation and found to be in full agreement.
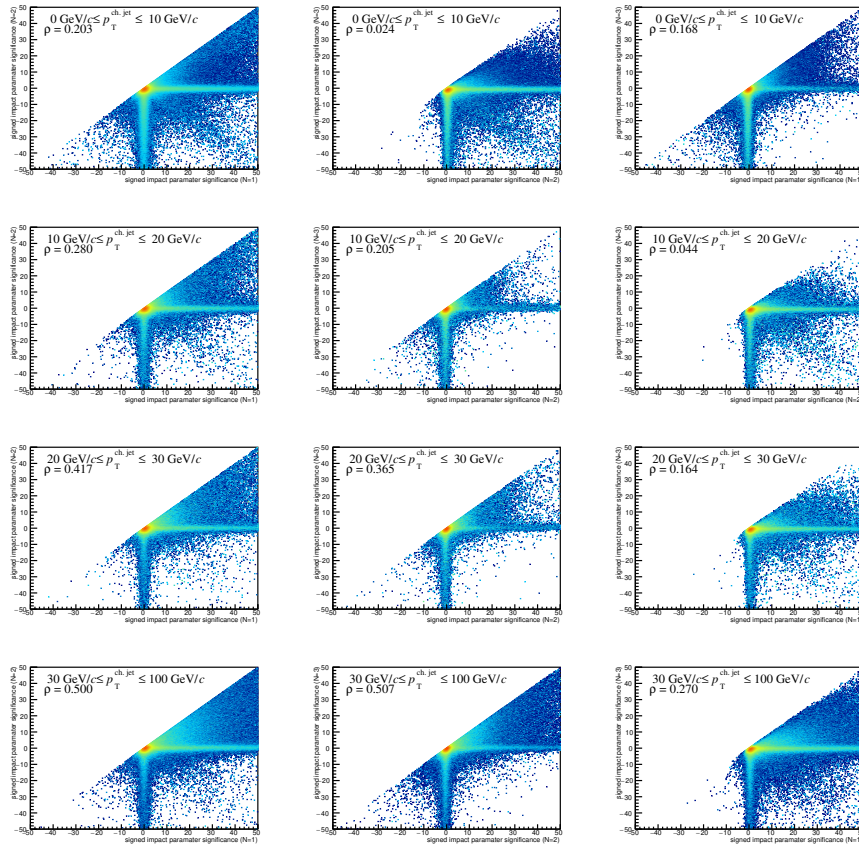
Figure 4.12: *Two-variable ($N = 1, 2, 3$) impact parameter correlations.*

$$
\underbrace{\begin{pmatrix} 1 & 0.2 & 0.16 \\ 0.2 & 1 & 0.03 \\ 0.16 & 0.03 & 1 \end{pmatrix}}_{p_T^{\text{ch.jet}} < 10 \text{ GeV/}c} \quad
\underbrace{\begin{pmatrix} 1 & 0.25 & 0.03 \\ 0.25 & 1 & 0.13 \\ 0.03 & 0.13 & 1 \end{pmatrix}}_{10 \text{ GeV/}c \le p_T^{\text{ch.jet}} \le 20 \text{ GeV/}c} \quad
\underbrace{\begin{pmatrix} 1 & 0.42 & 0.16 \\ 0.42 & 1 & 0.37 \\ 0.16 & 0.37 & 1 \end{pmatrix}}_{20 \text{ GeV/}c \le p_T^{\text{ch.jet}} \le 30 \text{ GeV/}c} \quad
\underbrace{\begin{pmatrix} 1 & 0.50 & 0.27 \\ 0.50 & 1 & 0.5 \\ 0.27 & 0.5 & 1 \end{pmatrix}}_{p_T^{\text{ch.jet}} \ge 30 \text{ GeV/}c} \quad (4.5)
$$

4.8   Monte Carlo data sample

The selection of the simulated data is a crucial ingredient to this analysis. The available ALICE Monte Carlo productions for the 2010 proton-proton runs are a combination of PYTHIA6 for event generation paired with GEANT3 for the full detector simulation. Several selections were studied including the use of minimum bias (MB) simulations, simulations using a implicit generator level jet trigger performed in different event p_T^{hard} bins and a combination of both.

In this analysis two sets of simulated PYTHIA6/GEANT3 events with ALICE internal designations LHC14j4b-f and LHC15g6d-e are used (see also table 4.6). LHC14j4b-f consist of approximately 301 million minimum bias events after event selection while LHC15g6d/e on the other hand consist of about 193 million events generated in so-called p_T-hard bins, with a generator level jet trigger $E_T^{Jet} > 10$ GeV. The production is split into several p_T^{hard} bins for those each generated event has to have an p_T-hard in the respective interval and at least one jet fulfilling the E_T^{Jet}-criterion to be accepted and to be passed to GEANT3 for the full detector simulation. As the event generation is much faster than the detector simulation, step sufficient statistics can be generated even at large transverse jet momenta. Due to the PYTHIA level jet trigger condition these simulations are often named Jet-Jet simulations. LH15g6d/e consist of 20 p_T-hard bins $(5, 7, 9, 12, 16, 21, 28, 36, 45, 57, 70, 85, 99, 115,\ 132, 150, 169, 190, 212,\ 235, 1000000)$ GeV/c. To combine the different bins one needs to rescale the relative respective observables with the weight of the bin defined by its integrated cross section and the number of trials used in the event production.

$$w_{bin} = \frac{\sigma^{bin}}{N_{Trials}} \tag{4.6}$$

While the minimum p_T-hard is 5 GeV/c the question arises if the jet-trigger introduces a bias that may affect the final results. A deviation due to this additional requirement was found and can be seen e.g. in the low momentum part of the inclusive charged jet spectrum (see 4.13).

In the following the descriptive term "Jet-Jet MC" is used for the LHC15g6e-d dataset , while the term "MB MC" is used for LHC14j4b-f.
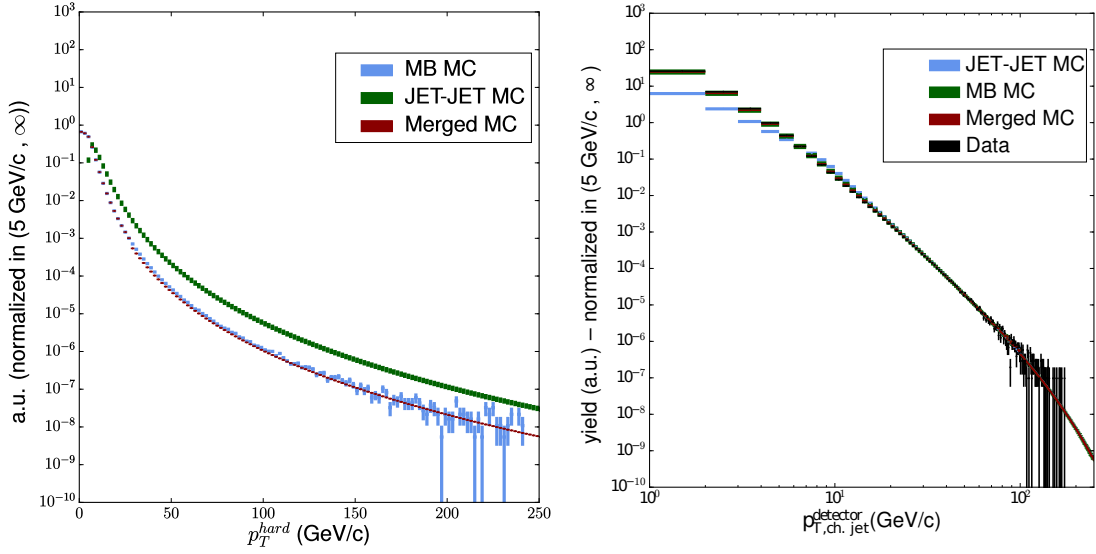
Figure 4.13: *(left)Comparison of the p_T-hard distribution in MB MC, Jet-Jet MC (left) and the merged ($k_{\mathrm{thres.}} = 28$ GeV/c) MC dataset. (right) inclusive charged detector level jet spectrum(right).*

To build a merged data set both samples Jet-Jet MC and MB MC are combined by defining a p_T^{hard}-threshold $k_{\mathrm{thres.}}$ with the requirement that the shapes of the p_T^{hard} distributions agree above the threshold value. $k_{\mathrm{thres.}}$ has been found to be in the range of $p_T^{\mathrm{hard}} = 20 - 30$ GeV/c (see 4.13 (left)) thus a $k_{\mathrm{thres.}} = 28$ GeV/c was chosen from the already available p_T^{hard}bin-limits in Jet-Jet MC.

Events with a $p_T^{\mathrm{hard}} > k_{\mathrm{thres.}}$ were rejected for MB MC and the resulting analysis outputs were weighted using the corresponding bin weights w_i. The comparison of the raw jet spectrum in data, Jet-Jet simulation and merged simulation are shown in figure 4.13 (right)

production	simulation type	N_{events}
LHC14j4b	MB Pythia6(Perugia11)/Geant3	31.643.500
LHC14j4c	MB Pythia6(Perugia11)/Geant3	86.324.000
LHC14j4d	MB Pythia6(Perugia11)/Geant3	191.349.000
LHC14j4e	MB Pythia6(Perugia11)/Geant3	193.977.000
LHC14j4f	MB Pythia6(Perugia11)/Geant3	59.660.000
LHC15g6d	Jet-Jet Pythia6(Perugia11)/Geant3	93.242.000
LHC15g6e	Jet-Jet Pythia6(Perugia11)/Geant3	99.758.500

Table 4.6: *List of used Monte Carlo datasets.*

Furthermore a comparison to Monte Carlo show a difference in resolution related to the residual misalignment of the detector (see figure 4.14).
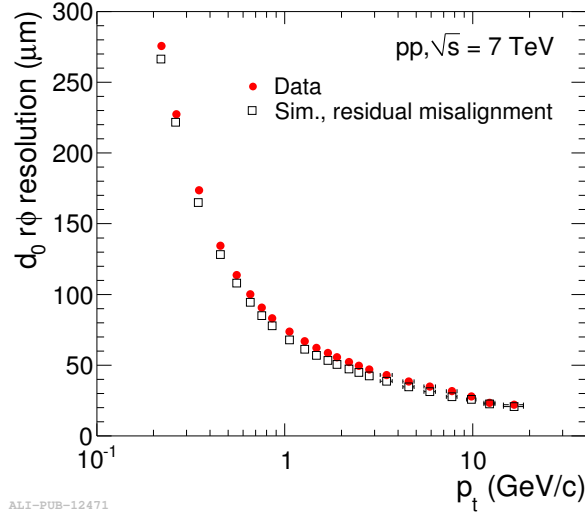
Figure 4.14: *Track impact parameter resolution comparison Data to* PYTHIA*6/*GEANT*3.*

To assure a good impact parameter quality the run dependence of d_0 impact parameter mean value and resolution in data was studied and is shown for data in figure 4.15. Here the impact parameters are calculated for all accepted tracks. As no significant run dependence was observed for the used Monte Carlo sample only the integrated mean and resolution values are indicated via red lines, as they do not include the equivalent run-by-run variations and should therefore be the same within the respective fit uncertainties.

Runs with negative impact parameter mean value coincide with a reversed L3 magnet polarity. This unexpected dependence was caused by a bug in the ALICE reconstruction software handling the propagation of electron-hole pairs in the ITS. A fix was pushed in February 2017, however data prior to the fix was not re-reconstructed.
The investigation related to the observed offset however occupied a considerable fraction of the total duration of the presented analysis. During this period several modifications to the vertex reconstruction, the impact parameter calculation, the track selection as well as several correction strategies were explored, however without any significant impact on the final distributions. Therefore the detailed discussion of these retrospectively ineffective measures is omitted in this analysis summary. Considering the relative event contributions from each run it can be estimated that periods LHC10d and LHC10e dominate with their offset of 7–9μm. In this Analysis both runs with $B > 0$ and $B < 0$

are used, however to asses the impact of the different offsets the analysis is repeated using $B > 0$ runs ($B < 0$) as a cross check. The $B < 0$ runs corresponds to about 26.8% of the available accepted statistics.

It is expected that using the available Monte-Carlo productions, that do not reproduce basic features of the measured impact parameter distributions in a impact parameter template fit based analysis will perform poorly.

In this analysis a multi-step correction strategy is used to account for both the observed detector level differences as well as for measured difference in the particle distributions on level of the event generation.
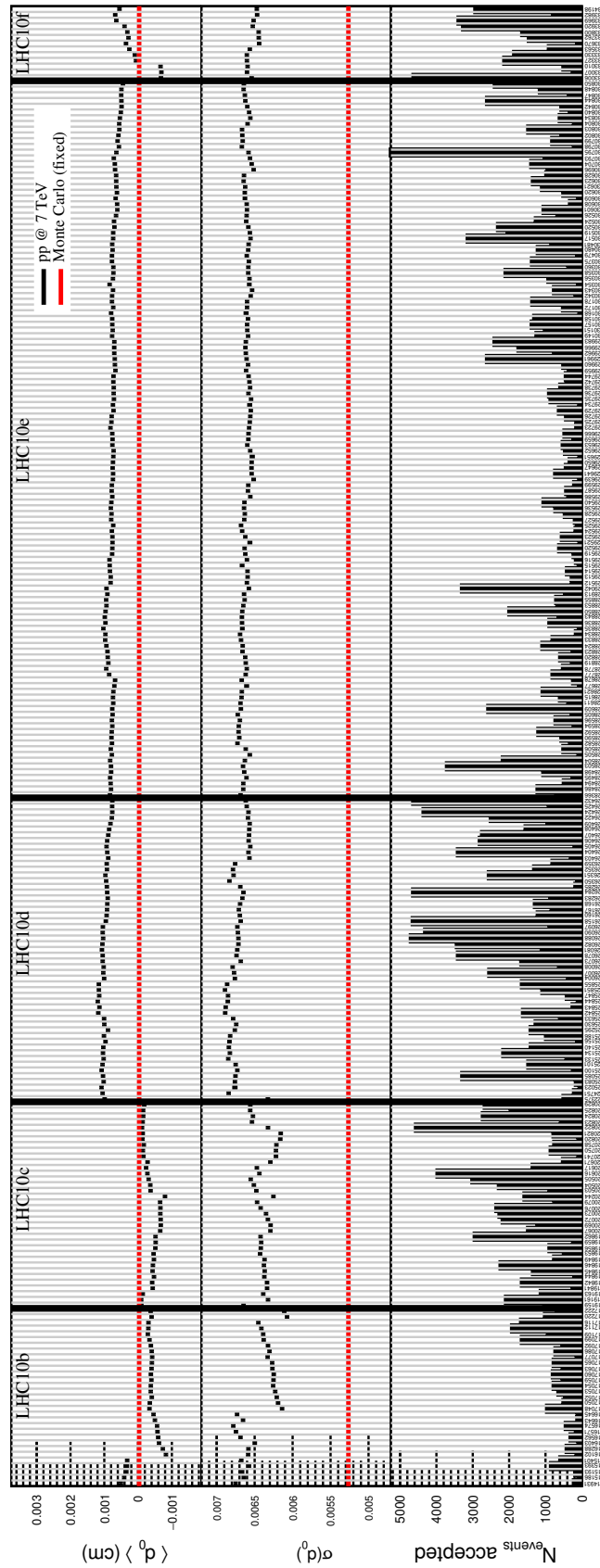
Figure 4.15: *Quality assurance: Mean and sigma value of the transverse impact parameter and the total number of accepted events.*

4.8.1 Particle composition re-weighting

PYTHIA6 [113] does not reproduce the measured relative particle compositions. While inclusive jet observables are less sensitive to this, impact parameter distributions are essentially defined by the mixture of different primary and secondary particle sources. Any relative change in the composition will therefore directly influence the shape of the distributions rendering them less accurate for any shape based template fit procedure. An effective track-wise re-weighing procedure is applied in the following way to reduce the impact of said generator level inaccuracies. The template generation is done using the available full PYTHIA6/GEANT3 simulations. After the signed impact parameter calculation for a jet constituent track, the MC particle connected to the re-constructed track is obtained from the generator stack. The particle is identified via its PDG designator and matched against a list of particles for that re-weighting factors are available. In most cases however the correction is applied based on the particles mother or grandmother and the actual matching consists of several chained iterations of loops through the particles ancestry. This procedure is required to avoid problems with ambiguities or of double counting that could otherwise arise due to feed-down.

4.8.2 Track-particle matching

1. Obtain (MC)particle from PYTHIA6 stack

2. Find particle or mother particle species:

   (a) Follow chain of mothers until considered particle species is found for: $K^0_{S/L}$[3] and Λ^0.

   (b) If none found → Repeat for $D^0, D^+, D^{*,+}, D^*_s, \Lambda_c, \Lambda_b, B^0, B^+$

   (c) If none found → Repeat for Ω^- ande Ξ^-

   (d) If none found → Repeat for $\pi^0, \eta^0, \eta^{'}, \phi, \rho$ and ω

   (e) If none found → Repeat for $\pi^{\pm}$ and $K^{\pm}, p$

3. Return weight for given particle/mother particle p_{T}.

The weight returned after successful identification is defined as the fraction of the p_{T}-dependent yields for a given particle species as measured in data over the same yields in PYTHIA6 (Perugia 11 tune).

$$w_i = \frac{N_{\mathrm{data}}}{N_{\mathrm{simulation}}} \qquad \text{with } i \in \{\text{particle type}\} \qquad (4.7)$$

---

[3]K^0_S weights used for K^0_L

As all published data is fully corrected for any detector effects and the available full PYTHIA6/GEANT3 simulations are limited in statistics as well are computationally expensive to extend, a stand-alone PYTHIA6 simulation was used to generate approx. 10 billion events utilizing the "Kronos" cluster computation facilities at (Helmholtzzentrum für Schwerionenforschung GmbH) GSI. The simulation was setup to exactly match the generator level configuration of the ALICE PYTHIA6/GEANT3 simulations used in this analysis to ensure that the extracted weights are applicable. Before the weights are extracted the available measurements are parametrized using suitable fit functions (Tsallis [135], Bylinkin-Rostostsev [136]). For rare particles, such as the B mesons, for that no measurements are available, FONLL [122, 137] predictions are used as reference and m_T-scaling in case of not-measured light mesons. Table 4.7 summarizes the available input references.

The m_T-scaling is a qualitative scaling first observed at the CERN SPS by the WA80 collaboration [138] and is used here to derive a approximation of the unmeasured light meson spectra from the measured π^0 spectrum. This procedure is expected to give acceptable results for $m_\mathrm{T} \ll p_\mathrm{T}$ where the spectra should satisfy the expected scaling behaviour and agree modulo a global normalization factor c that has to be determined experimentally. Technically the measured neutral pion spectrum is parametrized as a function of its transverse mass $m_\mathrm{T} = \sqrt{p_\mathrm{T}^2 - m_{\pi^0}^2}$. To obtain the derived spectra, the mass in pion parametrization is replaced the mass of the desired meson and the resulting shifted parametrization is scaled with the corresponding relative scaling factor. For a more rigorous discussion see [139].
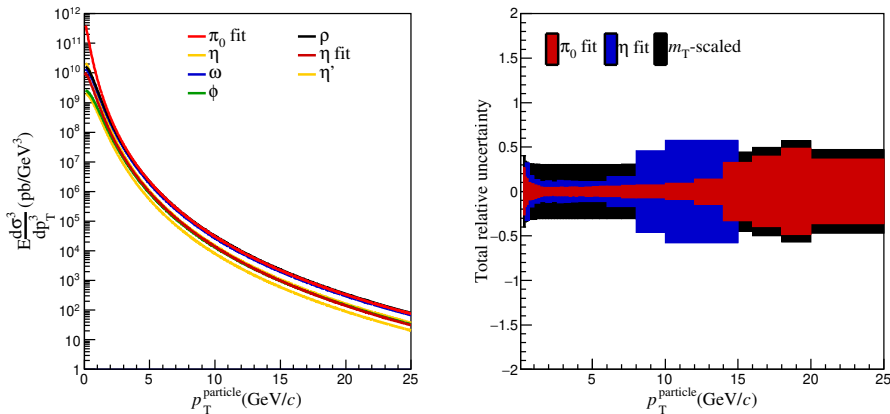
Figure 4.16: *Light meson particle reference spectra(left). Associated total relative uncertainties (right).*

particle species	Reference publication
$\pi^+ + \pi^-$	EPJC 75 (2015) 226 [140]
$p + \bar{p}$	EPJC 75 (2015) 226 [140]
$K^- + K^+$	EPJC 75 (2015) 226 [140]
π^0	Phys. Lett. B 717 (2012) 162-172 [141]
η	Phys. Lett. B 717 (2012) 162-172 [141]
ω	From m_{T}-scaling ($c_\omega = 0.9 \pm 0.06$) [139]
$\eta^{'}$	From m_{T}-scaling ($c_{\eta'} = 0.40 \pm 0.12$) [139]
ρ^0	From m_{T}-scaling($c_{\rho^0} = 1 \pm 0.3$) [139]
ϕ	From m_{T}-scaling($c_\phi = 0.25 \pm 0.08$) [139]
Ω^-	Phys.Lett. B712 (2012) 309-318[142]
Ξ^-	Phys.Lett. B712 (2012) 309-318[142]
Λ^0	J.Phys.Conf.Ser. 446 (2013) 012055 [143]
$K_s^0(K_l^0)$	J.Phys.Conf.Ser. 446 (2013) 012055 [143]
D^0	JHEP 09 (2015) 148 [144] + 10.1007/JHEP01(2012) 128 [145]
D^+	JHEP 09 (2015) 148 [144] + 10.1007/JHEP01(2012) 128[145]
D^{*+}	JHEP 09 (2015) 148 [144] + 10.1007/JHEP01(2012) 128[145]
D_s^+	Phys.Lett. B718 (2012) 279-294 [146]
Λ_c *	FONLL shape re-weighting [122, 137]
B^+	FONLL shape re-weighting [122, 137]
B^0	FONLL shape re-weighting [122, 137]
Λ_b	FONLL shape re-weighting[122, 137]

Table 4.7: *Particle species included in the composition correction step .*

(a)

(b)

(c)

(d)
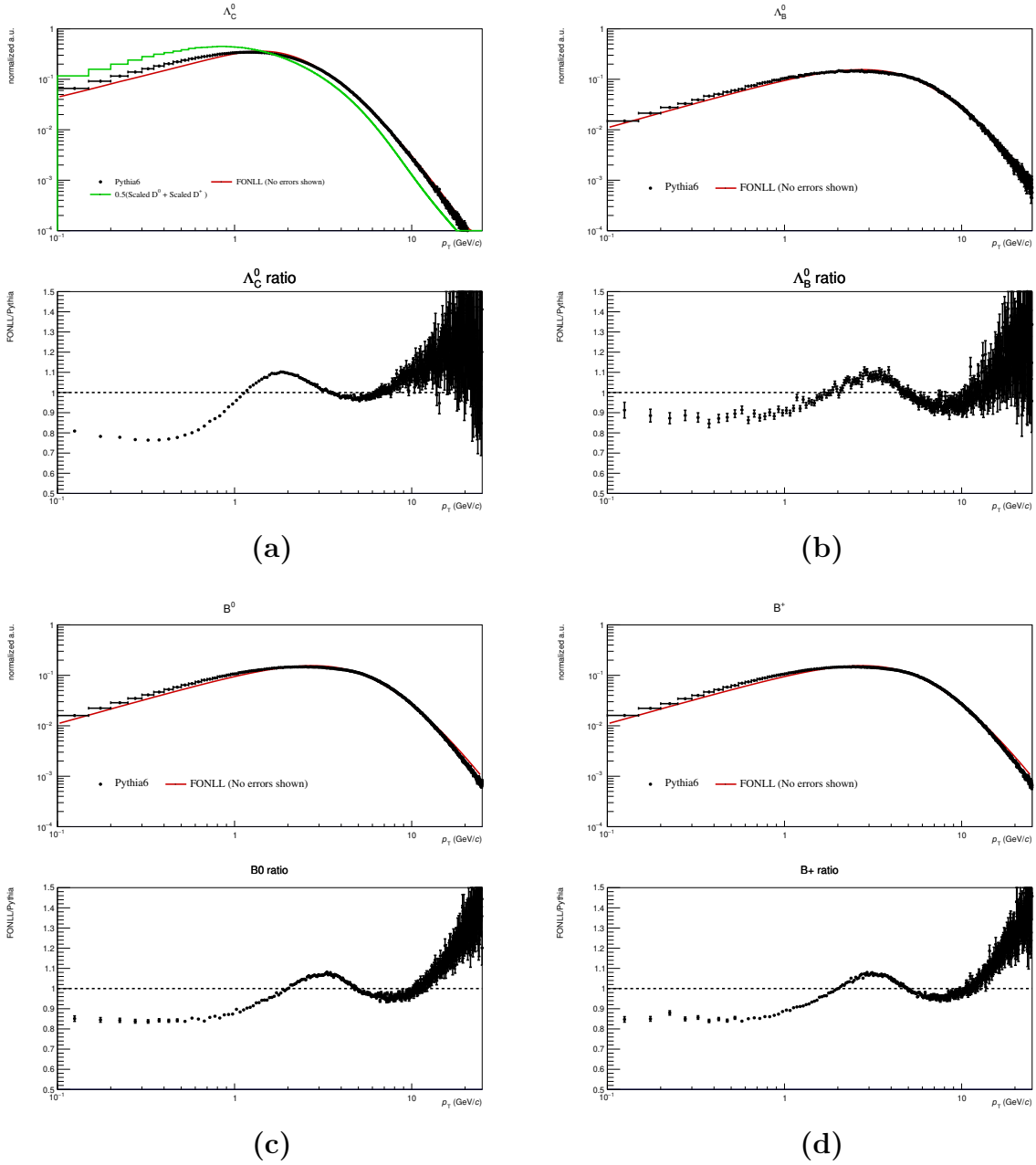
Figure   4.17:   *Shape   re-weighting   based   references   and   FONLL   over*
PYTHIA*6/*GEANT*3 ratio for* Λ_C^0, Λ_B^0, B^0, B^+ *(a-d).*
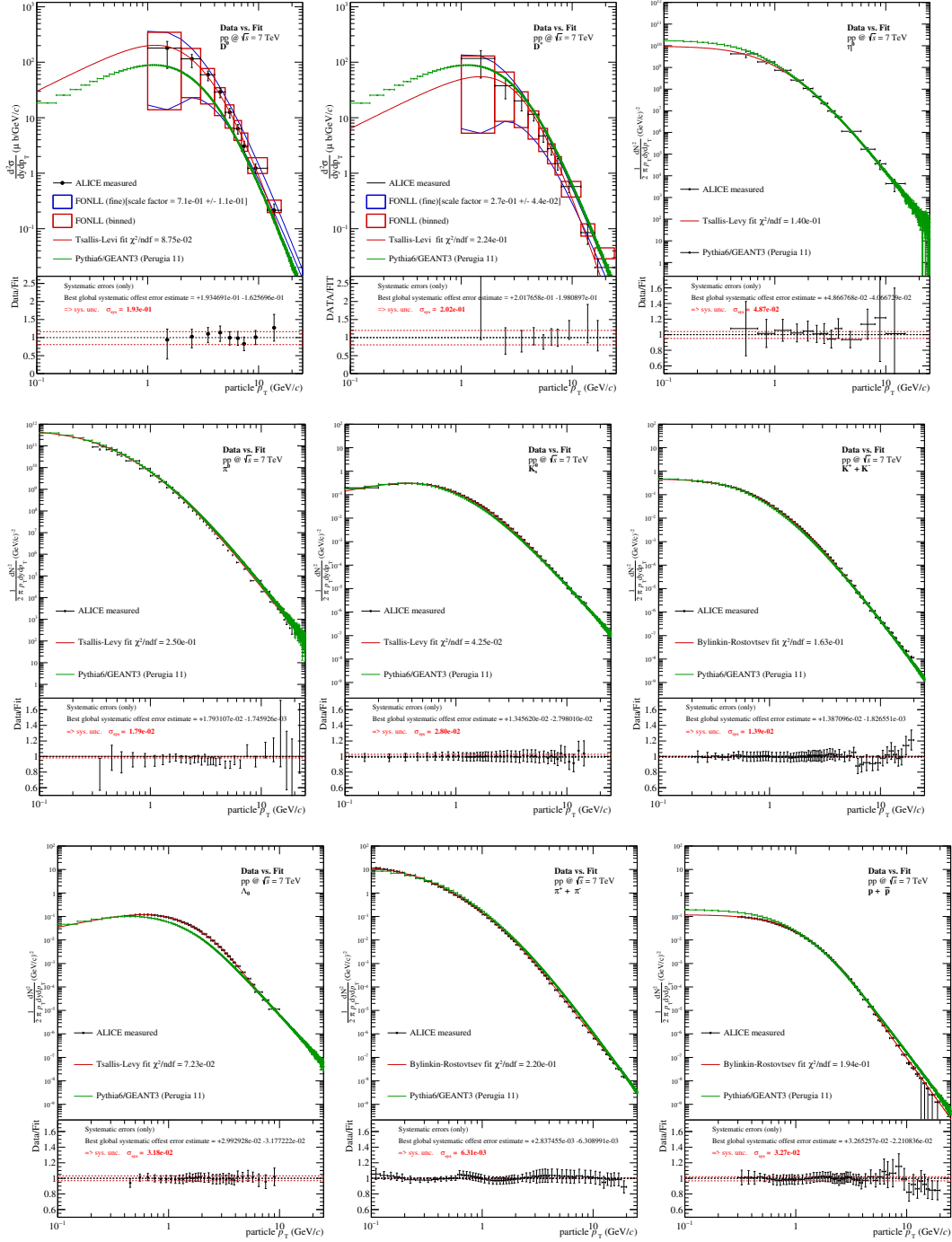
Figure 4.18: *Identified particle reference spectra (see table 4.7). The data (black points) is parametrized using a suitable parametrization (red line) and compared to the corresponding* PYTHIA*6/*GEANT*3 spectrum (green points). In case of the different D-meson spectra also the* FONLL *predictions are indicated (blue and dark red), where the global normalization factor was obtained from a fit to the data points. In the respective bottom panel the data over parametrization (fit) ratio is shown as well as the estimated normalization uncertainty (red line) obtained from the maximum allowed upward/downward variation within the systematic one-sigma uncertainties. The corresponding plots for Ω^-, Ξ^-, D_s^+ and D^{*+} can be found in the appendix A.2.*

Table 4.7 summarizes the parameters of the used interpolation functions and the resulting re-weighting factors are shown in figure 4.19. In case of a Tsallis (TF) fit the parametrization function is given by

$$A \cdot \frac{(n-1)(n-2)}{n \cdot T + m \cdot (n-2)} \cdot \left(1 + \frac{(\sqrt{m^2 + (p_{\mathrm{T}})^2} - m))}{n \cdot T}\right)^{-n} \qquad \text{with: } m \text{ fixed.} \qquad (4.8)$$

The Bylinkin-Rostovtsev(BR) parametrization is used where statistics is abundant. The function is given by

$$A_e \cdot \exp\left(-1 \cdot (\sqrt{(p_{\mathrm{T}})^2 + m^2} - m^2)/T_e\right) + A \cdot \left(\frac{1 + (p_{\mathrm{T}})^2}{T^2 \cdot n}\right)^{-n} \qquad \text{with: } m \text{ fixed.} \qquad (4.9)$$

The global m_{T}-scaling factors were taken from [139].

Particle	Fct.	A_e	T_e	m	A	T	n	χ^2/ndf	sys. unc. (%)
K_s^0	BR	1.1239	1.6838e-01	4.976e-01	3.592e-01	7.666e-01	3.091	0.0425	3
Λ^0	BR	5.185083e-02	4.667097e-01	1.115683	2.902157e-01	7.385782e-01	3.232184	0.0928	3
$\pi^{\pm}$	BR	1.35e+01	1.24e-01	1.153	1.396e-01	5.64e-01	3.04	0.22	3
$K^{\pm}$	BR	3.604e-01	1.738e-01	4.937e-01	1.146e-01	7.612e-01	3.065	0.163	3
$p^{\pm}$	BR	6.286e-03	5.204e-01	9.383e-01	1.131e-01	6.5476e-01	3.268e+00	0.194	3
Ω^-	BR	1.299e-03	1.392e-01	1.67245	0.0011	1.36957	4.51088	0.0606	8
Ξ^-	BR	2.493e-03	5.328e-01	1.322e	2.117e-02	9.537e-01	3.537	0.018	5
D_0	BR	2.0e+02	7.867e-01	1.865e	1.427e-01	2.6194	2.885	0.022	16
D^+	BR	6.293	1.337	1.865	2.0e+02	1.240	2.803	0.096	16
D^{*+}	BR	1.115	7.169e-01	2.010	1.897	4.635e	4.634e	0.0765	12
D_s^+	TF	n.a.	n.a.	1.9685	5.60e-01	5.60e-01	7.378	0.0391	36
π^0	TF	n.a.	n.a.	1.350e-01	2.48	0.14	6.9	0.25	3
η^0	TF	n.a.	n.a.	5.479e-01	2.e-01	0.239	7.17	0.14	5
MT scaled references									
ρ^0	m_{T}	n.a	n.a.	n.a.	n.a.	n.a.	n.a.	n.a.	30
η'	m_{T}	n.a	n.a.	n.a.	n.a.	n.a.	n.a.	n.a.	30
ϕ^0	m_{T}	n.a	n.a.	n.a.	n.a.	n.a.	n.a.	n.a.	30
ω^0	m_{T}	n.a	n.a.	n.a.	n.a.	n.a.	n.a.	n.a.	30
FONLL based p_{T} re-weighing									
B^+	SR	n.a.	n.a.	n.a.	n.a.	n.a.	n.a.	n.a.	30
B^0	SR	n.a.	n.a.	n.a.	n.a.	n.a.	n.a.	n.a.	30
λ_B	SR	n.a.	n.a.	n.a.	n.a.	n.a.	n.a.	n.a.	30
λ_C	SR	n.a.	n.a.	n.a.	n.a.	n.a.	n.a.	n.a.	30

Table 4.8: *Fit parameters of data parameterizations, extracted maximum global systematic uncertainty*

The weighting factors are applied as filling weight for a given impact parameter significance value. Technically this correction approach is only exact in the case of unlimited available statistics however as the impact parameter distributions are mostly defined by abundant particles species the effect of limited statistics is expected to be low. To verify this assumption the impact of statistical artefacts as e.g. single bin outliers have also been assessed (See listing 1).

While the previous correction addresses the imperfections of the event generation also the detector simulation needs to be corrected for residual detector misalignment and resulting differences in the impact parameter resolution between data and Monte Carlo. The approach used in the following first subtracts the true impact parameter d_0^{True} calculated with the Monte Carlo particle parameters and the Monte Carlo primary vertex from the previously estimated impact parameter value and then smears the remaining
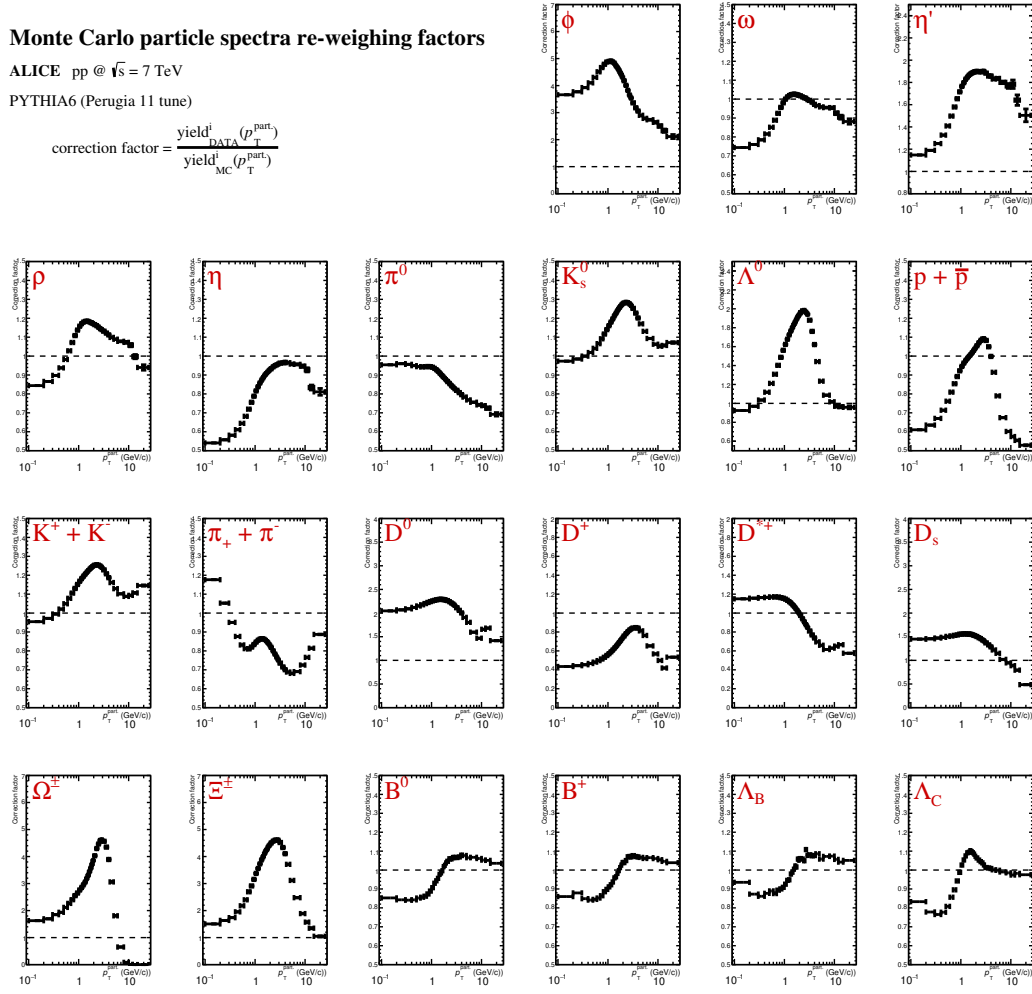
Figure 4.19: p_T^{Track} *dependent Monte Carlo (*PYTHIA*6/*GEANT*3) correction factors in the momentum region* 0.1 GeV/c $\leq$ p_T^{Track} $\leq$ 25GeV/c *(This Work)*

detector-resolution part with the smearing factor f:

$$d_0^{\text{smeard}} = (d_0^{\text{Orig.}} - d_0^{\text{MC}}) \cdot f + d_0^{\text{MC}} + \delta(d_0) \qquad (4.10)$$

The systematic uncertainties as shown in table 4.8 are defined as the maximum possible total variation within the 1σ systematic uncertainties of a given measured reference. This choice accounts for relative normalization differences between different particle species that would directly alter the shapes of the final impact parameter significance distributions. In case of spectra obtained from m_T-scaling the 30% uncertainty of the scaling factors is assigned. For the factors obtained from FONLL shape re-weighting, a global conservative estimate of 30% was assigned as well.

4.8.3   Impact parameter mean-width correction

$\delta(d_0)$ and f are iteratively determined by comparing the inclusive two-dimensional impact parameter distributions of tracks satisfying the analysis cuts using Gaussian fits to the peaks of the distributions and the inclusive signed impact parameter significance distributions.

In the later case only the negative significance range and the positive range up to 1σ has been used in the comparison as the range should be dominated by detector effects. Figure 4.20 shows the data/simulation ratio for different smearing factors (1.08, 1.113 and 1.134). It has been found that a good agreement can be achieved by choosing
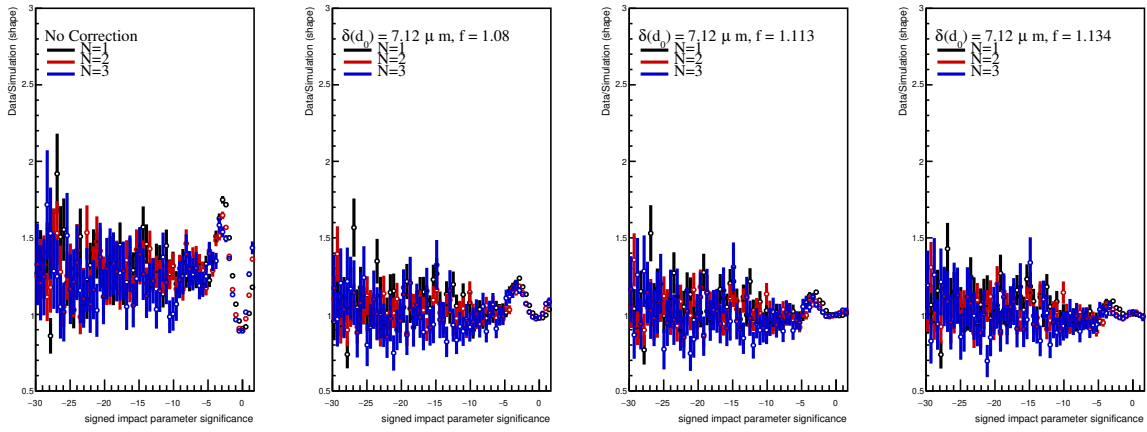
Figure 4.20: *Residual differences in the final discriminator distribution shapes for different smearing parameters i.e (left to right) no smearing or mean shift, $\delta(d_0) = 7.12 \pm 0.01/ f = 1.08 \pm 0.005$, $\delta(d_0) = 7.12 \pm 0.01/ f = 1.113 \pm 0.005$, $\delta(d_0) = 7.12 \pm 0.01/ f = 1.134 \pm 0.007$.*

$$\delta(d_0) = 7.12 \pm 0.01 \ \mu\text{m} \tag{4.11}$$

$$f = 1.134 \pm 0.005 \tag{4.12}$$

4.8.3.1   Systematic uncertainty estimation

The residual shape uncertainty is assessed by determining the relative difference of measured distributions in data and fully re-weighted and corrected simulation. For the used set of correction factors the relative uncertainty of 2%-5% was found for the negative tail region and the slope region close to the peak. These additional uncertainties are also accounted for in the template fit procedure.

4.8.4 Combined template systematics

The combined template systematic uncertainties are composed of the weight factor uncertainties scaled by their relative contribution to the templates and the maximum weight, more precisely by the maximum change due to the application of a given weight. With c being the composition correction factor, $\mathcal{R}_i^j$ being the relative particle species contribution to the template, $\sigma_j^{\text{sys.}}$ the estimated systematic uncertainty on the weighting factor, and $\sigma_{d_0}^{\text{sys.}}$ the residual shape uncertainty one can define the total systematic uncertainty to be:

$$(\sigma_{i=b,c,\text{light}}^{\text{sys.tot.}})^2 = (\sum_{j \in \pi^0, \eta^0, \ldots} \mathcal{R}_i^j(p_{\text{T}}^{\text{ch.jet}}) \cdot |1. - \max_{p_{\text{T}}^{\text{particle}} > 1\text{GeV/c}} c(p_{\text{T}}^{\text{particle}})| \cdot \sigma_j^{\text{sys.}})^2 + (\sigma_{d_0}^{\text{sys.}})^2 \qquad (4.13)$$

Using the maximum possible weight in the evaluation is a conservative estimate. It
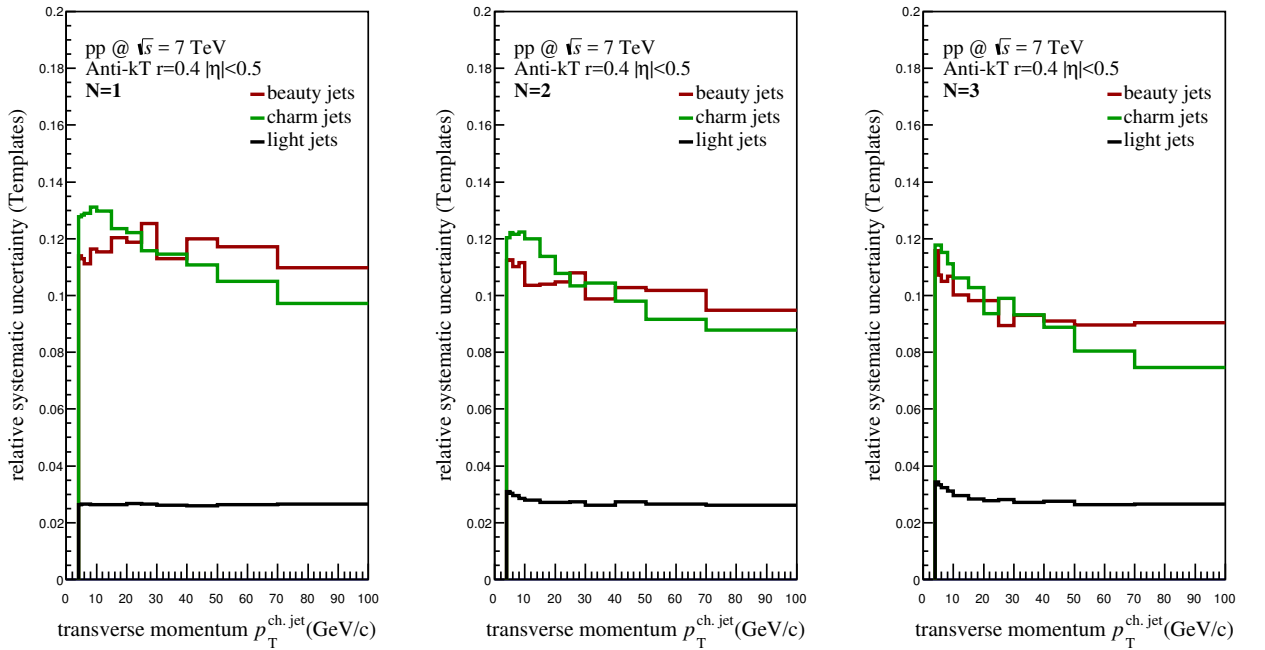
Figure 4.21: *Momentum dependent beauty-, charm- and light flavour signed impact parameter template uncertainties for $N = 1, 2, 3$.*

might be argued that the momentum range of the evaluation range could be constraint to a lower upper value for a less conservative estimate.

Figure 4.22 shows the $p_{\text{T}}^{ch,jet}$-dependent relative weight contribution for all corrected particle species that allows to estimate the total template uncertainty given the particle specific systematic uncertainty as listed in table 4.8 based on formula 4.13. The resulting inclusive template uncertainties for the different light- ,charm- and beauty templates are shown in figure 4.21.

(a) *N=1 (light jets)*   **(b)** *N=2 (light jets)*   **(c)** *N=3 (light jets)*

(d) *N=1 (charm jets)*   **(e)** *N=2 (charm jets)*   **(f)** *N=3 (charm jets)*

(g) *N=1 (beauty jets)*   **(h)** *N=2 (beauty jets)*   **(i)** *N=3 (beauty jets)*
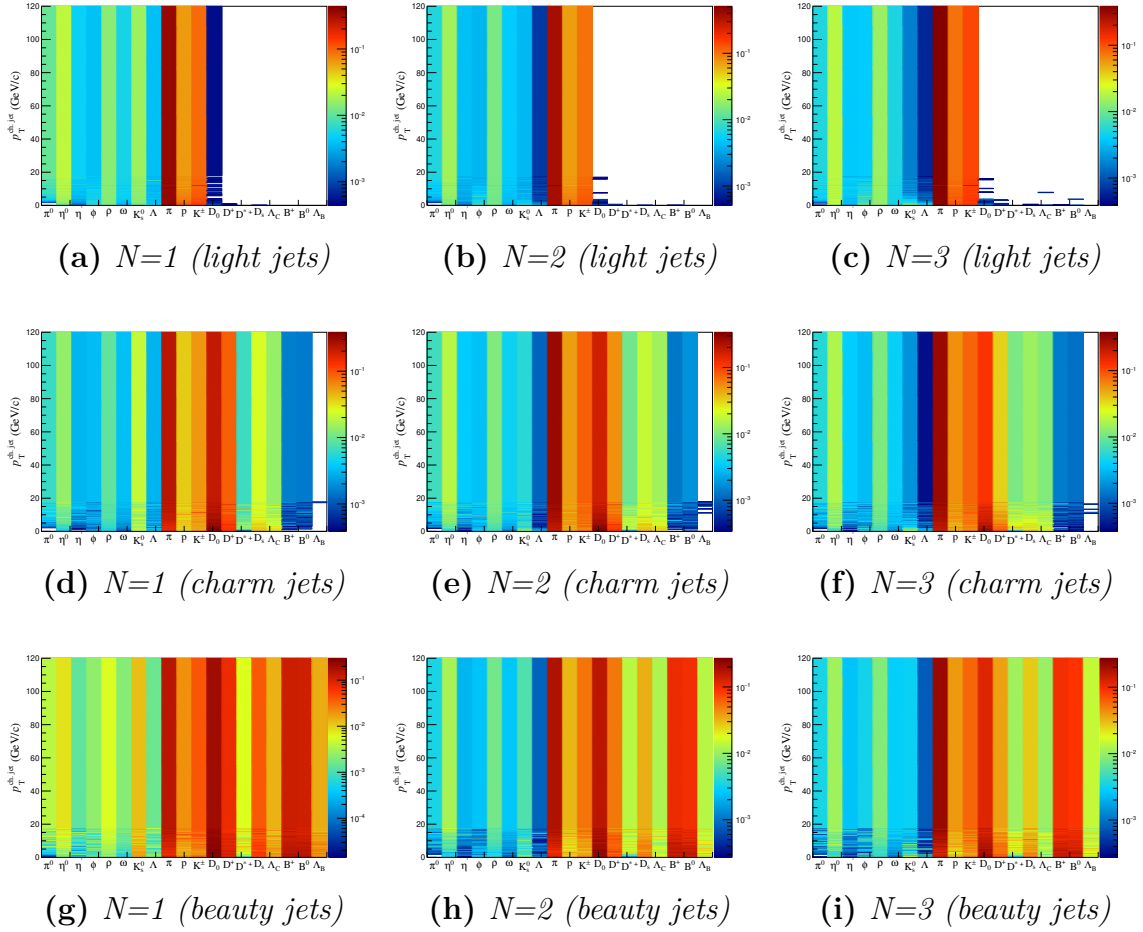
Figure 4.22: $p_{\mathrm{T}}^{ch,jet}$ *dependent relative particle contribution (normalized in $p_{\mathrm{T}}^{ch.jet}$-slices) to the $N = 1, 2, 3$ light-, charm- and beauty jet templates.*

The systematic uncertainties for the light jet templates are found to be of the order of $\mathcal{O}(\sigma_{lf}) = 3\%$, while the charm- and beauty jet template uncertainties are driven by the large uncertainties of the D and B mesons an are of the order $\mathcal{O}(\sigma_{b,c}) = 10\%$.

4.8.5 Template distributions

Before the decision on what input sample should be used for the template creation can be made, it is advised to test the differences in the template shapes for a pure MB simulation and the Jet-Jet figures 4.23,4.24 and 4.25 show the comparison for $N = 1$, $N = 2$ and $N = 3$ in four jet momentum bins. The templates show good agreement despite the differences in throughout the full momentum range. Due to the higher statistics available from the Jet-Jet data sample it is chosen over the Merged sample that is statistically limited at low jet momenta where it is dominantly defined by the contribution from the minimum bias MC.
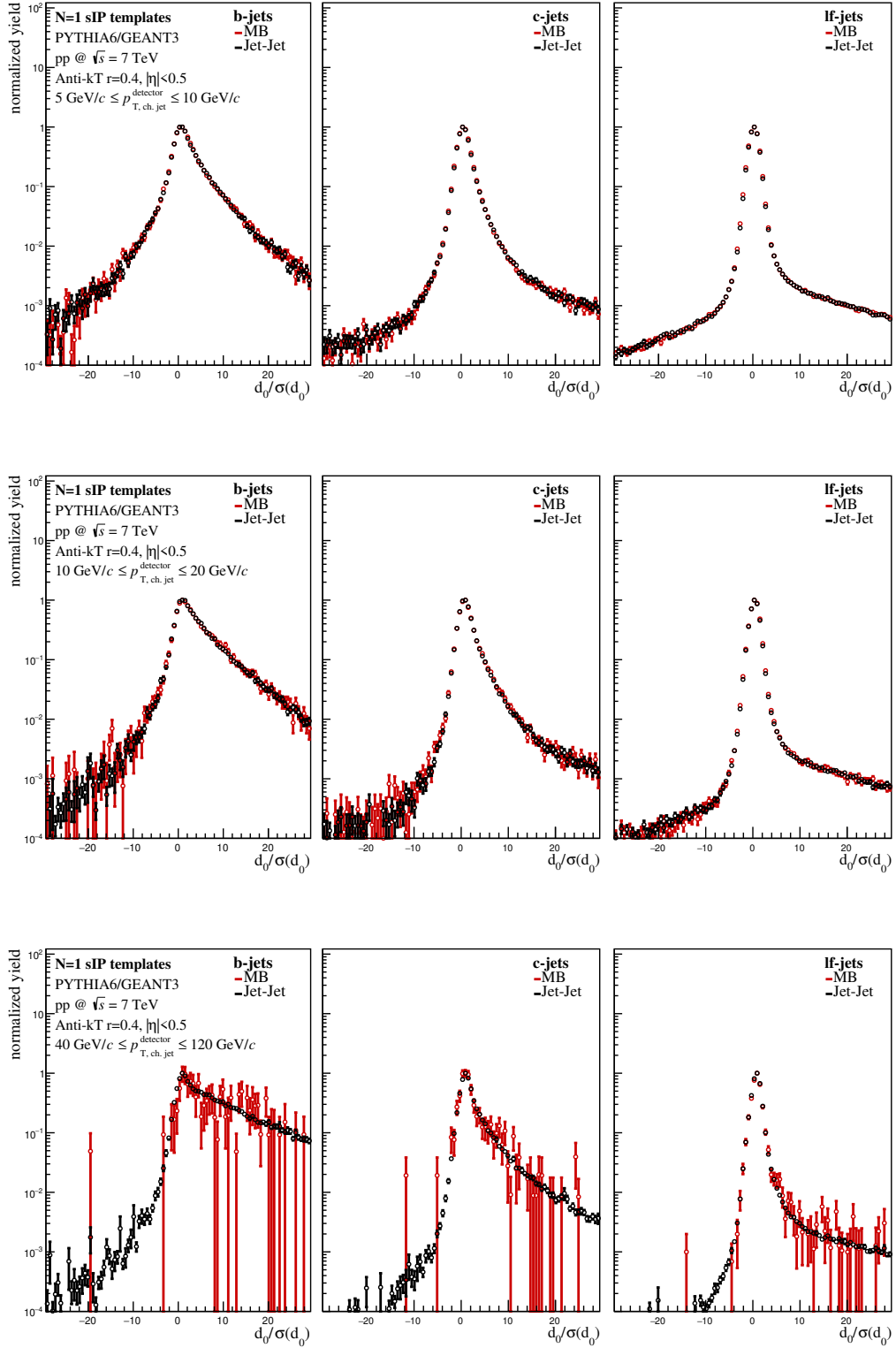
Figure 4.23: $N = 1$ *Signed impact parameter distribution template comparison LHC14j4b-f (minimum bias MC) and LHC15g6d/e (Jet-Jet MC)*
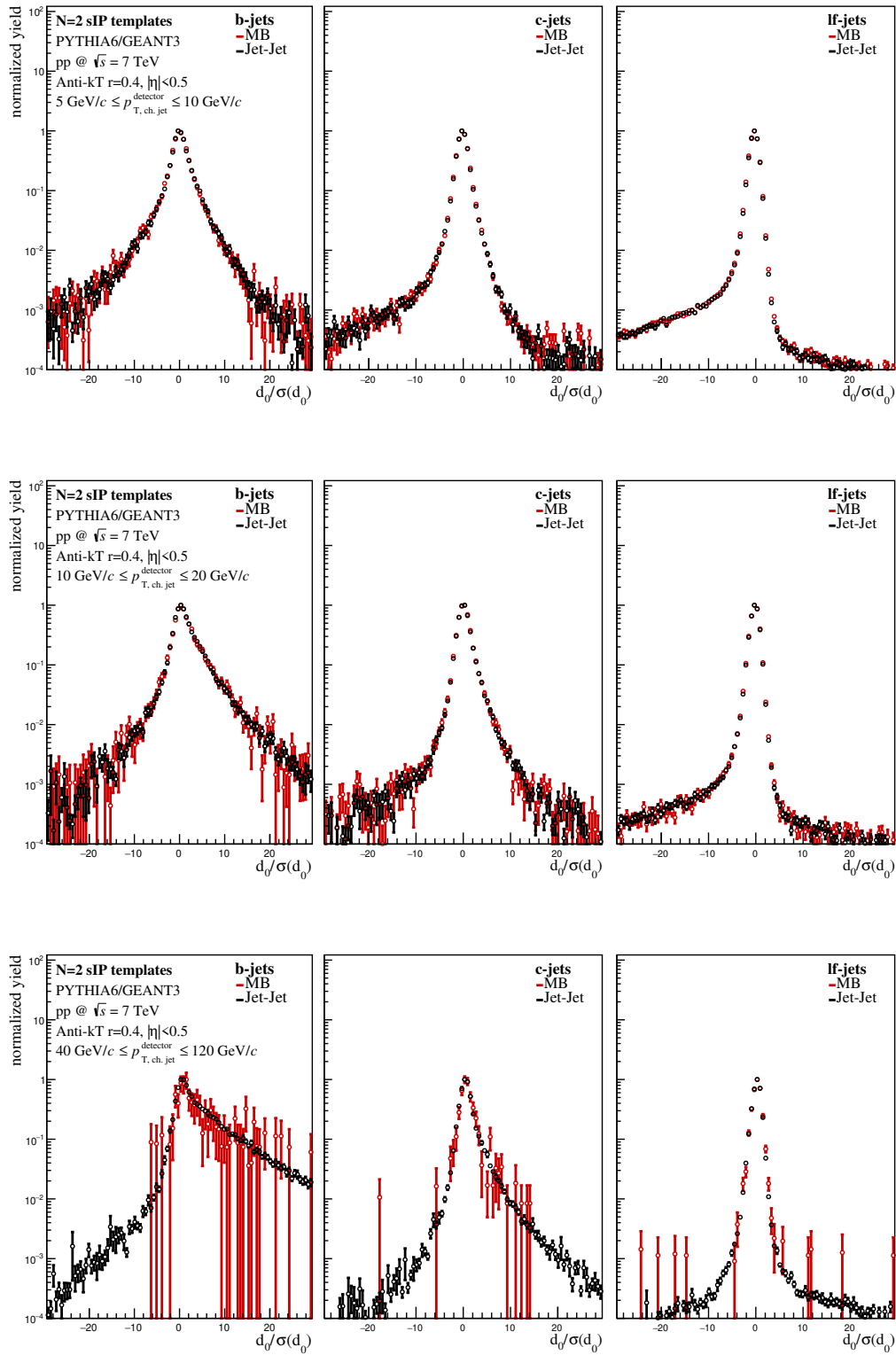
Figure 4.24: *N = 2 Signed impact parameter distribution template comparison LHC14j4b-f (minimum bias MC) and LHC15g6d/e (Jet-Jet MC)*
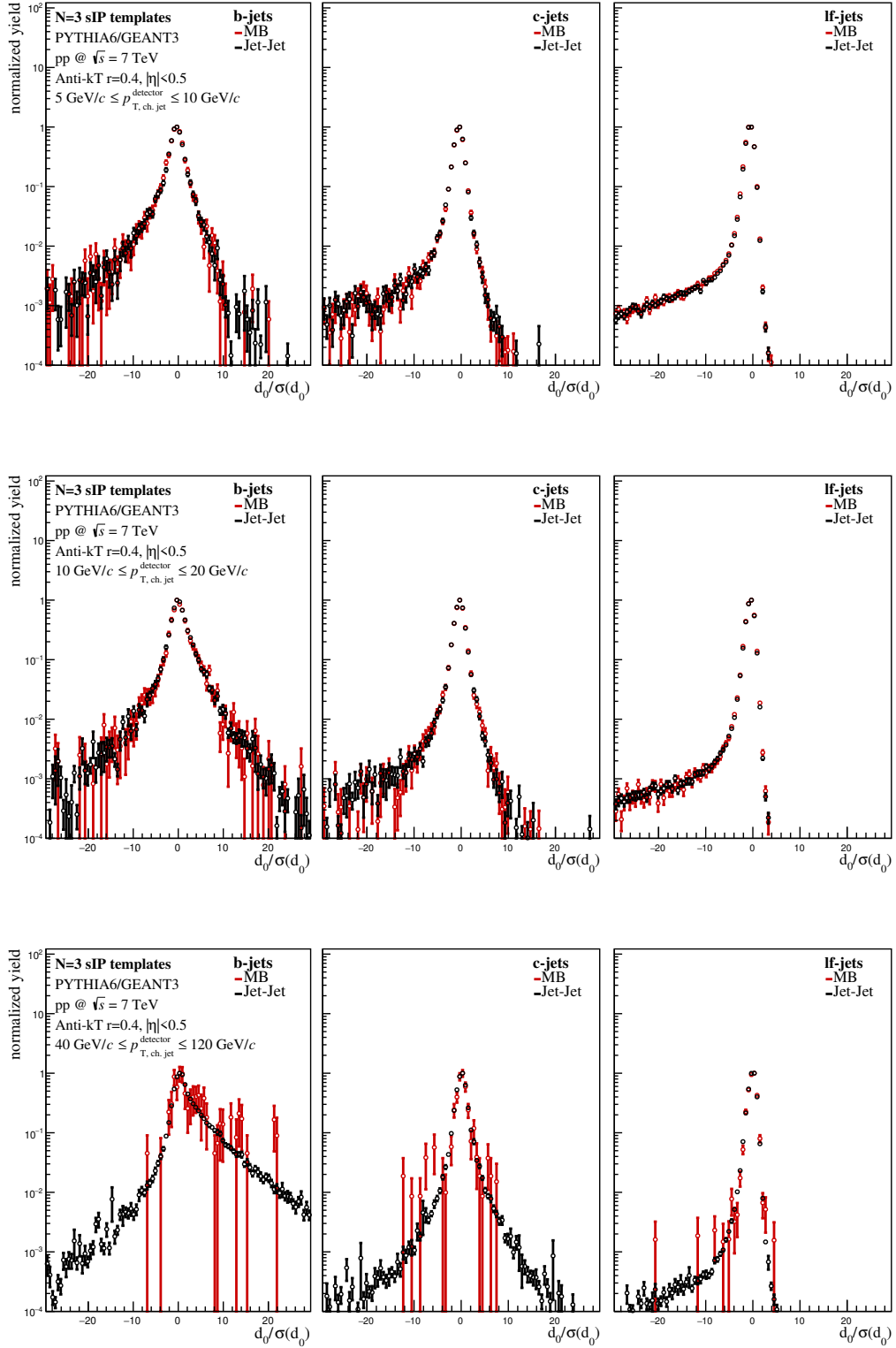
Figure 4.25: $N = 3$ *Signed impact parameter distribution template comparison LHC14j4b-f (minimum bias MC) and LHC15g6d/e (Jet-Jet MC)*

4.9   Template fit procedure

The template fit procedure is implemented using the Toolkit for Data Modelling with ROOT(RooFit) [147] providing interface classes for object-oriented data modelling. Each of the three templates for a given jet momentum bin (for a fixed N) is normalized and converted into a

RooFit::RooHistPdf that corresponds to a normalized probability density function sampled from the original histograms. The three PDFs are then combined into a

RooFit::RooAddPdf that is fitted to the data specifying the SumW2Error(1) option. The corresponding model is given by:

$$Model = f_b \cdot \text{b-template} + f_c \cdot \text{c-template} + f_{lf} \cdot \text{lf-template}. \qquad (4.14)$$

Here b,c and lf stand for beauty, charm and light flavour, where the latter includes up-, down-, strange- and gluon-jets.

The fit invokes the MINUIT [148] commands MIGRAD, HESSE and MINOS to find the best set of parameters $\{f_b, f_c, f_{lf}\}$ minimizing the standard χ^2 value of the model with respect to the measured distribution. Empty bins in one or more templates are excluded from the active fit region. The fit is performed for each momentum bin and for each of the $N = 1, 2, 3$ distribution. The uncertainty of the measured distribution is fully considered in the minimization while the templates uncertainties are not. The uncertainties, both due to limited statistics as well as systematic uncertainties are included by repeating the fit multiple times ($n_{\text{iter}} = 30$ times randomly varying the template bin contents within their 1 σ uncertainty range. The differences of the bin content of the fit results are later used as an additional systematic uncertainty accounting for the template finite statistics. The variations are also repeated with and without the systematic uncertainties to allow a later disentanglement of both contributions.

4.9.1   Outlier removal schemes

As the template uncertainties are addressed using the discussed multi-iteration procedure, single bins that are filled with large weight entries stemming from rare particles might introduce a pull to the template fit. In the ideal case of unlimited statistics the re-weighting procedure would be exact however in the finite statistics case these outliers cannot be fully excluded.

The possible impact of these outliers are explored using a multistage outlier removal scheme.

Therefore the impact of each bin onto the fit result can is calculated by removing the respective bin from the fit range and repeating the fit. The extracted change (bin impact)

$$b_{imp} = \frac{\text{b-fraction}_{\text{full}} - \text{b-fraction}_{\text{reduced}}}{\sigma} \tag{4.15}$$

serves as a measure of the impact of each bin (b_{imp}).

Two requirements can be formulated based on the fact that the ideal distributions should be continuous with well defined single peak around zero and more than exponentially falling flanks.

1. Bins close to the peak should have the largest bin impact (lowest uncertainty).

2. Neighbouring bins (sufficient fine binning) should have comparable bin impact (continuous distribution).

As it cannot be ruled out that these criteria are broken by some bins either by having globally or locally large bin impact values affected bins are removed if the bin impact is globally larger than a given threshold value (optimization strategy 1) or if the bins impact is locally significant larger than the impact of its neighbours (optimization strategy 2). The local deviation of the bin impact is therefore compared to the a third-order median filtered bin impact distribution, Where each bin content is replaced by the median value of itself and its two neighbours, omitting the lowest and the highest bin of the distribution. Each excluded bin is removed from the active fit range and the fit is repeated a final time. Algorithm 1 shows the implementation of the outlier removal scheme. For the default result obtained in this analysis no optimization is used. In section 4.13.3 the impact of the outlier removal is discussed and found to be negligible.

Algorithm 1 Multi-stage template fit with outlier reduction in pseudo-code representation

---

1: **procedure** DOTEMPLATEFIT()
2:      *data, templates* ← ReadInputs()
3:      $b_{\text{Fraction}}^{\text{ref.}}$ ← RunTemplateFit(data,templates)
4:
5:      **for** each bin i in data **do**
6:          $\{\text{data}^{\text{tmp}}\} = \{\text{data}\} - \{\text{data}\}_i$
7:          $b_{\text{Fraction}}^{\text{mod.}}$ ← RunTemplateFit(data$^{\text{tmp}}$,templates)
8:          binImpact$_i$ ← $|b_{\text{Fraction}}^{\text{ref.}} - b_{\text{Fraction}}^{\text{mod.}}|/Error(|b_{\text{Fraction}}^{\text{ref.}} - b_{\text{Fraction}}^{\text{mod.}}|)$
9:
10:     $\{\text{medianImpact}_i\}$ ← getThirdOrderMedianFilter($\{\text{binImpact}_i \}$)
11:     **for** each bin i in data **do**
12:         **if** i. (binImpact$_i$ >5) **then**
13:             $\{\text{data}^{\text{clean}}\} = \{\text{data}\} - \{\text{data}\}_i$
14:         **if** ii. (binImpact$_i$ >5) **OR** (binImpact$_i$ /medianImpact$_i$ >3) **then**
15:             $\{\text{data}^{\text{clean}}\} = \{\text{data}\} - \{\text{data}\}_i$
16:
17:     $b_{\text{Fraction}}^{\text{RooFit}}$ ← RunTemplateFit(data$^{\text{clean}}$,templates)

4.9.1.1 Template fit results

The fine binned distributions are moderately re-binned corresponding to a new bin spacing of $\delta x = 0.24\sigma$ to remove low-statistics bins impacting the template fit while preserving the global shape. Figure 4.27 shows the results of the template fit procedure for the default (no optimization) strategy. The fitted model, shown in orange, gives a reasonable good description of the data points. In the highest momentum bin the impact of low statistics is clearly visible. Still the resulting fractions especially for the signal (beauty-jets) is remarkably stable with respect to fluctuations. As charm- and light- jet templates are quite similar the low contribution of charm-jets in the highest momentum bin can be explained to be an artefact of this similarity and the influence of the much lower statistics in the templates for charm- than for light jets. The impact of the template statistics is discussed in section 4.10 with respect to the beauty-jet fraction but is equally valid for the charm contribution. In figure 4.26 the comparison
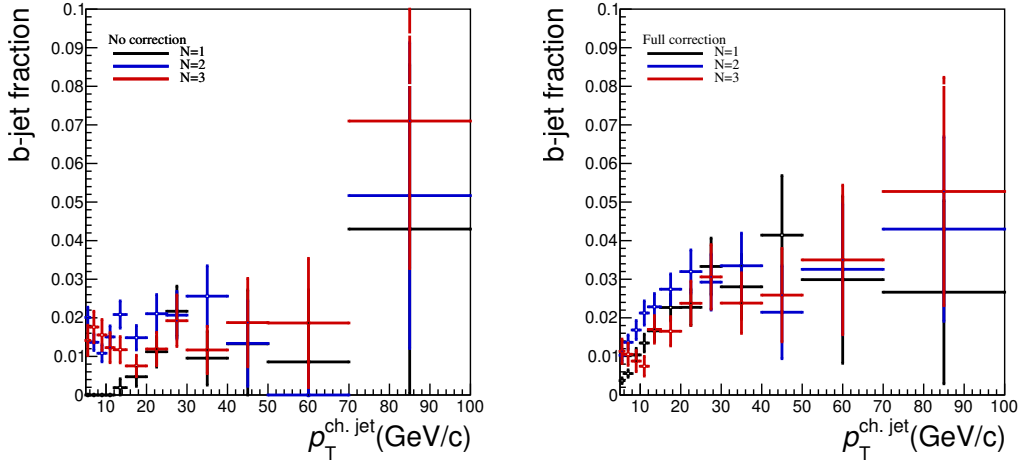
Figure 4.26: *Comparison of the template fit raw results using uncorrected (left) and corrected(right) Monte Carlo templates.*

of the template fit results with and without corrected Monte Carlo templates are shown. Without the correction procedure the template fit is unable to extract any smooth signal fraction vs. momentum relation as the fit fails converge for most of the momentum bins.
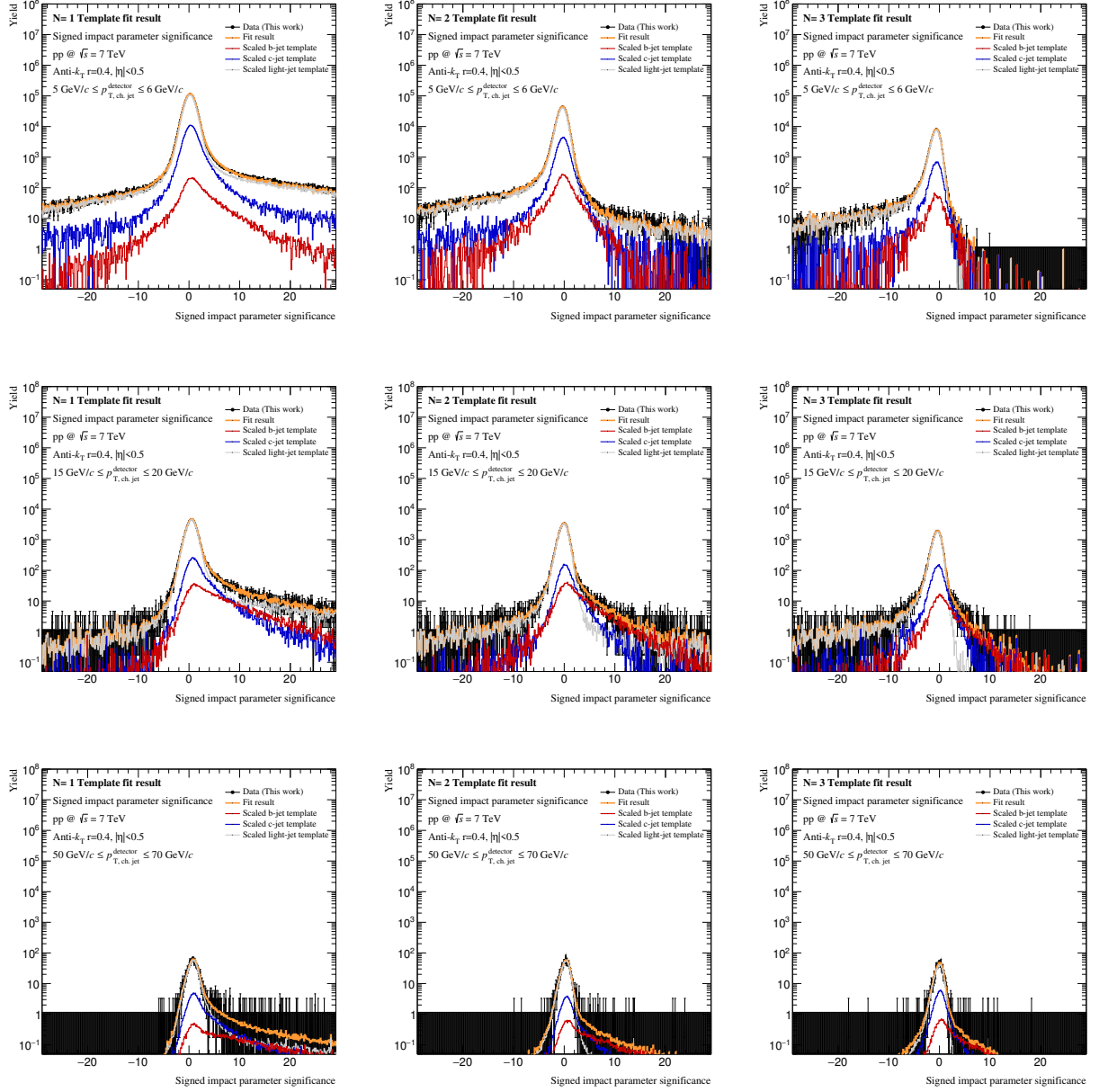
Figure 4.27: $N = 1$(left), $N = 2$(centre), $N = 3$ (right) template fit results for low (5 GeV/c $\leq$ 6 GeV/c) intermediate (15 GeV/c $\leq$ 20 GeV/c) and high (50 GeV/c $\leq$ 70 GeV/c) transverse jet momenta. The full set of plots can be found in the appendix A.3.

4.10   Detector level beauty jet spectrum

The BLUE (Best Linear Unbiased Estimator)[149][150] method is a technique that allows the approximate combination different measurements without the knowledge of the underlying individual likelihood functions.

Let N be the number of measurements X_i of an observable X (i.e. the selection efficiency corrected beauty jet fraction in our case) and C be the associated covariance matrix. We define the individual weights to be given by

$$\vec{w} = \frac{C^{-1}\vec{u}}{\vec{u}^T C \vec{u}} \qquad \text{with } u_j = 1 \quad \forall j \in (1, N) \tag{4.16}$$

The combined estimate is then given by

$$X = \sum_{i=1}^{N} w_i X_i \pm \vec{w}^T C \vec{w} \tag{4.17}$$

In contrast to the general weighted average some w_i may be negative depending on the individual correlations. Negative weights indicate a strong correlation of the individual measurements.

The BLUE combinations for the $N = 1$, $N = 2$, $N = 3$ fractions are calculated for all of the 30 iterations in a bin-wise procedure. Here the fractions are first corrected for the relative differences in the jet selection efficiencies for b-jets and non-b-jets.

$$P_{\text{b-jet,N=1,2,3}}^{corr.} = P_{\text{b-jet,N=1,2,3}}^{\text{Fit}} \frac{\epsilon_{\text{N=1,2,3}}^{\text{b-jet}}}{\epsilon_{\text{N=1,2,3}}^{\text{nonb-jet}}} \tag{4.18}$$

Figure 4.28 shows the jet selection efficiencies for $N = 1, 2, 3$ as measured in data (left) and the jet selection efficiencies for b-jets and non-b jets (right) extracted from the PYTHIA6/GEANT3 simulation and used in the correction of the input fractions for the BLUE combination. Finally the relative upward and downward deviations from the default hypothesis (first iteration) are calculated and added as systematic uncertainties covering the impact of the template uncertainties. Finally the fraction is multiplied with the inclusive jet fraction to obtain the detector level charged beauty jet spectrum. The input fractions and the combined BLUE results are shown in figure 4.29.

The impact of the template uncertainty can be addressed using a small gedanken experiment to illustrate the problem: Let $f(x_i) = c$ be a constant data distribution, where i enumerates the bins and $s(x_i)$ the signal template distribution. σ_i is the uncertainty of bin i. Now $s(x_i)$ should be fitted to the data $f(x_i)$ using a scale parameter p. If $s(x_i)$ has high statistics it would be a normalized constant function and p can be found that $\chi^2 = \frac{(f(x_i) - s(x_i))^2}{\sigma_i} \to 1$. If $s(x_i)$ has low statistics the values of two e.g. adjacent bins can be separated within their uncertainties by a value of Δv. For the sake of the
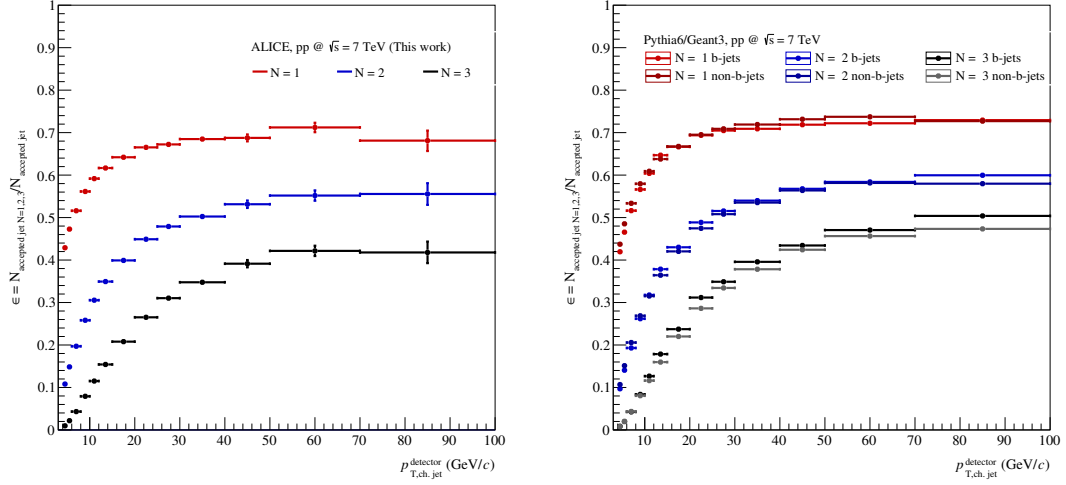
Figure 4.28: *Jet selection efficiencies for N=1,2,3 as measured in data (left) and the jet selection efficiencies for b-jets and non-b jets from MC (right)*

argument all but one bin $i = t$ have equal and ideal values. In that case $\min(\chi^2) = \frac{(\Delta v)^2}{\sigma_t}$. A minimizer will therefore fail to improve its prediction as a minimum was found and any parameter change would have no effect.

As the used Monte Carlo samples are basically reproducing minimum bias events, the $N = 3$ beauty jet template should be the most affected contribution. In terms of the resulting beauty jet fraction one therefore expects a systematic reduction with increasing N as the higher statistics of the charm- and light-jets corresponds to lower minimal χ^2 values favouring both over the b-jet template during the minimization. Figure 4.30 shows the impact of increasing statistics onto the the resulting $N = 1$, $N = 2$ and $N = 3$ fractions illustrating the anticipated effect.
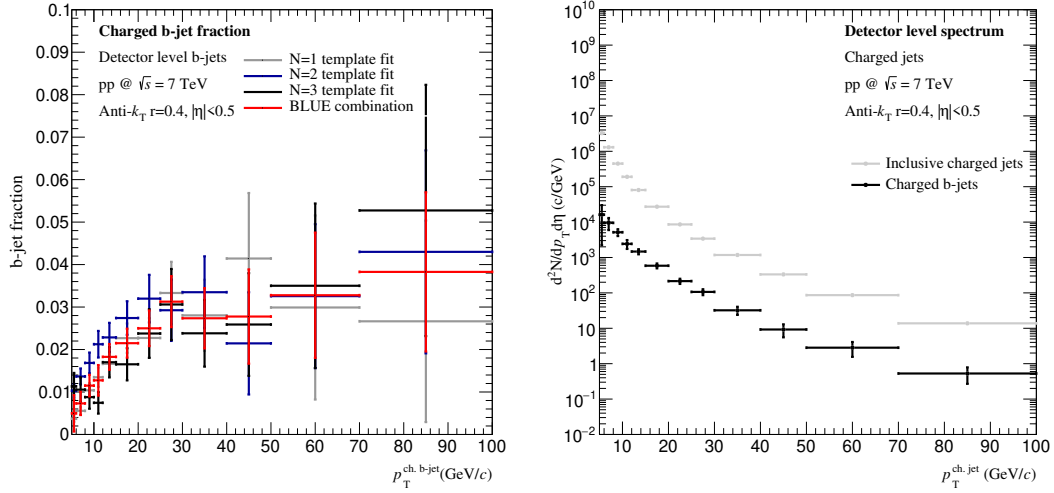
Figure 4.29:   *Measured* $N = 1, 2, 3$ *fraction and BLUE combination(left), BLUE estimate beauty jet spectrum and raw inclusive jet spectrum*
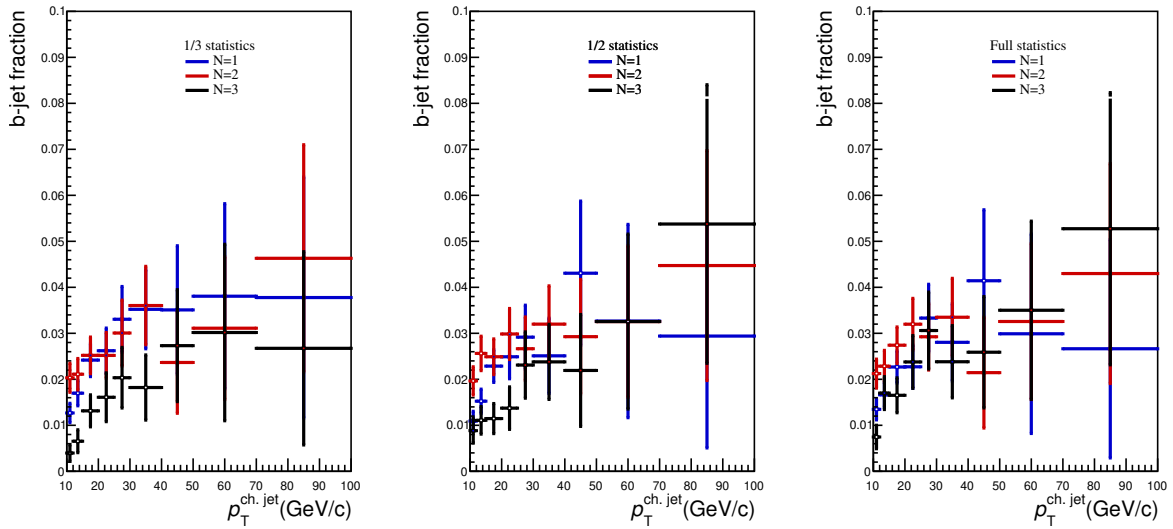
Figure 4.30: *Illustration of the impact of different template statistics on fit results. (left) 1/3, (middle) 1/2, (right) full available template statistics*

4.11 Unfolding

Unfolding in the context of jet analyses is a technique to correct the measured spectra for detector effects. Without this correction the results of different experiments and even the theory predictions would not be comparable with one-another.

Any measurement is therefore described by the convolution of the true observable with the detector response. This response function $r(a, b)$ describes the probability for a true value x_a to be measured as value x_b. In case of a simple spectrum the response can be identified with a simple matrix A_{ab} and the indices indicate the measured and unfolded bins.

$$x_b = \sum_c A_{bc} x_c \tag{4.19}$$

The response matrix A_{bc} is constructed from a combination of two PYTHIA6/ GEANT3 simulations as outlined in section 4.11.1. Due to the measurement uncertainties no exact inversion of the matrix is possible as the inversion leads to rapidly oscillating solutions. There have been several approaches to address this problem, of those we will use the Singular Value Decomposition (SVD) unfolding [151] and the Bayesian unfolding technique [152] implemented in the RooUnfold framework [153]:

Singular Value Decomposition unfolding   The singular value decomposition [151] of a general $m \times n$ matrix A is the factorization of the matrix into three matrices U,S and V where V and U are orthogonal $m \times m$ and $n \times n$ matrices and S is a $m \times n$ diagonal matrix with $S_{ii} > 0$.

$$A = U \ S \ V^T \tag{4.20}$$

The diagonal entries $S_{ii} = s_i$ are then called singular values. By swapping of rows of U and V the s_i are organised in descending order. Since the columns of V and U form normal bases of their spaces. Starting from $USV^T x = b$, rotated vectors $z \equiv V^T x$, $U^T b = d$ and $SV^T x \rightarrow s_i z_i \equiv d_i$ can be introduced. With these it follows that $x = Vz$ however this solution is highly dependent on b and d_i that are non-exact quantities but are only known with some uncertainty.

The unfolding itself can be defined as a minimization problem:

$$\sum_{i=1}^{n_b} \left(\frac{\sum_{j=1}^{n_x} A_{ij} x_j - b_i}{\delta b_i} \right)^2 \tag{4.21}$$

or more general

$$(Ax - b)^T \text{Cov}^{-1}(\text{b})(\text{Ax} - \text{b}) = \min \tag{4.22}$$

To rescale the and rotating A and b using the SVD of $\mathrm{Cov(B)^{-1} = QR^{-1}Q^T}$ one arrives at

$$(\tilde{A}x - \tilde{b})^T(\tilde{A}x - \tilde{b}) = \min \tag{4.23}$$

Now all equations have equal importance in the minimization, however small singular values are still likely to result in rapid oscillating solutions. To stabilize the solution a regularization is introduced.

$$(\tilde{A}x - \tilde{b})^T(\tilde{A}x - \tilde{b}) + \tau \cdot (Cw)^T Cw = \min \tag{4.24}$$

Where C is a matrix that defines the a-priori conditions (prior) and τ defines the relative weight of the regularisation i.e. the regularisation strength. With respect to the spectrum unfolding the matrix C holds the condition that the second derivative of the solution is small and therefore the spectrum is smooth.

Bayesian unfolding   The Bayesian unfolding technique interprets the jet spectra as probability distributions and the response matrix as set of conditional probabilities. Bayes' theorem on conditional probability is then applied to the problem in multiple steps. With the true spectrum y and the measured spectrum x one can calculate the so-called smearing matrix S and define the solution as

$$\tilde{S}_{ji} = \frac{A_{ij} \cdot y_j}{\sum_k A_{ik} y_k} \tag{4.25}$$

$$\tilde{y}_j = \sum_i S_{ji} x_i \tag{4.26}$$

As the true spectrum is not known the calculation starts using a prior, where often a flat distribution or even a interpolated measured spectrum is used. The next iteration then uses the unfolded result as the starting point.

4.11.1 The detector response matrix
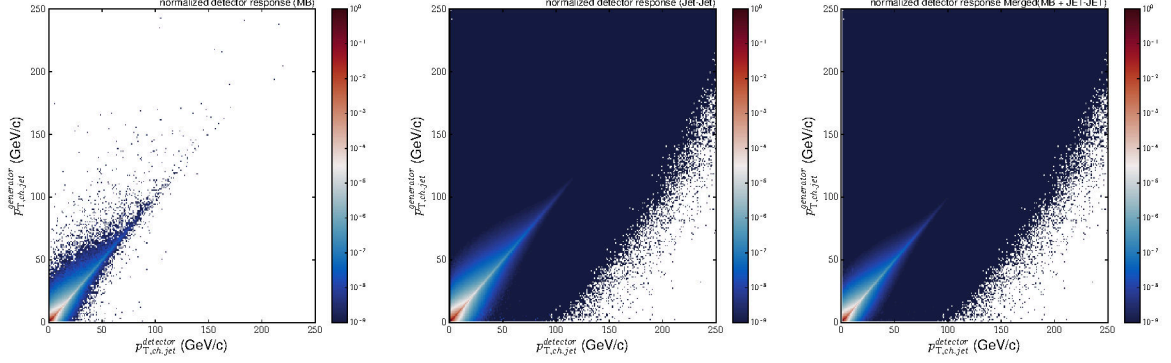
Figure 4.31: *Jet momentum response matrix for different Monte Carlo dataset choices: MB MC(left), Jet-Jet MC (center), Merged MC(right).*

The detector response matrix is constructed from the geometrically associated generator-level (same jet finder settings but on MC particle level) and detector-level jets from the merged min. bias and Jet-Jet Monte Carlo. Figure 4.31 illustrates the difference between the MB and Jet-Jet response and the good agreement between MB and the Merged response matrix. While it might not be totally evident from figures, differences are especially visible in the low momentum region below 20 GeV/c (but even extending to higher-momenta) indicating an increased probability for a given detector-level jet to come from a high momentum generator level jet. The mean jet energy shift and the jet energy resolution are shown in Figure 4.32. While the effect seems to be non-negligible,
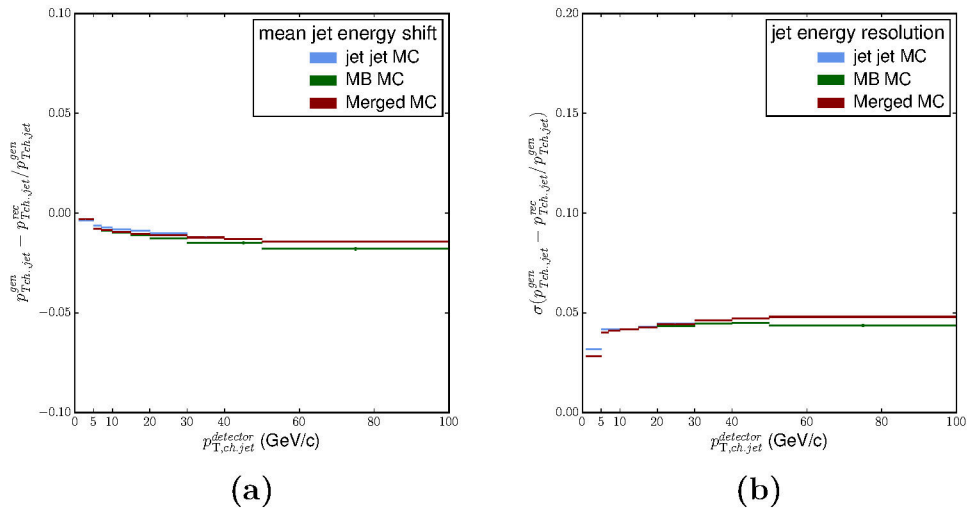
Figure 4.32: *Mean jet energy shift (left), jet energy resolution (right)*

no visible impact on the final unfolded spectrum was observed. The reason for this small impact is most likely the steeply falling shape of the associated spectra, leading to a very small contribution from high momentum generator level jets. The impact was assessed to be less than 1% for the whole jet momentum range.

4.11.2   Choice of the regularization parameter

As no exact solution for the unfolding problem exists also the choice of the unfolding parameters is subject to same limitation. For this analysis the regularisation parameter R was chosen in the following manner. As depicted in figure (4.34) the $\chi 2$ per number of degree of freedom (ndf) for the measured and the refolded spectra approaches a value around 0.78 for $R \geq 8$. This alone would imply choosing $R \geq 9$. Looking at the corresponding covariance matrices, however shows the onset of strong off-diagonal anti-correlations for $R \geq 9$ and of still large off-diagonal correlations for $R \leq 7$ (See figure 4.33).
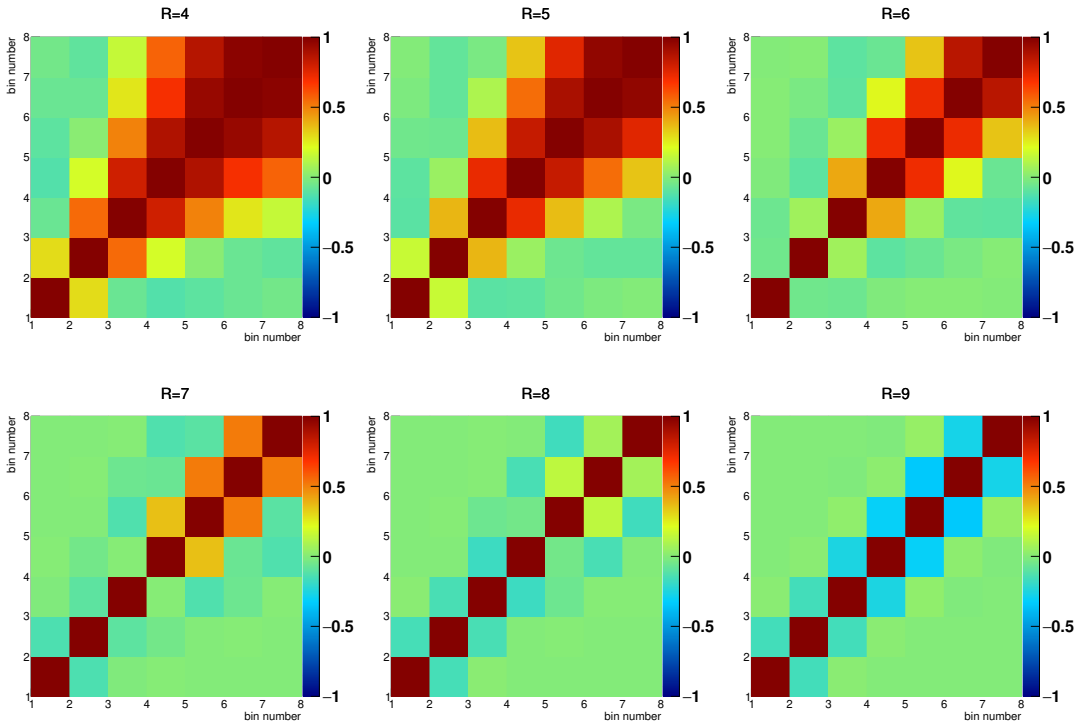
Figure 4.33: *SVD unfolding bin-wise covariance matrix for different regularisation parameters R=4 - 9.*
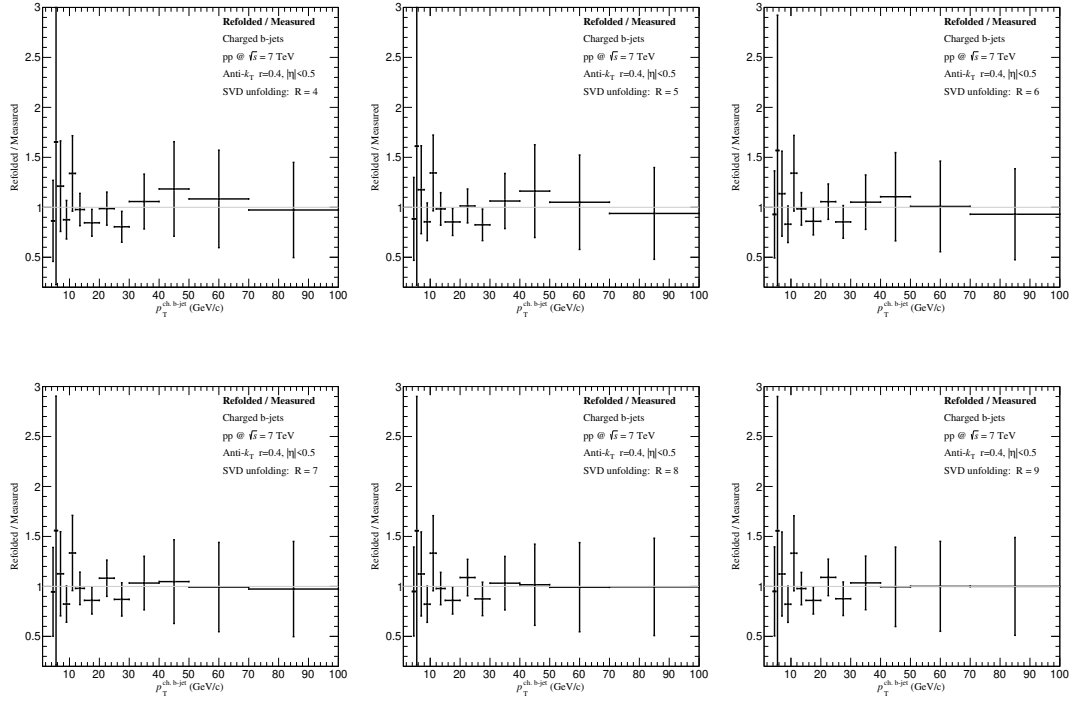
Figure 4.34: *SVD unfolding Refolded-over-Measured ratio for different regularisation parameters R = 4 - 9.*

4.11.3 Unfolding results

The binning for the unfolded spectrum is

$$\Big(\ 1, 5, 10, 15, 20, 30, 40, 50, 70, 100\Big)\,\mathrm{GeV/c} \tag{4.27}$$

Figure 4.35 shows the result of the unfolding procedure using SVD unfolding with a regularization parameter. It was chosen due to its good measured-over-refolded ratio with small off diagonal correlation coefficients and compatible d_i entries.
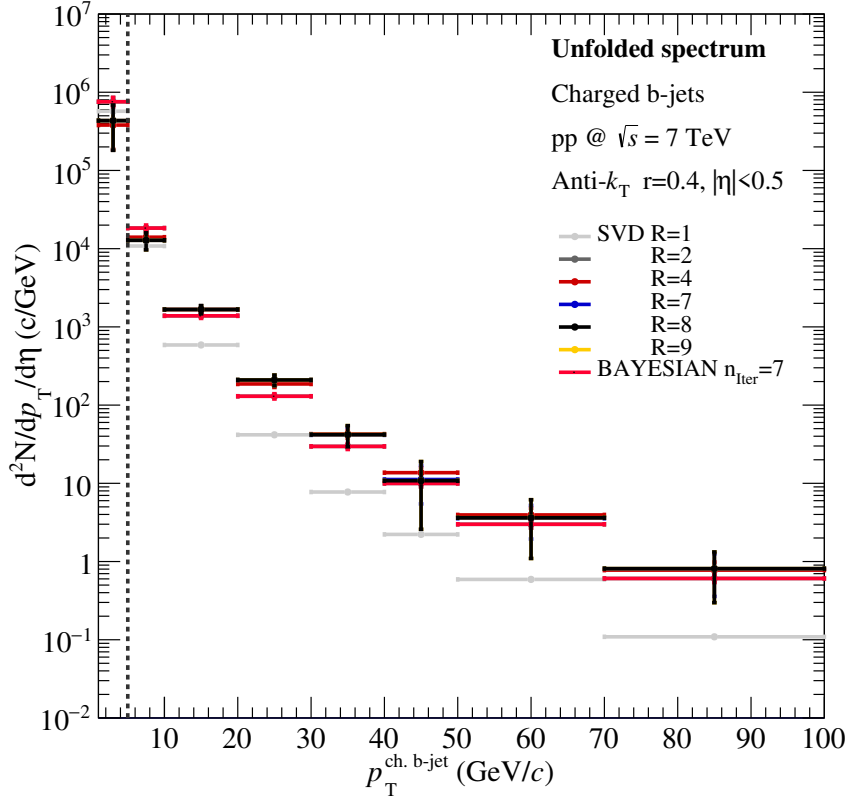
Figure 4.35: *Unfolded spectrum using SVD unfolding for various regularization parameters.*

4.11.4   Unfolding systematics

Systematic uncertainties from the unfolding method, the regularization parameter, the tracking efficiency and the steepness of the unfolding prior were evaluated. The SVD result is compared to the one obtainable by Bayesian (4 iterations) Unfolding. The Regularization parameter is varied by ± 1, the prior steepness by multiplication of the prior with $x^{\pm 0.3}$ and the tracking efficiency is reduced by 3% and the resulting systematic deviation mirrored to obtain an estimate for a increased tracking efficiency.

Figure 4.36 shows the resulting systematic uncertainties.
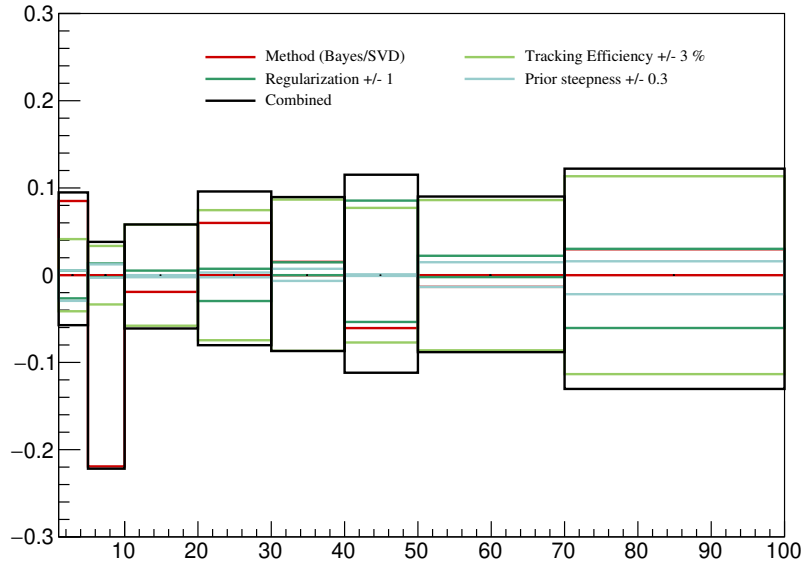
Figure 4.36: *Contributions to the systematic uncertainties of the unfolding.*

An overview of the uncertainties is given in table 4.9. It can be seen that the dominant contribution over the full momentum range originates from the track reconstruction efficiency uncertainty with the exception of the $5 - 10$ GeV/c bin where the Bayesian unfolding dominates. It may be noted that a different choice of e.g. the number of iterations for the Bayesian reference might reduce the effect. Also different methods differ in sensitivity to certain statistical configurations therefore it can be debated to what extend a comparison under the assumption that both methods should ideally give the same result captures a true methodological motivated systematic uncertainty. The resulting uncertainty is therefore seen as a conservative estimate.

All presented uncertainties are estimated by comparing the bin content of resulting unfolded spectra to the default spectrum and calculating the relative difference. All relative differences are later added quadratically to obtain the total systematic uncertainty. It should be noted that such a combination, although widely applied in many jet related analyses is only valid in the case of fully uncorrelated sources of uncertainty.

4.12 Normalization

The unfolded spectra are normalized with the measured inelastic proton-proton cross section for the MBOR trigger [57] $\sigma_{MBOR} = (62.2 \pm 2.2)$ mb.

$$\frac{d^2\sigma_{\text{b}-\text{jets}}^{\text{charged}}}{dp_{\text{T}}d\eta} = \frac{\sigma_{\text{MB}}}{N_{norm,evts.}} \frac{d^2N_{\text{b}-\text{jets}}^{\text{charged}}}{dp_{\text{T}}d\eta} \tag{4.28}$$

with

$$N_{norm,evts.} = N_{MBOR}^{|v_z|<10.} + \frac{N_{MBOR}^{|v_z|<10.}}{N_{MBOR}^{|v_z|>10.} + N_{MBOR}^{|v_z|<10.}} \cdot N_{MBOR}^{NoVtx} \qquad (4.29)$$

The normalization factor corrects for the number of min. bias events without a reconstructed vertex N_{MBOR}^{NoVtx} within the accepted vertex z-position range and the corresponding event fraction was found to be $c_{vtx.} = N_{evts.}/N_{norm,evts} = 0.859$.

4.13 Final spectrum
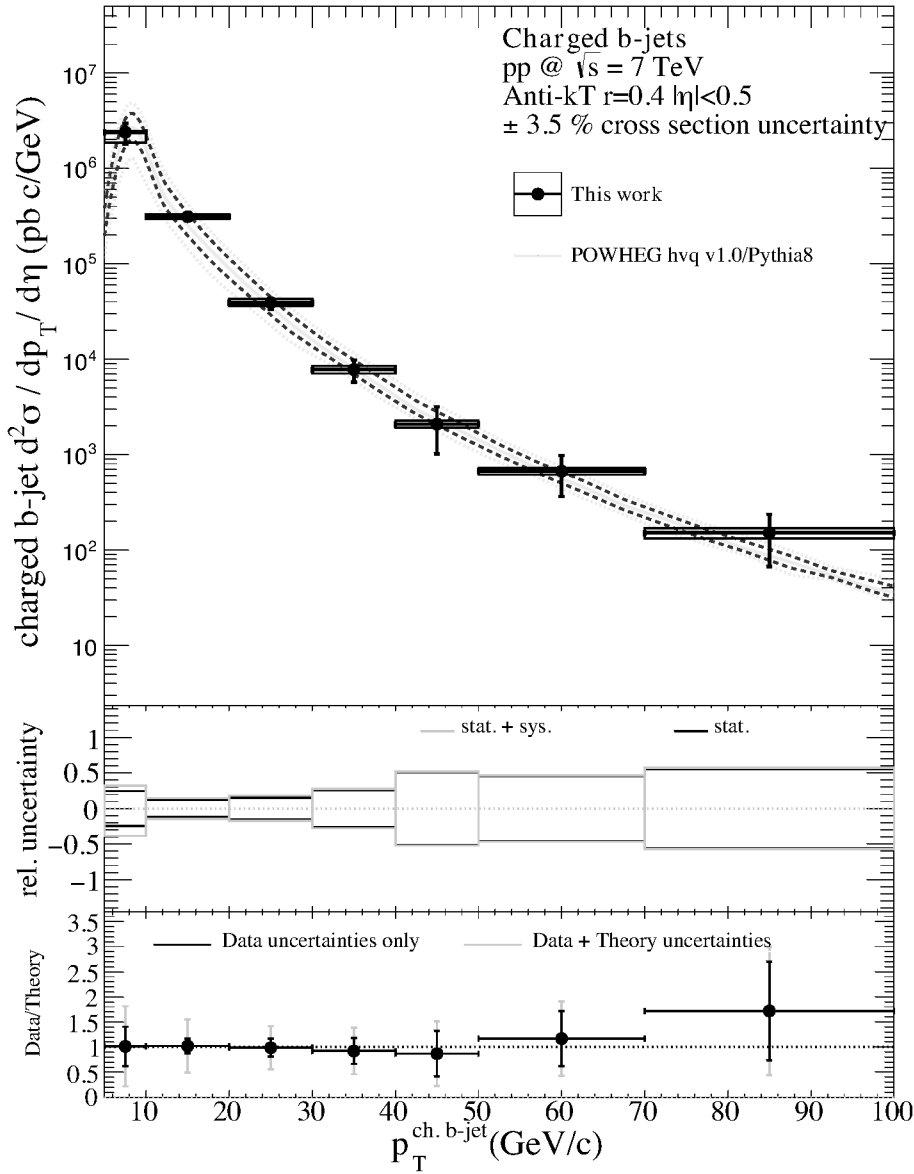
Figure 4.37: *Final corrected spectrum and* POWHEG *(CTEQ6.6)/*PYTHIA*8 (Monash 2013 tune [115]) comparison for pp collisions at $\sqrt{s} = 7$ TeV (This Work).*

Source	5-10	10-20	20-30	30-40	40-50	50-70	70-100
Template uncertainty[4]	20%	5%	1%	<1%	1%	<1%	1%
Tracking efficiency	3%	6%	7%	9%	8%	9%	11%
Unfolding							
Prior	1%	<1%	<1%	1%	<1%	1%	2%
Method	22%	2%	6%	2%	6%	1%	3%
Regularization	1%	1%	3%	1%	9%	2%	6%
Normalization	3.5%	3.5%	3.5%	3.5%	3.5%	3.5%	3.5 %
Total	30.1%	8.9%	10.4%	10.0%	13.9%	10.1%	13.5 %

Table 4.9: *Summary of systematic uncertainties for the different jet momentum bins.*

This section presents the final fully corrected charged beauty-jet spectrum in proton-proton at $\sqrt{s} = 7$ TeV collisions. The spectrum as shown in figure 4.37 was obtained using the Jet-Jet Monte Carlo based impact parameter significance templates and all available data. The underlying event momentum density is subtracted, but no outlier optimization (see section 4.9.1) is performed. Table 4.9 lists the different contributions to the total systematic uncertainty with respect to the final spectrum. The impact of the template uncertainties were calculated by excluding/including them prior to the template fit and comparing the final unfolded spectra.

The impact of the magnetic field polarity, of the UE subtraction as well as of the outlier optimization is studied in the following paragraphs.

4.13.1 Influence of the magnetic field polarity

As discussed in section 4.8 a dependence of the impact parameter mean value depending on the polarity of the L3 magnet has been found. As the correction value (see. section 4.8.3) of the impact parameter mean is only consistent with the observed mean value for $B > 0$ it needs to be verified that the impact of the runs taken at $B < 0$ does not significantly alter final result. Figure 4.38 shows the comparison of the final results using all data taking runs, those with a positive magnetic field and the remaining with negative magnetic field. It can be observed that for all three cases the final data points are in
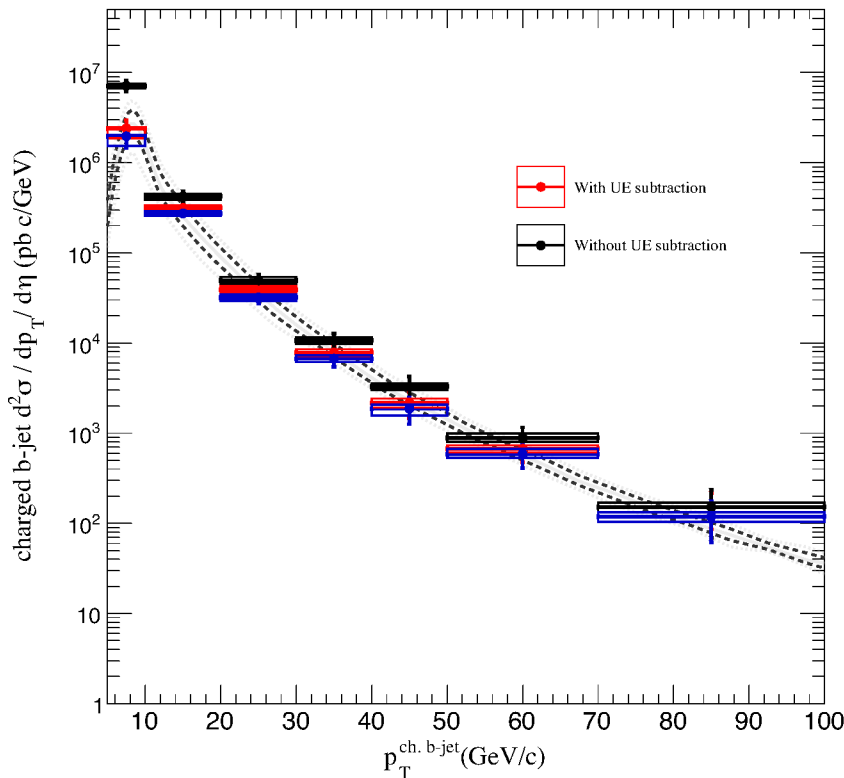
Figure 4.38: *Comparison of the final fully corrected charged beauty jet spectrum based on data taken at different L3 polarities (*POWHEG *predictions shown for better comparability only.).*

full agreement. The large uncertainties for $B < 0$ are compatible with the much lower available statistics. There is also no indication of any systematic upward or downward pull for $B > 0$ or $B < 0$ with respect to the combined dataset.

4.13.2 Influence of the underlying event subtraction

The mean underlying event momentum density (see 4.5) is expected to be negligible in proton-proton collisions therefore any effect on the final spectrum is expected to occur at low transverse jet momenta. Figure 4.39 shows the comparison of the final result to

the result obtained without using the underlying event subtraction. All points above
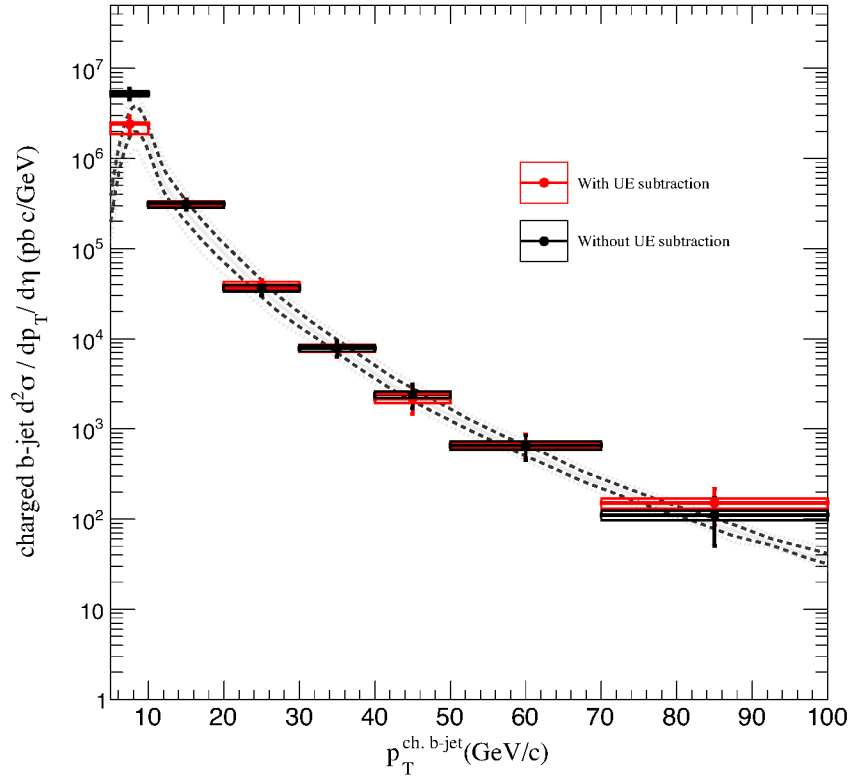
Figure 4.39: *Comparison the final fully corrected charged beauty jet spectrum with and without the application of the UE subtraction (*POWHEG *predictions shown for better comparability only.).*

$p_T^{\mathrm{ch.b-jet}} = 10$ GeV/c are compatible within the respective uncertainties. The lowest 5-10 GeV/c bin is lowered significantly when the UE subtraction is applied.

4.13.3 Influence of the template outlier reduction

As discussed in section 4.9.1 two outlier removal schemes were implemented. The influence on the final spectrum can be seen in Figure 4.40.
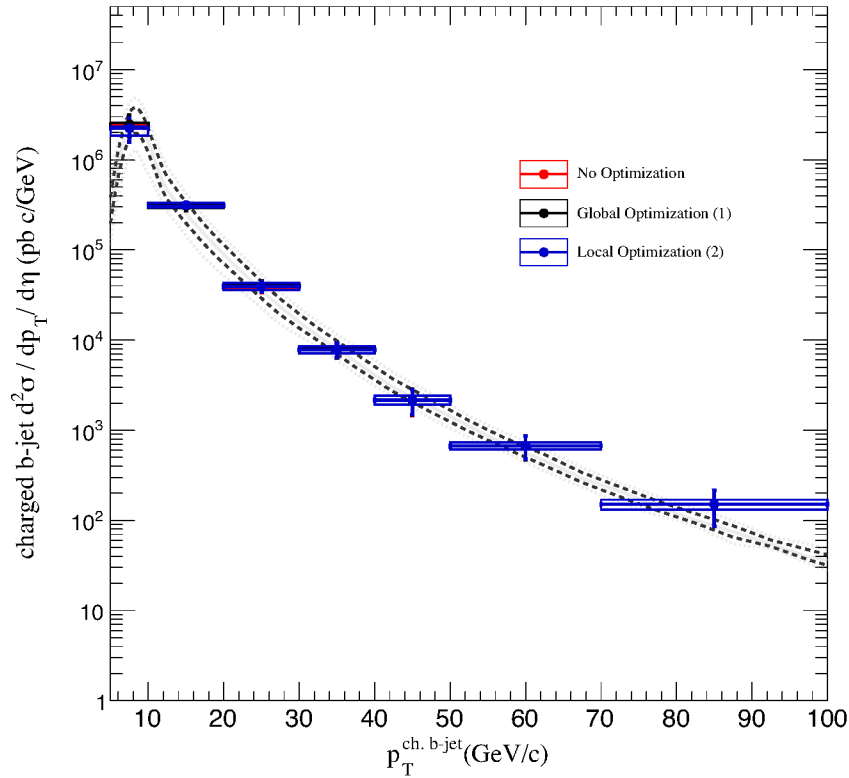
Figure 4.40: *Comparison of the final spectrum for different outlier removal strategies* (POWHEG *predictions shown for better comparability only.*).

All three spectra are fully compatible indicating that the impact of the proposed outlier removal strategies is negligible.

4.14 Discussion and theory comparison

Based on the previously presented sub-studies it has been found that the impact of low template statistics outweighs the differences between merged and Jet-Jet Monte-Carlo so the latter is used. In favour of the increased statistics an additional systematic uncertainty of 2% has been added to the raw template uncertainties. The outlier reduction scheme, using a global threshold shows negligible impact on the final spectrum, the local threshold however has a visible impact. As a exclusion of bins is equivalent to a reduction in statistics of the templates, the observed slight overall beauty jet cross section reduction in combination with the increased total uncertainties can however again be explained as such. As no qualitatively new behaviour in the shape of the spectrum emerges, the impact of outliers on the final result is assessed negligible. The impact of the magnetic field polarity fits into the same pattern and no apparent bias due to the relative offset in the mean impact parameters can be observed. Therefore the full available data is used for the final result. Lastly the underlying event subtraction significantly alters the low-p_T yield towards lower values while it preserves the results at higher momenta. This indicates that the especially for the low momentum bins the UE is not negligible and has to be thoroughly considered. The final result therefore includes the described UE subtraction.

It should be noted that the underlying event description of the simulation is expected to strongly depend on the used PYTHIA tune. The Monash 2013 tune produce a reasonable description of the UE (c.f. [111]) however the largest deviations are expected in the low-momentum part of the spectrum. In that respect the comparison to the presented POWHEG spectrum should be taken with great care especially at low transverse jet momentum. Therefore it might be advised to perform further Monte Carlo simulation studies in the future, to carefully check the influence of different PYTHIA tunes as well as of different PDF sets. Also shown in figure 4.37 is the comparison of the reconstructed spectrum to POWHEG/hvq predictions including different scale variations and based on CTEQ6.6m PDFs.

The b-jet over inclusive fraction can be calculated using the published 7 TeV inclusive charged jet spectrum [131] measured by ALICE as a reference. Figure (4.41) shows the corresponding fraction.
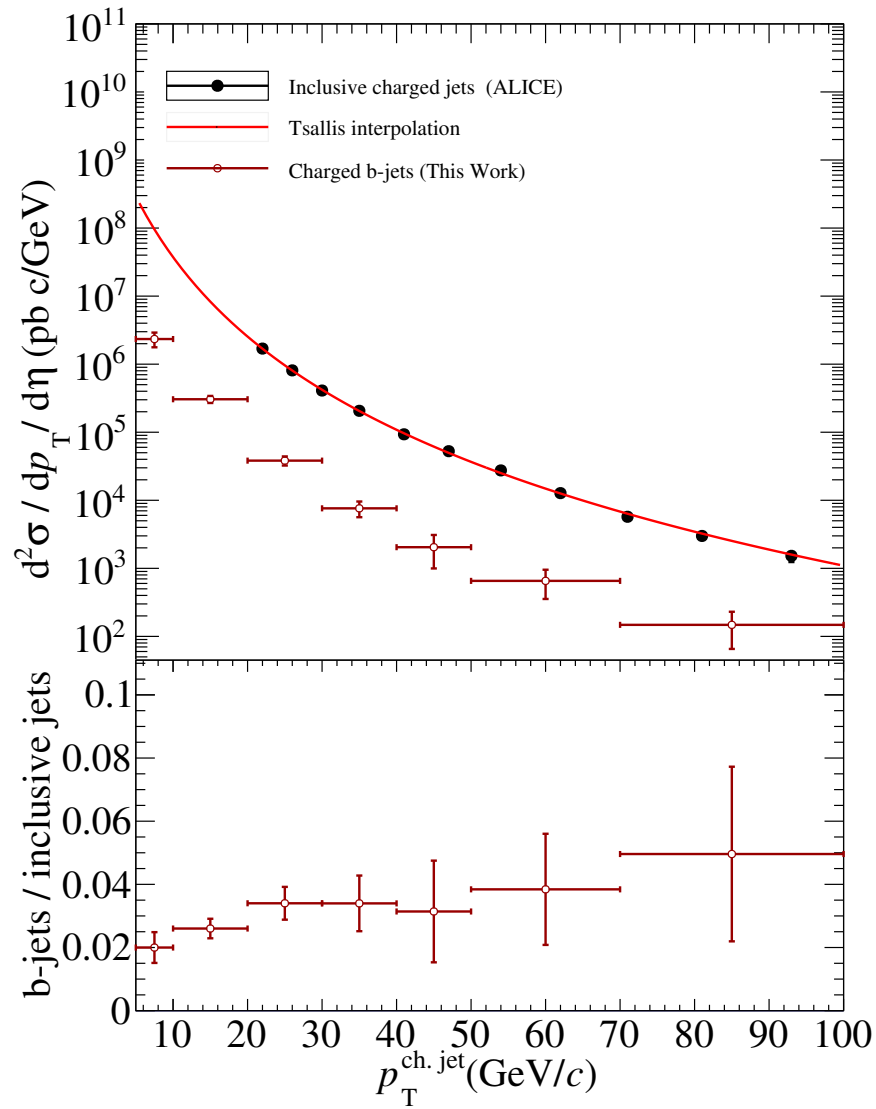
Figure 4.41: *Ratio of the charged beauty jet spectrum and the inclusive charged jet measured by ALICE[131] .*

Since a different binning was used in the inclusive jet analysis the data points were parametrized using a Tsallis fit before the fraction was calculated. The resulting fraction in the intermediate momentum region above $p_{\mathrm{T}}^{ch.jet} = 20$ GeV/c is of the order of 3%-4%. It should be noted that that the corrected inclusive jet spectrum obtained from the data and machinery used in this analysis is in full agreement with the published inclusive jet spectrum and therefore only the published spectrum is shown in figure 4.41 .

Summary

This work presents the first reconstruction of the inclusive charged beauty jet production cross section in proton-proton collisions at $\sqrt{s} = 7$ TeV with the ALICE detector. For this a new analysis strategy was developed that exploits the characteristic distributions for the three largest track impact parameter significances within beauty-, charm- and light flavour-jets, to extract the charged beauty-jet fraction from the measured reconstructed inclusive signed impact parameter significance distributions. The discussed strategy makes use of multiple published ALICE measurements of identified particles to devise a re-weighting scheme for the available PYTHIA/GEANT Monte Carlo productions in order to extract realistic signed track impact parameter distribution templates. The re-weighting is supplemented by a smearing and shifting procedure that accounts for residual detector differences in data and simulation.

A template fit using the extracted and corrected signed impact parameter significance distributions for the three largest impact parameters within a given jet was used to extract the beauty-jet fraction from the inclusively measured distributions. The resulting three partially correlated observables were then combined using the BLUE method to make best use of all available information. The detector level charged beauty-jet spectrum spectrum were then calculated using the obtained BLUE b-jet fraction resulting in the measured inclusive charged jet spectrum. Several studies with modified data selections as well as with different template optimization strategies were performed. Also the influence of the underlying event and its subtraction was studied.

The final spectrum covers the jet momentum range from 5 GeV/c to 100 GeV/c and was found to be in good agreement with theoretical predictions obtained from POWHEG-hvq/PYTHIA8 simulations.

Beside the reconstruction of the charged b-jet cross section, an optimized particle identification method for the ALICE TRD based on artificial neural networks was implemented and the improved performance over traditional PID methods is shown for p–Pb Collisions at $\sqrt{s} = 5.02$ TeV.

Zusammenfassung

Diese Arbeit präsentiert die erste Rekonstruktion des inklusiven Beauty-Jet Wirkungsquerschnittes in ultra-relativistischen Proton-Proton Kollisionen bei einer Schwerpunktsenergie von $\sqrt{s} = 7$ TeV mit dem ALICE Detektor. Die vorgestellte Methodik basiert auf der statistisch größeren Wahrscheinlichkeit der Konstituenten von Beauty-Jets aus dem Zerfallsvertex eines schweren Mesons zu entstammen und somit nicht aus dem primären Kollisionsvertex. Als Maß für die Kompatibilität des Ursprungs einer Teilchenspur mit dem primären Vertex dient dabei die so-genannte Spur-Stoßparametersignifikanz. Die vorgestellte Analyse nutzt dabei die drei größten Stoßparametersignifikanzen innerhalb eines rekonstruierten Jets als Observablen. Musterverteilungen für diese Observablen für Beauty- und Charm-Jets, sowie für Jets aus der Hadronisierung von leichten Quarks und Gluonen werden anhand von PYTHIA/GEANT Monte Carlo Simulationen bestimmt. Die Simulationen wurden dabei, auf Basis von früheren Messungen, neu gewichtet und für die nicht vollständig korrekte Beschreibung der Detektoreigenschaften korrigiert. Diese Musterverteilungen dienen schließlich als Basis eines additiven Modells, mit dessen Hilfe der relative Anteil der Beauty-Jets an den inklusiven Verteilungen bestimmt werden kann. Die Methode kombiniert die resultierenden drei disjunkten Verteilungen unter Berücksichtigung ihrer jeweiligen Korrelationen um den impulsabhängigen Anteil von Beauty-Jets und somit das Spektrum derselben zu bestimmen. Durch Entfaltung des resultierenden Spektrums und entsprechender Normierung ergibt sich schließlich das finale Spektrum im Impulsbereich von 5 GeV/c $\leq$ p$_T^{\text{ch.b-jet}} \leq$ 100 GeV/c.

Der Vergleich des so bestimmten Spektrums mit POWHEG/PYTHIA8 Vorhersagen zeigt eine gute Übereinstimmung in Bestätigung des Standardmodells. Das hier dokumentierte Verfahren kann als Grundlage für das Studium anderer Kollisionssysteme und schlussendlich zur Untersuchung des Energieverlustes schwerer Quarks im Quark-Gluonen Plasma dienen.

Neben der präsentierten Beauty-Jet Analyse wurde ein Teilchenidentifikationsverfahren für den ALICE TRD auf Basis künstlicher neuronaler Netze entwickelt und dessen gesteigerte Leistung anhand von Proton-Blei Daten bei einer Schwerpunktsenergie von $\sqrt{s} = 5.02$ TeV präsentiert.

Appendix A

Additional figures

A.1 Signed impact parameter significance distributions
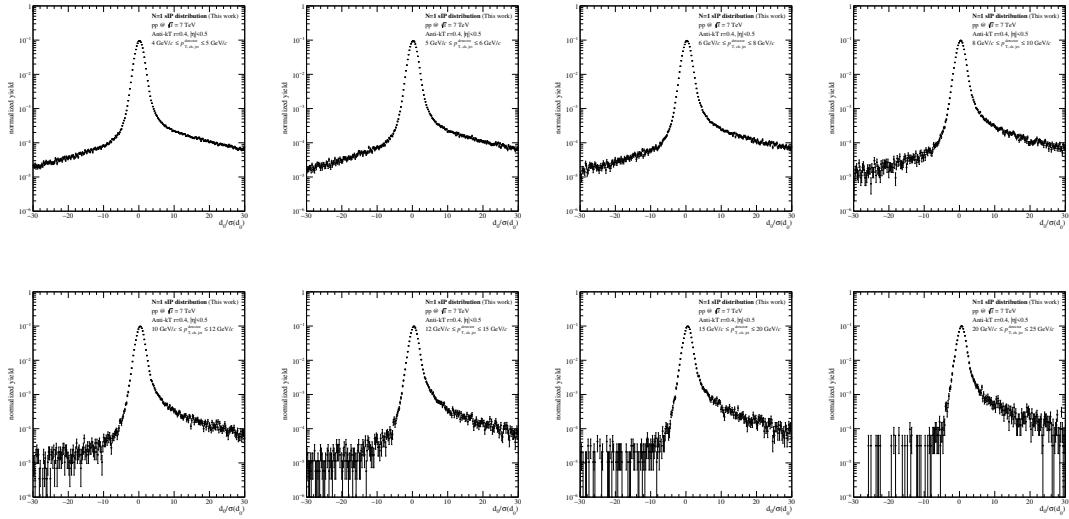
Figure A.1: $N = 1$ *template distributions extracted from ALICE 2010 proton-proton collisions at $\sqrt{s} = 7$ TeV (Part 1).*
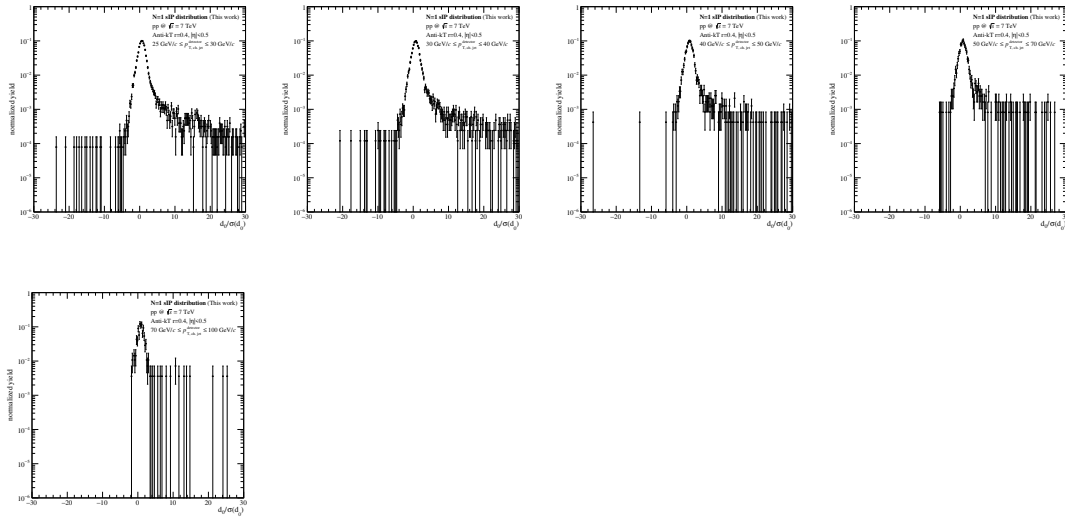
Figure A.2: $N = 1$ *template distributions extracted from ALICE 2010 proton-proton collisions at $\sqrt{s} = 7$ TeV (Part 2).*
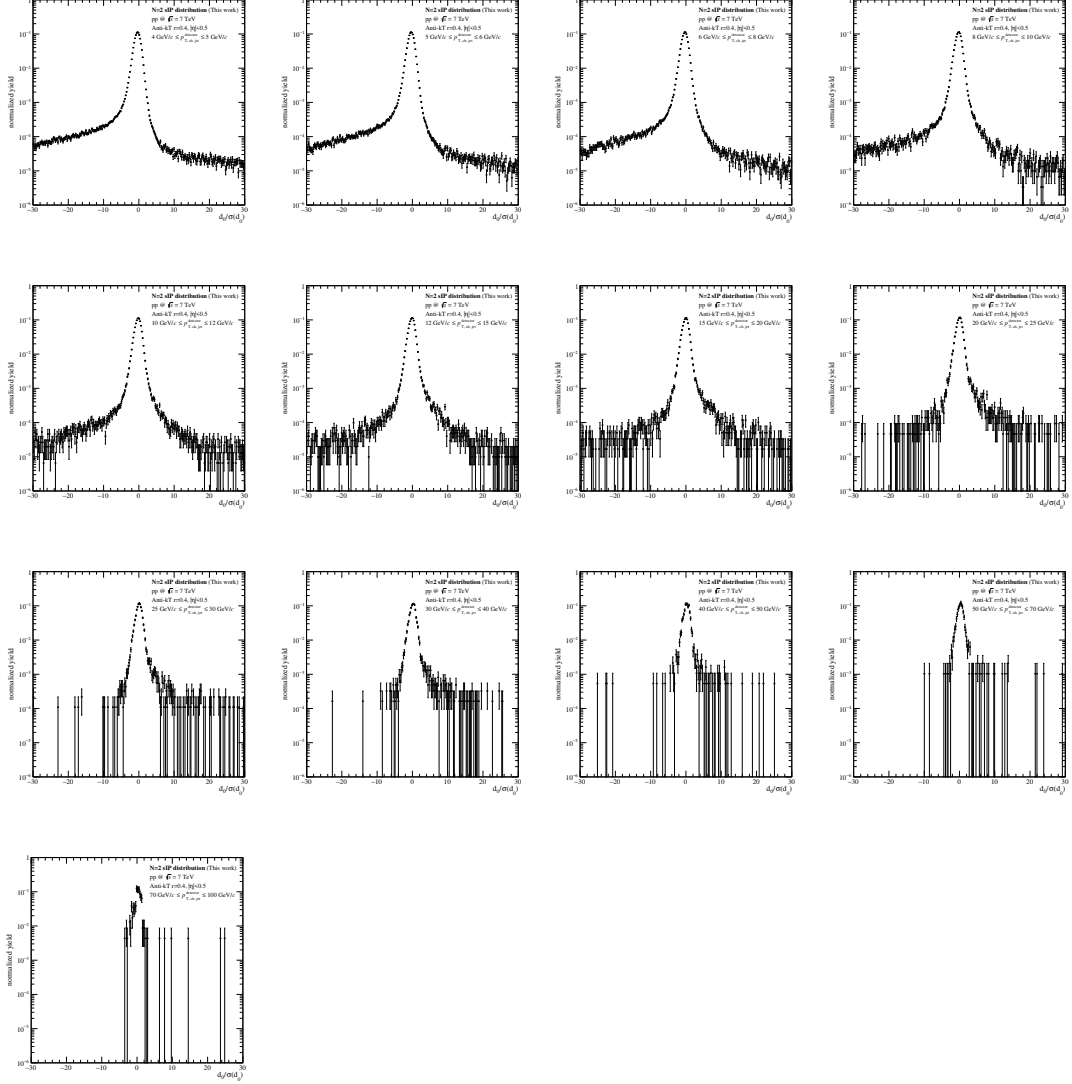
Figure A.3: $N = 2$ template distributions extracted from ALICE 2010 proton-proton collisions at $\sqrt{s} = 7$ TeV.
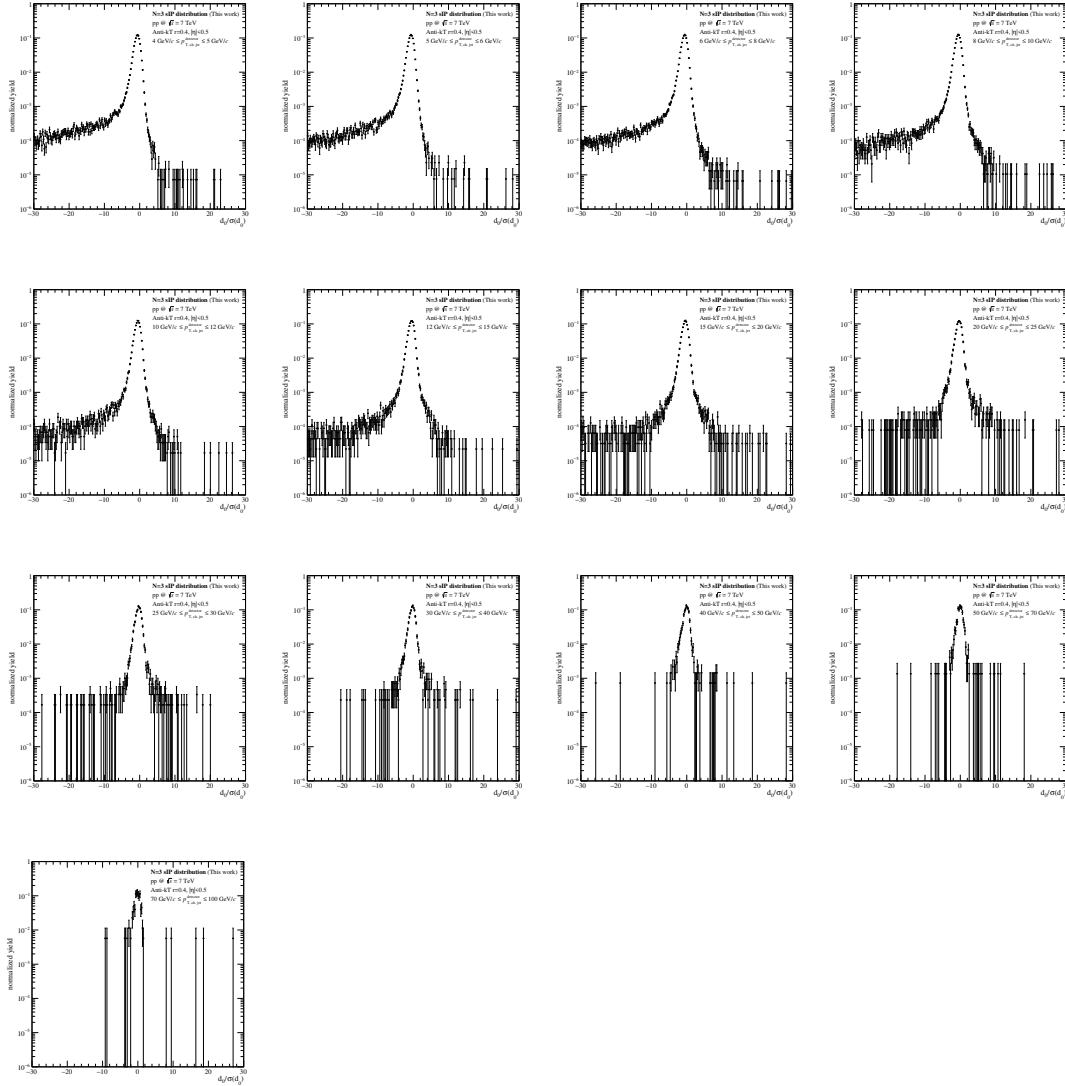
Figure A.4: $N = 3$ *template distributions extracted from ALICE 2010 proton-proton collisions at* $\sqrt{s} = 7$ *TeV.*

A.2 References for Monte Carlo re-weighting
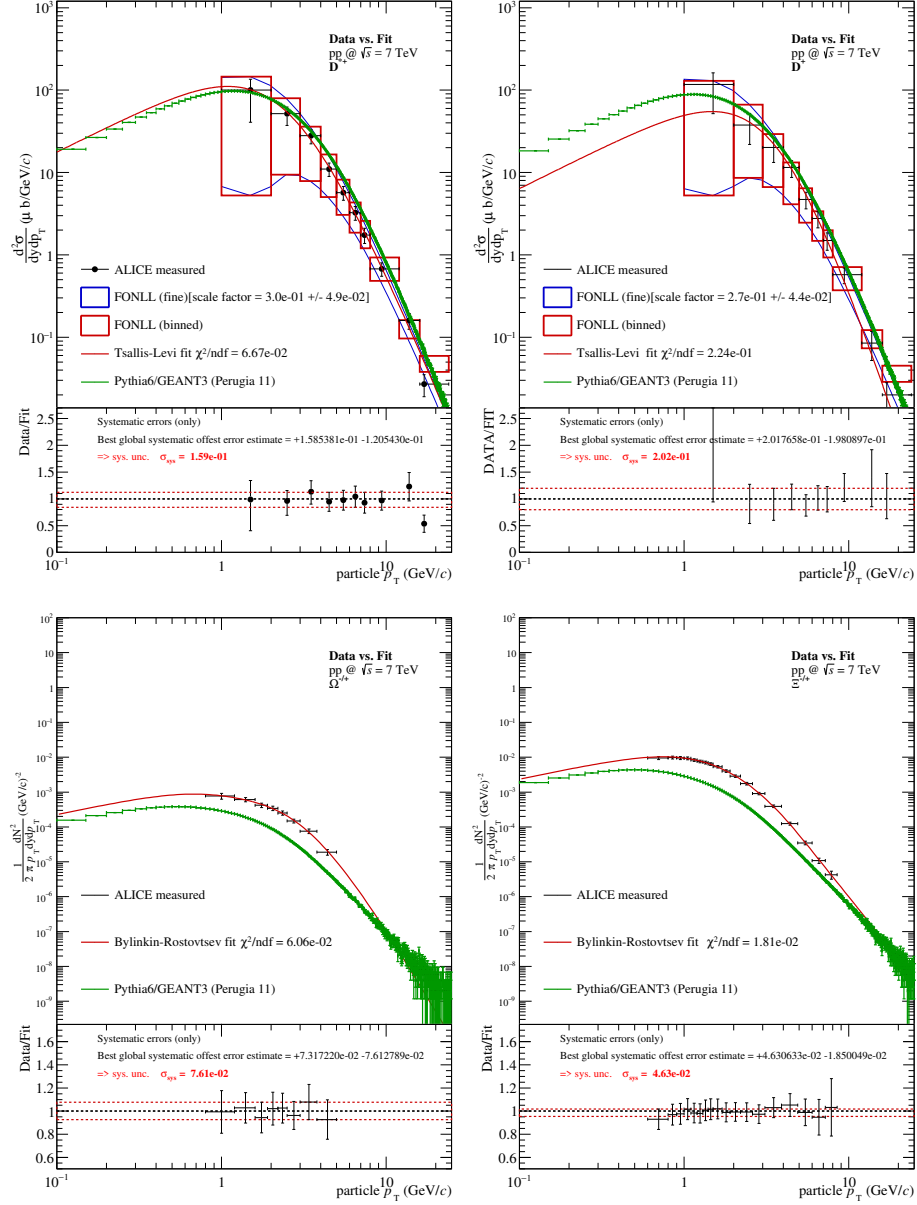
Figure A.5: *Additional identified particle reference spectra for Monte Carlo re-weighting.*

A.3   Template fit results
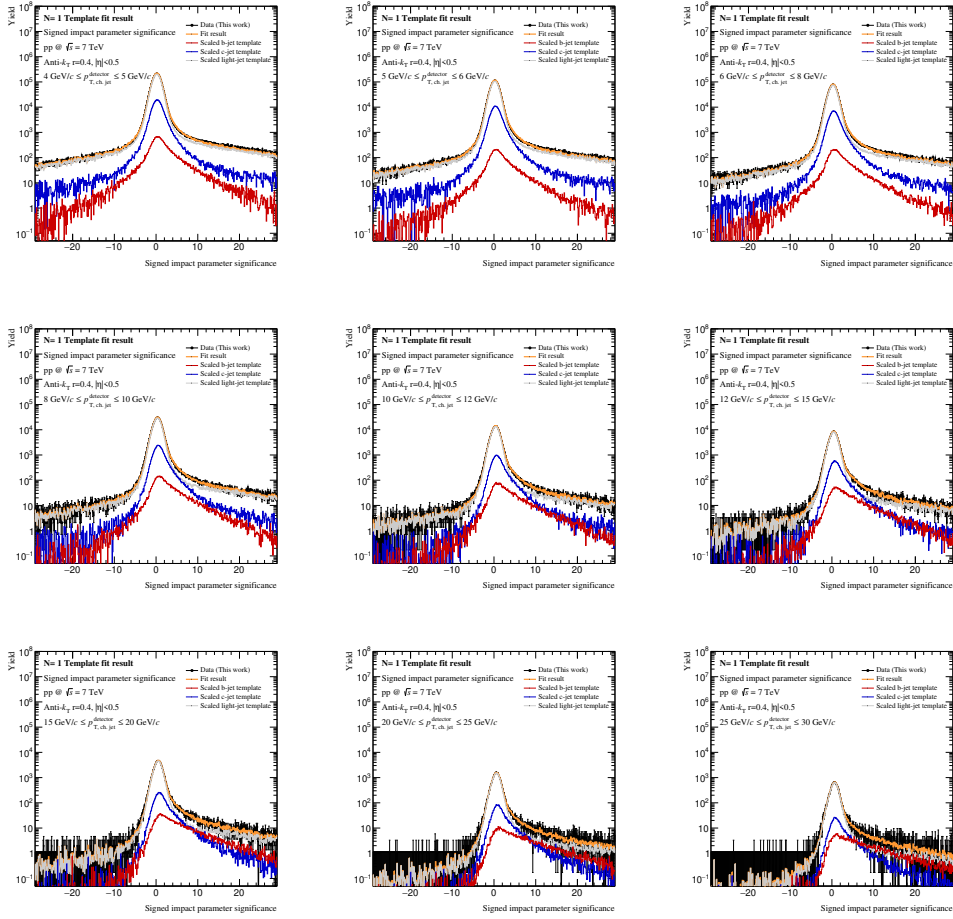
Figure A.6: $N = 1$ *template fit results (Part 1)*
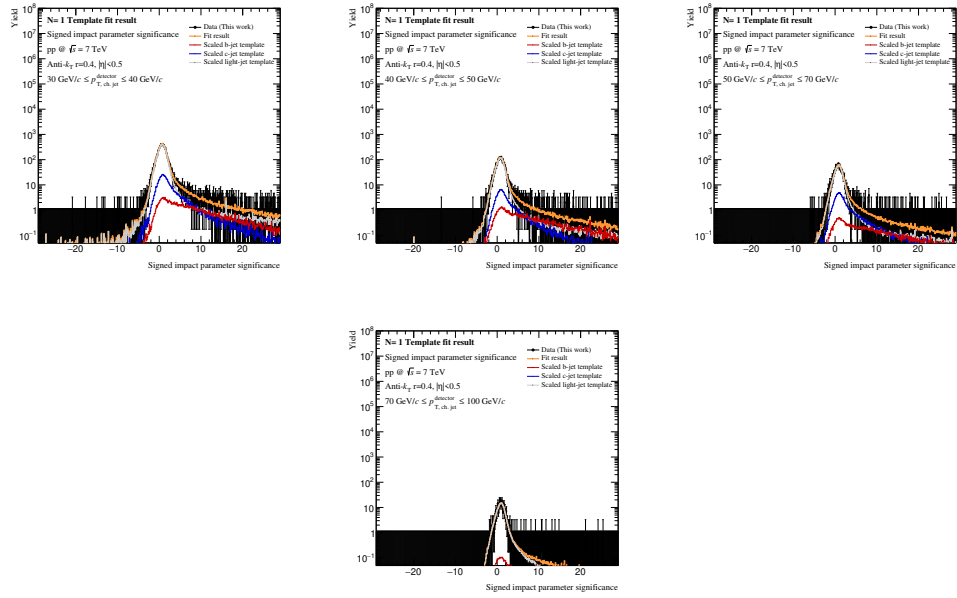
Figure A.7: $N = 1$ *template fit results (Part 2)*
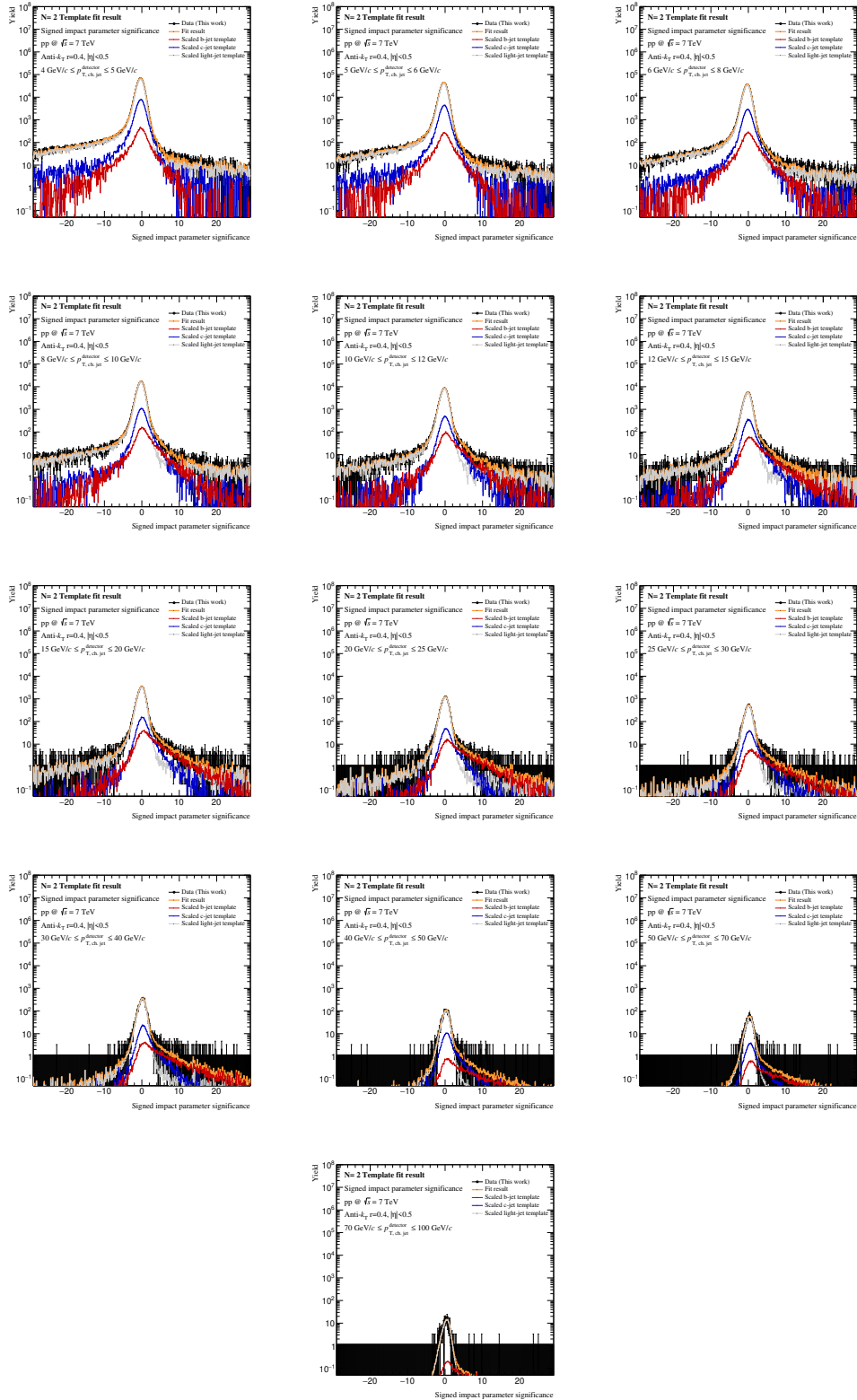
Figure A.8: *N = 2 template fit results*
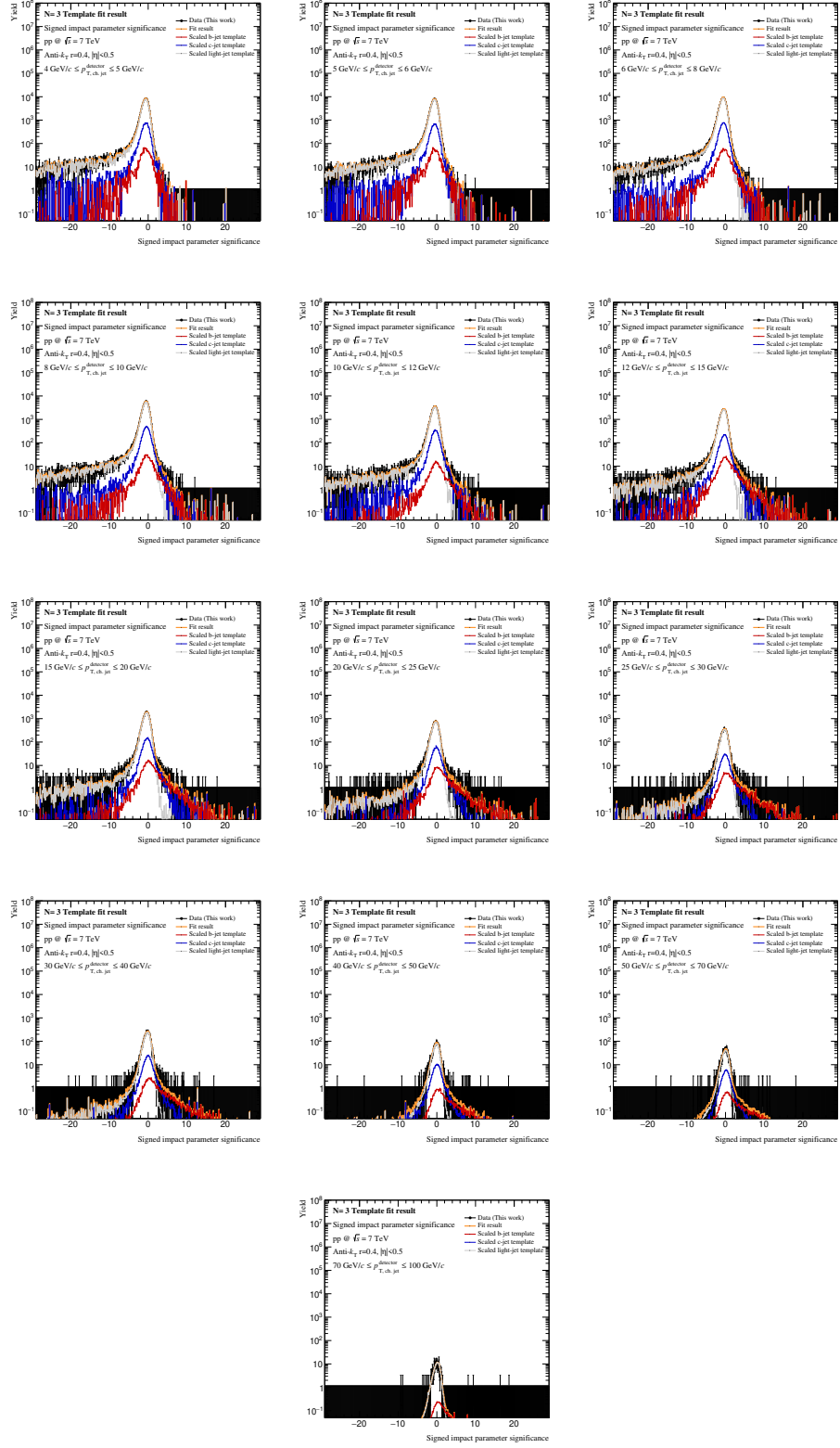
Figure A.9: *N = 3 template fit results*

Bibliography

[1] Serguei Chatrchyan et al. "Observation of a new boson at a mass of 125 GeV with the CMS experiment at the LHC". In: *Phys. Lett.* B716 (2012), pp. 30–61. DOI: 10.1016/j.physletb.2012.08.021. arXiv: 1207.7235 [hep-ex].

[2] Georges Aad et al. "Observation of a new particle in the search for the Standard Model Higgs boson with the ATLAS detector at the LHC". In: *Phys. Lett.* B716 (2012), pp. 1–29. DOI: 10.1016/j.physletb.2012.08.020. arXiv: 1207.7214 [hep-ex].

[3] *Combined measurements of the Higgs boson production and decay rates in $H \to ZZ^* \to 4\ell$ and $H \to \gamma\gamma$ final states using pp collision data at $\sqrt{s} = 13$ TeV in the ATLAS experiment.* Tech. rep. ATLAS-CONF-2016-081. Geneva: CERN, Aug. 2016. URL: https://cds.cern.ch/record/2206272.

[4] *Updated measurements of Higgs boson production in the diphoton decay channel at $\sqrt{s} = 13$ TeV in pp collisions at CMS.* Tech. rep. CMS-PAS-HIG-16-020. Geneva: CERN, 2016. URL: https://cds.cern.ch/record/2205275.

[5] *Measurements of properties of the Higgs boson and search for an additional resonance in the four-lepton final state at sqrt(s) = 13 TeV.* Tech. rep. CMS-PAS-HIG-16-033. Geneva: CERN, 2016. URL: https://cds.cern.ch/record/2204926.

[6] Morad Aaboud et al. "Combined measurement of differential and total cross sections in the $H \to \gamma\gamma$ and the $H \to ZZ^* \to 4\ell$ decay channels at $\sqrt{s} = 13$ TeV with the ATLAS detector". In: (2018). arXiv: 1805.10197 [hep-ex].

[7] R Aaij et al. "First Evidence for the Decay $B_s^0 \to \mu^+\mu^-$". In: *Phys. Rev. Lett.* 110.2 (2013), p. 021801. DOI: 10.1103/PhysRevLett.110.021801. arXiv: 1211.2674 [hep-ex].

[8] Roel Aaij et al. "Observation of two new Ξ_b^- baryon resonances". In: *Phys. Rev. Lett.* 114 (2015), p. 062004. DOI: 10.1103/PhysRevLett.114.062004. arXiv: 1411.4849 [hep-ex].

[9] Roel Aaij et al. "Observation of $J/\psi p$ Resonances Consistent with Pentaquark States in $\Lambda_b^0 \to J/\psi K^- p$ Decays". In: *Phys. Rev. Lett.* 115 (2015), p. 072001. DOI: 10.1103/PhysRevLett.115.072001. arXiv: 1507.03414 [hep-ex].

[10] *ALICE Collaboration.* Accessed = 28.05.2018. URL: http://aliceinfo.cern.ch/Public/Welcome.html.

[11] John M. Campbell, J. W. Huston, and W. J. Stirling. "Hard Interactions of Quarks and Gluons: A Primer for LHC Physics". In: *Rept. Prog. Phys.* 70 (2007), p. 89. DOI: 10.1088/0034-4885/70/1/R02. arXiv: hep-ph/0611148 [hep-ph].

[12] R. Pasechnik and M. Šumbera. "Phenomenological Review on Quark-Gluon Plasma: Concepts vs. Observations". In: *Universe* 3 (Jan. 2017), p. 7. DOI: 10.3390/universe3010007. arXiv: 1611.01533 [hep-ph].

[13] Yuri L. Dokshitzer and D. E. Kharzeev. "Heavy quark colorimetry of QCD matter". In: *Phys. Lett.* B519 (2001), pp. 199–206. DOI: 10.1016/S0370-2693(01)01130-3. arXiv: hep-ph/0106202 [hep-ph].

[14] Wen-Chang Xiang, Heng-Tong Ding, and Dai-Cui Zhou. "Radiative energy loss of heavy quark and dead cone effect in ultra-relativistic heavy ion collisions". In: *Chin. Phys. Lett.* 22 (2005), pp. 72–75. DOI: 10.1088/0256-307X/22/1/021.

[15] Jinrui Huang, Zhong-Bo Kang, and Ivan Vitev. "Inclusive b-jet production in heavy ion collisions at the LHC". In: *Phys. Lett.* B726 (2013), pp. 251–256. DOI: `10.1016/j.physletb.2013.08.009`. arXiv: `1306.0909 [hep-ph]`.

[16] Christiane Lefèvre. "The CERN accelerator complex. Complexe des accélérateurs du CERN". Dec. 2008. URL: `https://cds.cern.ch/record/1260465`.

[17] Lyndon Evans and Philip Bryant. "LHC Machine". In: *JINST* 3 (2008), S08001. DOI: `10.1088/1748-0221/3/08/S08001`.

[18] Rudiger Voss and Amos Breskin, eds. *The CERN Large Hadron Collider, accelerator and experiments*. 2009. URL: `http://www-spires.fnal.gov/spires/find/books/www?cl=QC787.P73C37::2009`.

[19] R. Assmann, M. Lamont, and S. Myers. "A brief history of the LEP collider". In: *Nucl. Phys. Proc. Suppl.* 109B (2002). [,17(2002)], pp. 17–31. DOI: `10.1016/S0920-5632(02)90005-8`.

[20] Valeriane Duvivier. "Cross section of LHC dipole.. Dipole LHC: Coupe transversale." AC Collection. Legacy of AC. Pictures from 1992 to 2002. 2001. URL: `http://cds.cern.ch/record/843195`.

[21] R Scrivens et al. "Overview of the status and developments on primary ion sources at CERN*". In: CERN-ATS-2011-172 (Sept. 2011), 4 p. URL: `https://cds.cern.ch/record/1382102`.

[22] M. Weiss. "The RFQ2 complex: The future injector to CERN Linac 2". In: *Conf. Proc.* C920324 (1992). [,539(1992)], pp. 539–541.

[23] A. Blas et al. "The PS complex as proton pre-injector for the LHC: Design and implementation report". In: CERN-2000-003 (2000). Ed. by M. Benedikt.

[24] P. Collier et al. "The SPS as injector for LHC: Conceptual design". In: CERN-SL-97-007-DI (1997).

[25] T. Bohl. "Bunch compression in the SPS as LHC injector". In: *Part. Accel.* 58 (1997), pp. 237–240.

[26] Mike Lamont. "The First Years of LHC Operation for Luminosity Production". In: *Proceedings, 4th International Particle Accelerator Conference (IPAC 2013): Shanghai, China, May 12-17, 2013.* 2013, MOYAB101. URL: `http://JACoW.org/IPAC2013/papers/moyab101.pdf`.

[27] Z. Q. Xie. "State of the Art of ECR Ion Sources". In: *Conf. Proc.* C970512 (1997), p. 2662.

[28] C E Hill, Detlef Küchler, and Geneva Switzerland. "The 18 GHz upgrade of the CERN ECR4 ion source". In: AB-Note-2003-008-ABP (May 2018).

[29] Michael Benedikt et al. *LHC Design Report*. CERN Yellow Reports: Monographs. Geneva: CERN, 2004. URL: `https://cds.cern.ch/record/823808`.

[30] A. Beuret et al. "The LHC lead injector chain". In: Proceedings of EPAC (2004).

[31] C. Fabjan and J. Schukraft. "The Story of ALICE: Building the dedicated heavy ion detector at LHC". In: *'The Large Hadron Collider: A marvel technology', EPFL-Press Lausanne, Switzerland, 2009 (Editor: L. Evans), chapter 5.4.* 2011. arXiv: `1101.1257 [physics.ins-det]`. URL: `https://inspirehep.net/record/883486/files/arXiv:1101.1257.pdf`.

[32] "The Construction of the L3 Experiment". In: *Nucl. Instrum. Meth.* A289 (1990), pp. 35–102. DOI: `10.1016/0168-9002(90)90250-A`.

[33] O. Adriani et al. "Results from the L3 experiment at LEP". In: *Phys. Rept.* 236 (1993), pp. 1–146. DOI: `10.1016/0370-1573(93)90027-B`.

[34] Betty Bezverkhny Abelev et al. "Performance of the ALICE Experiment at the CERN LHC". In: *Int. J. Mod. Phys.* A29 (2014), p. 1430044. DOI: `10.1142/S0217751X14300440`. arXiv: `1402.4476 [nucl-ex]`.

[35] L. Betev et al. "Definition of the ALICE coordinate system and basic rules for sub-detector components numbering." In: (2003). URL: `http://edms.cern.ch/file/406391/1ALICE-INT-2003-03`.

[36] P. Kuijer. "The inner tracking system of the Alice experiment". In: *Nucl. Instrum. Meth.* A530 (2004), pp. 28–32. DOI: `10.1016/j.nima.2004.05.042`.

[37] G. Dellacasa et al. "ALICE technical design report of the inner tracking system (ITS)". In: CERN-LHCC-99-12 (1999).

[38] K Aamodt et al. "Alignment of the ALICE Inner Tracking System with cosmic-ray tracks". In: *JINST* 5 (2010), P03003. DOI: `10.1088/1748-0221/5/03/P03003`. arXiv: `1001.0502 [physics.ins-det]`.

[39] D. Nouais et al. "The Alice silicon drift detector system". In: *Nucl. Instrum. Meth.* A501 (2001), pp. 119–125. DOI: `10.1016/S0168-9002(02)02020-X`.

[40] Yvonne Pachmayer. "Physics with the ALICE Transition Radiation Detector". In: (2011). [Nucl. Instrum. Meth.A706,6(2013)]. DOI: `10.1016/j.nima.2012.05.016`. arXiv: `1112.2098 [nucl-ex]`.

[41] Alexander Wilk. "Particle Identification using Artificial Neural Networks with the ALICE TRD". PhD thesis. Munster U., 2010. URL: `http://inspirehep.net/record/1231193/files/diss_wilk.pdf`.

[42] Fabio M. Soares and Alan M. F. Souza. *Neural Network Programming with Java - Second Edition.* 2nd. Packt Publishing, 2017. ISBN: 1787126056, 9781787126053.

[43] Andreas Hoecker et al. "TMVA: Toolkit for Multivariate Data Analysis". In: *PoS* ACAT (2007), p. 040. arXiv: `physics/0703039`.

[44] C. Szegedy et al. "Inception-v4, Inception-ResNet and the Impact of Residual Connections on Learning". In: *ArXiv e-prints* (Feb. 2016). arXiv: `1602.07261 [cs.CV]`.

[45] Yangqing Jia. *Caffe: An Open Source Convolutional Architecture for Fast Feature Embedding.* `http://caffe.berkeleyvision.org/`. 2013.

[46] Alex Krizhevsky and Sutskever, Ilya and Hinton, Geoffrey E. "ImageNet Classification with Deep Convolutional Neural Networks". In: *Advances in Neural Information Processing Systems 25.* Ed. by F. Pereira and C. J. C. Burges and L. Bottou and K. Q. Weinberger. Curran Associates, Inc., 2012, 1097–1105. URL: `{http://papers.nips.cc/paper/4824-imagenet-classification-with-deep-convolutional-neural-networks.pdf}`.

[47] A. Akindinov et al. "The MRPC detector for the ALICE Time Of Flight system: Final design and performances". In: *Nucl. Phys. Proc. Suppl.* 158 (2006). [,60(2006)], pp. 60–65. DOI: `10.1016/j.nuclphysbps.2006.07.035`.

[48] A. Akindinov et al. "Performance of the ALICE Time-Of-Flight detector at the LHC". In: *Eur. Phys. J. Plus* 128 (2013), p. 44. DOI: `10.1140/epjp/i2013-13044-x`.

[49] Andrea Alici. "The MRPC-based ALICE Time-Of-Flight detector: status and performance". In: *Nucl. Instrum. Meth.* A706 (2013), pp. 29–32. DOI: `10.1016/j.nima.2012.05.004`. arXiv: `1203.5976 [physics.ins-det]`.

[50] C. Pastore et al. "The Cherenkov radiator system of the high momentum particle identification detector of the ALICE experiment at CERN-LHC". In: *Nucl. Instrum. Meth.* A639 (2011), pp. 231–233. DOI: `10.1016/j.nima.2010.10.069`.

[51] G. Dellacasa et al. "ALICE technical design report of the photon spectrometer (PHOS)". In: CERN-LHCC-99-04 (1999).

[52] C. Zhao et al. "Performance of the ALICE PHOS trigger and improvements for RUN 2". In: *JINST* 8 (2013), p. C12028. DOI: `10.1088/1748-0221/8/12/C12028`.

[53] "Shashlik Calorimetry A Combined Shashlik + Preshower Detector for LHC". Nov. 1993. URL: `http://cds.cern.ch/record/5470`.

[54] U. Abeysekara et al. "ALICE EMCal Physics Performance Report". In: (2010). arXiv: `1008.0413 [physics.ins-det]`.

[55] E. Abbas et al. "Performance of the ALICE VZERO system". In: *JINST* 8 (2013), P10016. DOI: `10.1088/1748-0221/8/10/P10016`. arXiv: `1306.3130 [nucl-ex]`.

[56] P Cortese et al. "ALICE technical design report on forward detectors: FMD, T0 and V0". In: CERN-LHCC-2004-025 (2004).

[57] Betty Abelev et al. "Measurement of inelastic, single- and double-diffraction cross sections in proton–proton collisions at the LHC with ALICE". In: *Eur. Phys. J.* C73.6 (2013), p. 2456. DOI: 10.1140/epjc/s10052-013-2456-0. arXiv: 1208.4968 [hep-ex].

[58] Jaroslav Adam et al. "Determination of the event collision time with the ALICE detector at the LHC". In: *Eur. Phys. J. Plus* 132.2 (2017), p. 99. DOI: 10.1140/epjp/i2017-11279-1. arXiv: 1610.03055 [physics.ins-det].

[59] "ALICE: Addendum to the technical design report of the Photon Multiplicity Detector (PMD)". In: CERN-LHCC-2003-038 (2003).

[60] G. Dellacasa et al. "ALICE technical design report: Photon multiplicity detector (PMD)". In: CERN-LHCC-99-32, CERN-OPEN-2000-184 (1999).

[61] Christian Holm Christensen et al. "The ALICE Forward Multiplicity Detector". In: *Int. J. Mod. Phys.* E16 (2007), pp. 2432–2437. DOI: 10.1142/S0218301307008057. arXiv: 0712.1117 [nucl-ex].

[62] R. Arnaldi et al. "Design and performance of the ALICE muon trigger system". In: *Nucl. Phys. Proc. Suppl.* 158 (2006). [,21(2006)], pp. 21–24. DOI: 10.1016/j.nuclphysbps.2006.07.012.

[63] Jaroslav Adam et al. "Study of cosmic ray events with high muon multiplicity using the ALICE detector at the CERN Large Hadron Collider". In: *JCAP* 1601.01 (2016), p. 032. DOI: 10.1088/1475-7516/2016/01/032. arXiv: 1507.07577 [astro-ph.HE].

[64] Artur Szostak. "Operational experience with the ALICE High Level Trigger". In: *J. Phys. Conf. Ser.* 396 (2012), p. 012048. DOI: 10.1088/1742-6596/396/1/012048.

[65] Christian Wolfgang Fabjan et al. "ALICE: Physics performance report, volume II". In: *J. Phys.* G32 (2006). Ed. by B Alessandro et al., pp. 1295–2040. DOI: 10.1088/0954-3899/32/10/001.

[66] R. Brun and F. Rademakers. "ROOT: An object oriented data analysis framework". In: *Nucl. Instrum. Meth.* A389 (1997), pp. 81–86. DOI: 10.1016/S0168-9002(97)00048-X.

[67] R Brun et al. "PAW, a general-purpose portable software tool for data analysis and presentation". In: CERN-DD-89-17 (May 1989), 9 p. URL: https://cds.cern.ch/record/197657.

[68] René Brun et al. "PAW++ : Physics Analysis Workstation : User's Guide". In: (1999). CERN Program Library Long Writeups. URL: https://cds.cern.ch/record/2296392.

[69] P. Saiz et al. "AliEn - ALICE environment on the GRID". In: *Nucl. Instrum. Meth.* A502 (2003), pp. 437–440. DOI: 10.1016/S0168-9002(03)00462-5.

[70] Markus Zimmermann. "The ALICE analysis train system". In: *J. Phys. Conf. Ser.* 608.1 (2015), p. 012019. DOI: 10.1088/1742-6596/608/1/012019. arXiv: 1502.06381 [hep-ex].

[71] Michael E. Peskin and Daniel V. Schroeder. *An Introduction to quantum field theory.* Reading, USA: Addison-Wesley, 1995. ISBN: 9780201503975, 0201503972. URL: http://www.slac.stanford.edu/~mpeskin/QFT.html.

[72] C. Patrignani et al. "Review of Particle Physics". In: *Chin. Phys.* C40.10 (2016), p. 100001. DOI: 10.1088/1674-1137/40/10/100001.

[73] L. D. Faddeev and V. N. Popov. "Feynman Diagrams for the Yang-Mills Field". In: *Phys. Lett.* B25 (1967). [,325(1967)], pp. 29–30. DOI: 10.1016/0370-2693(67)90067-6.

[74] Gerard 't Hooft. "Dimensional regularization and the renormalization group". In: *Nucl. Phys.* B61 (1973), pp. 455–468. DOI: 10.1016/0550-3213(73)90376-3.

[75] Steven Weinberg. "New approach to the renormalization group". In: *Phys. Rev.* D8 (1973), pp. 3497–3509. DOI: 10.1103/PhysRevD.8.3497.

[76] M. Czakon. "The Four-loop QCD beta-function and anomalous dimensions". In: *Nucl. Phys.* B710 (2005), pp. 485–498. DOI: 10.1016/j.nuclphysb.2005.01.012. arXiv: hep-ph/0411261 [hep-ph].

[77]   H. David Politzer. "Reliable Perturbative Results for Strong Interactions?" In: *Phys. Rev. Lett.* 30 (1973). [,274(1973)], pp. 1346–1349. DOI: 10.1103/PhysRevLett.30.1346.

[78]   David J. Gross and Frank Wilczek. "Ultraviolet Behavior of Nonabelian Gauge Theories". In: *Phys. Rev. Lett.* 30 (1973). [,271(1973)], pp. 1343–1346. DOI: 10.1103/PhysRevLett.30.1343.

[79]   Aude Gehrmann-De Ridder. *Perturbative QCD Lecture 1.* Tech. rep. CERN, 2013. URL: https://indico.cern.ch/event/230448/attachments/381911/531283/CERN1.pdf.

[80]   John C. Collins, Davison E. Soper, and George F. Sterman. "Factorization of Hard Processes in QCD". In: *Adv. Ser. Direct. High Energy Phys.* 5 (1989), pp. 1–91. DOI: 10.1142/9789814503266_0001. arXiv: hep-ph/0409313 [hep-ph].

[81]   A. D. Martin et al. "Parton distributions for the LHC". In: *Eur. Phys. J.* C63 (2009), pp. 189–285. DOI: 10.1140/epjc/s10052-009-1072-5. arXiv: 0901.0002 [hep-ph].

[82]   Francesco Cerutti and N. P. Hartland. "The NNPDF2.2 Parton Set". In: *J. Phys. Conf. Ser.* 368 (2012), p. 012063. DOI: 10.1088/1742-6596/368/1/012063. arXiv: 1111.6768 [hep-ph].

[83]   J. Pumplin et al. "New generation of parton distributions with uncertainties from global QCD analysis". In: *JHEP* 07 (2002), p. 012. DOI: 10.1088/1126-6708/2002/07/012. arXiv: hep-ph/0201195 [hep-ph].

[84]   Guido Altarelli and G. Parisi. "Asymptotic Freedom in Parton Language". In: *Nucl. Phys.* B126 (1977), pp. 298–318. DOI: 10.1016/0550-3213(77)90384-4.

[85]   Yuri L. Dokshitzer. "Calculation of the Structure Functions for Deep Inelastic Scattering and e+ e- Annihilation by Perturbation Theory in Quantum Chromodynamics." In: *Sov. Phys. JETP* 46 (1977). [Zh. Eksp. Teor. Fiz.73,1216(1977)], pp. 641–653.

[86]   V. N. Gribov and L. N. Lipatov. "Deep inelastic e p scattering in perturbation theory". In: *Sov. J. Nucl. Phys.* 15 (1972). [Yad. Fiz.15,781(1972)], pp. 438–450.

[87]   T. J. Hobbs. "The Nonperturbative Structure of Hadrons". PhD thesis. Indiana U., 2014-08. arXiv: 1408.5463 [hep-ph]. URL: http://inspirehep.net/record/1312182/files/arXiv:1408.5463.pdf.

[88]   C. Adloff et al. "Measurement of neutral and charged current cross-sections in electron - proton collisions at high Q^2". In: *Eur. Phys. J.* C19 (2001), pp. 269–288. DOI: 10.1007/s100520100607. arXiv: hep-ex/0012052 [hep-ex].

[89]   S. Chekanov et al. "Measurement of the neutral current cross-section and F(2) structure function for deep inelastic e + p scattering at HERA". In: *Eur. Phys. J.* C21 (2001), pp. 443–471. DOI: 10.1007/s100520100749. arXiv: hep-ex/0105090 [hep-ex].

[90]   R. S. Towell et al. "Improved measurement of the anti-d / anti-u asymmetry in the nucleon sea". In: *Phys. Rev.* D64 (2001), p. 052002. DOI: 10.1103/PhysRevD.64.052002. arXiv: hep-ex/0103030 [hep-ex].

[91]   B. Abbott et al. "High-p_T jets in $\bar{p}p$ collisions at $\sqrt{s} = 630$ GeV and 1800 GeV". In: *Phys. Rev.* D64 (2001), p. 032003. DOI: 10.1103/PhysRevD.64.032003. arXiv: hep-ex/0012046 [hep-ex].

[92]   C. Peterson et al. "Scaling Violations in Inclusive e+ e- Annihilation Spectra". In: *Phys. Rev.* D27 (1983), p. 105. DOI: 10.1103/PhysRevD.27.105.

[93]   V. G. Kartvelishvili, A. K. Likhoded, and V. A. Petrov. "On the Fragmentation Functions of Heavy Quarks Into Hadrons". In: *Phys. Lett.* 78B (1978), pp. 615–617. DOI: 10.1016/0370-2693(78)90653-6.

[94]   Bo Andersson et al. "Parton Fragmentation and String Dynamics". In: *Phys. Rept.* 97 (1983), pp. 31–145. DOI: 10.1016/0370-1573(83)90080-7.

[95]   D. Buskulic et al. "Measurement of the effective b quark fragmentation function at the Z resonance". In: *Phys. Lett.* B357 (1995), pp. 699–714. DOI: 10.1016/0370-2693(95)00988-W.

[96]   P. Nason, S. Dawson, and R. Keith Ellis. "The Total Cross-Section for the Production of Heavy Quarks in Hadronic Collisions". In: *Nucl. Phys.* B303 (1988), pp. 607–633. DOI: 10.1016/0550-3213(88)90422-1.

[97]   Kaoru Hagiwara and T. Yoshino. "Hadroproduction of Heavy Quark Flavors in QCD". In: *Phys. Lett.* 80B (1979), pp. 282–285. DOI: 10.1016/0370-2693(79)90217-X.

[98]   W. Beenakker et al. "QCD corrections to heavy quark production in hadron hadron collisions". In: *Nucl. Phys.* B351 (1991), pp. 507–560. DOI: 10.1016/S0550-3213(05)80032-X.

[99]   Michelangelo L. Mangano. "Two lectures on heavy quark production in hadronic collisions". In: *Proc. Int. Sch. Phys. Fermi* 137 (1998), pp. 95–137. DOI: 10.3254/978-1-61499-222-6-95. arXiv: hep-ph/9711337 [hep-ph].

[100] W. Beenakker et al. "QCD Corrections to Heavy Quark Production in p anti-p Collisions". In: *Phys. Rev.* D40 (1989), pp. 54–82. DOI: 10.1103/PhysRevD.40.54.

[101] P. Nason, S. Dawson, and R. Keith Ellis. "The One Particle Inclusive Differential Cross-Section for Heavy Quark Production in Hadronic Collisions". In: *Nucl. Phys.* B327 (1989). [Erratum: Nucl. Phys.B335,260(1990)], pp. 49–92. DOI: 10.1016/0550-3213(90)90180-L,10.1016/0550-3213(89)90286-1.

[102] R. Keith Ellis and P. Nason. "QCD Radiative Corrections to the Photoproduction of Heavy Quarks". In: *Nucl. Phys.* B312 (1989), pp. 551–570. DOI: 10.1016/0550-3213(89)90571-3.

[103] J. Smith and W. L. van Neerven. "QCD corrections to heavy flavor photoproduction and electroproduction". In: *Nucl. Phys.* B374 (1992), pp. 36–82. DOI: 10.1016/0550-3213(92)90476-R.

[104] Michelangelo L. Mangano, Paolo Nason, and Giovanni Ridolfi. "Heavy quark correlations in hadron collisions at next-to-leading order". In: *Nucl. Phys.* B373 (1992), pp. 295–345. DOI: 10.1016/0550-3213(92)90435-E.

[105] W. M. Alberico et al. "Heavy flavors in *AA* collisions: production, transport and final spectra". In: *Eur. Phys. J.* C73 (2013), p. 2481. DOI: 10.1140/epjc/s10052-013-2481-z. arXiv: 1305.7421 [hep-ph].

[106] F. Aversa et al. "QCD Corrections to Parton-Parton Scattering Processes". In: *Nucl. Phys.* B327 (1989), p. 105. DOI: 10.1016/0550-3213(89)90288-5.

[107] Matteo Cacciari and Paolo Nason. "Is there a significant excess in bottom hadroproduction at the Tevatron?" In: *Phys. Rev. Lett.* 89 (2002), p. 122003. DOI: 10.1103/PhysRevLett.89.122003. arXiv: hep-ph/0204025 [hep-ph].

[108] John C. Collins. "Hard scattering factorization with heavy quarks: A General treatment". In: *Phys. Rev.* D58 (1998), p. 094002. DOI: 10.1103/PhysRevD.58.094002. arXiv: hep-ph/9806259 [hep-ph].

[109] R. C. Baral et al. "Production of *D*-mesons in $p + p$ and p+Pb collisions at LHC energies". In: *Int. J. Mod. Phys.* E25.11 (2016), p. 1650092. DOI: 10.1142/S0218301316500920. arXiv: 1606.07971 [hep-ph].

[110] Georges Aad et al. "Measurement of the differential cross-section of B^+ meson production in pp collisions at $\sqrt{s} = 7$ TeV at ATLAS". In: *JHEP* 10 (2013), p. 042. DOI: 10.1007/JHEP10(2013)042. arXiv: 1307.0126 [hep-ex].

[111] Peter Zeiler Skands. "Tuning Monte Carlo Generators: The Perugia Tunes". In: *Phys. Rev.* D82 (2010), p. 074018. DOI: 10.1103/PhysRevD.82.074018. arXiv: 1005.3457 [hep-ph].

[112] Jonathan M. Butterworth, Guenther Dissertori, and Gavin P. Salam. "Hard Processes in Proton-Proton Collisions at the Large Hadron Collider". In: *Ann. Rev. Nucl. Part. Sci.* 62 (2012), pp. 387–405. DOI: 10.1146/annurev-nucl-102711-094913. arXiv: 1202.0583 [hep-ex].

[113] Torbjorn Sjostrand, Stephen Mrenna, and Peter Z. Skands. "PYTHIA 6.4 Physics and Manual". In: *JHEP* 05 (2006), p. 026. DOI: 10.1088/1126-6708/2006/05/026. arXiv: hep-ph/0603175 [hep-ph].

[114] John C. Collins. "Sudakov form-factors". In: *Adv. Ser. Direct. High Energy Phys.* 5 (1989), pp. 573–614. DOI: 10.1142/9789814503266_0006. arXiv: hep-ph/0312336 [hep-ph].

[115] Peter Skands, Stefano Carrazza, and Juan Rojo. "Tuning PYTHIA 8.1: the Monash 2013 Tune". In: *Eur. Phys. J.* C74.8 (2014), p. 3024. DOI: 10.1140/epjc/s10052-014-3024-y. arXiv: 1404.5630 [hep-ph].

[116] Johannes Bellm et al. "Herwig 7.0/Herwig++ 3.0 release note". In: *Eur. Phys. J.* C76.4 (2016), p. 196. DOI: 10.1140/epjc/s10052-016-4018-8. arXiv: 1512.01178 [hep-ph].

[117] Torbjorn Sjostrand, Stephen Mrenna, and Peter Z. Skands. "A Brief Introduction to PYTHIA 8.1". In: *Comput. Phys. Commun.* 178 (2008), pp. 852–867. DOI: 10.1016/j.cpc.2008.01.036. arXiv: 0710.3820 [hep-ph].

[118] W. Giele et al. "The QCD / SM working group: Summary report". In: *Physics at TeV colliders. Proceedings, Euro Summer School, Les Houches, France, May 21-June 1, 2001.* 2002, pp. 275–426. arXiv: hep-ph/0204316 [hep-ph]. URL: http://lss.fnal.gov/cgi-bin/find_paper.pl?conf-02-410.

[119] Andy Buckley et al. "LHAPDF6: parton density access in the LHC precision era". In: *Eur. Phys. J.* C75 (2015), p. 132. DOI: 10.1140/epjc/s10052-015-3318-8. arXiv: 1412.7420 [hep-ph].

[120] Georges Aad and et. al. Abbott. "Measurement of the inclusive and dijet cross-sections of b-jets in pp collisions at $\sqrt{s} = 7$ TeV with the ATLAS detector. Measurement of the inclusive and dijet cross-sections of b-jets in pp collisions at sqrt(s) = 7 TeV with the ATLAS detector". In: *Eur. Phys. J. C* 71.arXiv:1109.6833. CERN-PH-EP-2011-146 (Aug. 2011). Comments: 10 pages plus author list (21 pages total), 8 figures, 1 table, submitted to Eur. Phys. J. C, 1846. 21 p. URL: https://cds.cern.ch/record/1386708.

[121] Matteo Cacciari, Gavin P. Salam, and Gregory Soyez. "The Anti-k(t) jet clustering algorithm". In: *JHEP* 04 (2008), p. 063. DOI: 10.1088/1126-6708/2008/04/063. arXiv: 0802.1189 [hep-ph].

[122] Matteo Cacciari, Mario Greco, and Paolo Nason. "The P(T) spectrum in heavy flavor hadroproduction". In: *JHEP* 05 (1998), p. 007. DOI: 10.1088/1126-6708/1998/05/007. arXiv: hep-ph/9803400 [hep-ph].

[123] Bernd A. Kniehl. "Inclusive production of heavy-flavored hadrons at NLO in the GM-VFNS". In: *Proceedings, 16th International Workshop on Deep Inelastic Scattering and Related Subjects (DIS 2008): London, UK, April 7-11, 2008.* 2008, p. 195. DOI: 10.3360/dis.2008.195. arXiv: 0807.2215 [hep-ph]. URL: http://inspirehep.net/record/790697/files/arXiv:0807.2215.pdf.

[124] Bo Andersson, Per Dahlqvist, and Gosta Gustafson. "ON LOCAL PARTON HADRON DUALITY. 1. MULTIPLICITY". In: *Z. Phys.* C44 (1989), p. 455. DOI: 10.1007/BF01415560.

[125] Bo Andersson, Per Dahlqvist, and Gosta Gustafson. "ON LOCAL PARTON - HADRON DUALITY. 2. MOMENTUM DISTRIBUTIONS". In: *Z. Phys.* C44 (1989), p. 461. DOI: 10.1007/BF01415561.

[126] Yuri L. Dokshitzer, Valery A. Khoze, and S. I. Troian. "On the concept of local parton hadron duality". In: *J. Phys.* G17 (1991), pp. 1585–1587. DOI: 10.1088/0954-3899/17/10/017.

[127] Pol Gossiaux, Joerg Aichelin, and Thierry Gousset. "Theory of heavy quark energy loss". In: *Prog. Theor. Phys. Suppl.* 193 (2012), pp. 110–116. DOI: 10.1143/PTPS.193.110. arXiv: 1201.4038 [hep-ph].

[128] V. M. Abazov et al. "b-Jet Identification in the D0 Experiment". In: *Nucl. Instrum. Meth.* A620 (2010), pp. 490–517. DOI: 10.1016/j.nima.2010.03.118. arXiv: 1002.4224 [hep-ex].

[129] Georges Aad et al. "Performance of *b*-Jet Identification in the ATLAS Experiment". In: *JINST* 11.04 (2016), P04008. DOI: 10.1088/1748-0221/11/04/P04008. arXiv: 1512.01094 [hep-ex].

[130] Serguei Chatrchyan et al. "Identification of b-quark jets with the CMS experiment". In: *JINST* 8 (2013), P04013. DOI: 10.1088/1748-0221/8/04/P04013. arXiv: 1211.4462 [hep-ex].

[131] Betty Bezverkhny Abelev et al. "Charged jet cross sections and properties in proton-proton collisions at $\sqrt{s} = 7$ TeV". In: *Phys. Rev.* D91.11 (2015), p. 112012. DOI: 10.1103/PhysRevD.91.112012. arXiv: 1411.4969 [nucl-ex].

[132] Matteo Cacciari, Gavin P. Salam, and Gregory Soyez. "FastJet User Manual". In: *Eur. Phys. J.* C72 (2012), p. 1896. DOI: 10.1140/epjc/s10052-012-1896-2. arXiv: 1111.6097 [hep-ph].

[133] Matteo Cacciari and Gavin P. Salam. "Dispelling the N^3 myth for the k_t jet-finder". In: *Phys. Lett.* B641 (2006), pp. 57–61. DOI: 10.1016/j.physletb.2006.08.037. arXiv: hep-ph/0512210 [hep-ph].

[134] Serguei Chatrchyan et al. "Measurement of the Underlying Event Activity at the LHC with $\sqrt{s} = 7$ TeV and Comparison with $\sqrt{s} = 0.9$ TeV". In: *JHEP* 09 (2011), p. 109. DOI: 10.1007/JHEP09(2011)109. arXiv: 1107.0330 [hep-ex].

[135] Constantino Tsallis. "Possible Generalization of Boltzmann-Gibbs Statistics". In: *J. Statist. Phys.* 52 (1988), pp. 479–487. DOI: 10.1007/BF01016429.

[136] Alexander Bylinkin, Nadezda S. Chernyavskaya, and Andrei A. Rostovtsev. "Predictions on the transverse momentum spectra for charged particle production at LHC-energies from a two component model". In: *Eur. Phys. J.* C75.4 (2015), p. 166. DOI: 10.1140/epjc/s10052-015-3392-y. arXiv: 1501.05235 [hep-ph].

[137] Matteo Cacciari, Stefano Frixione, and Paolo Nason. "The p(T) spectrum in heavy flavor photoproduction". In: *JHEP* 03 (2001), p. 006. DOI: 10.1088/1126-6708/2001/03/006. arXiv: hep-ph/0102134 [hep-ph].

[138] R. Albrecht et al. "Production of eta mesons in 200-A/GeV S + S and S + Au reactions". In: *Phys. Lett.* B361 (1995), pp. 14–20. DOI: 10.1016/0370-2693(95)01166-N. arXiv: hep-ex/9507009 [hep-ex].

[139] P. K. Khandai, P. Shukla, and V. Singh. "Meson spectra and m_T scaling in $p + p$, d+Au, and Au + Au collisions at $\sqrt{s_{NN}} = 200$ GeV". In: *Phys. Rev.* C84 (2011), p. 054904. DOI: 10.1103/PhysRevC.84.054904. arXiv: 1110.3929 [hep-ph].

[140] Jaroslav Adam et al. "Measurement of pion, kaon and proton production in proton–proton collisions at $\sqrt{s} = 7$ TeV". In: *Eur. Phys. J.* C75.5 (2015), p. 226. DOI: 10.1140/epjc/s10052-015-3422-9. arXiv: 1504.00024 [nucl-ex].

[141] B. Abelev et al. "Neutral pion and η meson production in proton-proton collisions at $\sqrt{s} = 0.9$ TeV and $\sqrt{s} = 7$ TeV". In: *Phys. Lett.* B717 (2012), pp. 162–172. DOI: 10.1016/j.physletb.2012.09.015. arXiv: 1205.5724 [hep-ex].

[142] Betty Abelev et al. "Multi-strange baryon production in pp collisions at $\sqrt{s} = 7$ TeV with ALICE". In: *Phys. Lett.* B712 (2012), pp. 309–318. DOI: 10.1016/j.physletb.2012.05.011. arXiv: 1204.0282 [nucl-ex].

[143] D. D. Chinellato. "Strange and Multi-Strange Particle Production in ALICE". In: *J. Phys. Conf. Ser.* 446 (2013), p. 012055. DOI: 10.1088/1742-6596/446/1/012055. arXiv: 1211.7298 [hep-ex].

[144] Jaroslav Adam et al. "Measurement of charm and beauty production at central rapidity versus charged-particle multiplicity in proton-proton collisions at $\sqrt{s} = 7$ TeV". In: *JHEP* 09 (2015), p. 148. DOI: 10.1007/JHEP09(2015)148. arXiv: 1505.00664 [nucl-ex].

[145] B. Abelev et al. "Measurement of charm production at central rapidity in proton-proton collisions at $\sqrt{s} = 7$ TeV". In: *JHEP* 01 (2012), p. 128. DOI: 10.1007/JHEP01(2012)128. arXiv: 1111.1553 [hep-ex].

[146] Betty Abelev et al. "D_s^+ meson production at central rapidity in proton–proton collisions at $\sqrt{s} = 7$ TeV". In: *Phys. Lett.* B718 (2012), pp. 279–294. DOI: 10.1016/j.physletb.2012.10.049. arXiv: 1208.1948 [hep-ex].

[147] Wouter Verkerke and David P. Kirkby. "The RooFit toolkit for data modeling". In: *eConf* C0303241 (2003). [,186(2003)], MOLT007. arXiv: physics/0306116 [physics].

[148] F. James. "MINUIT Function Minimization and Error Analysis: Reference Manual Version 94.1". In: CERN-D-506, CERN-D506 (1994).

[149] Richard Nisius. "BLUE: A software package to combine correlated estimates of physics observables within ROOT using the Best Linear Unbiased Estimate method". In: ().

[150]   Richard Nisius. "On the combination of correlated estimates of a physics observable". In: *Eur. Phys. J.* C74.8 (2014), p. 3004. DOI: 10.1140/epjc/s10052-014-3004-2. arXiv: 1402.4016 [physics.data-an].

[151]   Andreas Hocker and Vakhtang Kartvelishvili. "SVD approach to data unfolding". In: *Nucl. Instrum. Meth.* A372 (1996), pp. 469–481. DOI: 10.1016/0168-9002(95)01478-0. arXiv: hep-ph/9509307 [hep-ph].

[152]   G. D'Agostini. "A Multidimensional unfolding method based on Bayes' theorem". In: *Nucl. Instrum. Meth.* A362 (1995), pp. 487–498. DOI: 10.1016/0168-9002(95)00274-X.

[153]   Tim Adye. "Unfolding algorithms and tests using RooUnfold". In: *Proceedings, PHYSTAT 2011 Workshop on Statistical Issues Related to Discovery Claims in Search Experiments and Unfolding, CERN,Geneva, Switzerland 17-20 January 2011.* CERN. Geneva: CERN, 2011, pp. 313–318. DOI: 10.5170/CERN-2011-006.313. arXiv: 1105.1160 [physics.data-an]. URL: http://inspirehep.net/record/898599/files/arXiv:1105.1160.pdf.

List of Figures

List of Tables

Danksagung

Lebenslauf und Bildungsgang

Persönliche Daten

Name:	Linus Feldkamp
Geburtsdatum:	17.05.1985
Geburtsort:	Münster
Staatsangehörigkeit:	deutsch
Familienstand:	verheiratet
Eltern:	Andrea Bölling geb. Jacob
	Dieter Feldkamp

Schulbildung

1991–1994	Johannisschule in Münster
1994–2005	Wilhelm-Hittorf-Gymnasium in Münster

Studium

2005–2011	Physik an der Westfälischen Wilhelms-Universität Münster
01.03.2011	Diplom

Promotionsstudium

Seit Mai 2011	Beginn der Dissertation am Institut für Kern- und Teilchenphysik bei Prof. Dr. J. P. Wessels

Münster, 26. Juli 2018